Experimental Studies and Numerical Simulations on Light-Harvesting Devices

By

Kevin V. Hagedorn

A dissertation submitted in partial fulfillment
of the requirements for the degree of
Doctor of Philosophy
(Chemistry)
in The University of Michigan
2010

Doctoral Committee:

Assistant Professor Stephen Maldonado, Chair
Professor Adam J. Matzger
Professor Raul Kopelman
Assistant Professor Max Shtein

2010

To my parents

Vincent Hagedorn
and
Jeanette Hagedorn

Acknowledgments

I'd like to thank my thesis committee for taking the time to read and evaluate my works. I'd especially like to thank my advisor Stephen Maldonado for his help preparing me for a career in science and for editing this work. His pursuit of perfection has brought my work to a new level and set a standard to which I will be striving in the years to come.

I'd also like to thank Oleg Varnavski, Colin Forgacs, Megan Villwock, Roy Wentz, and Sean Collins for their contributions. Oleg was a mentor and friend early in my graduate career. His help editing manuscripts, teaching me ultra-fast spectroscopy, and fixing instrumentation was invaluable. I'd like to thank Colin for teaching me to use the TeSCA software. His initial work translating TeSCA from German to English and learning how to write programs in TeSCA laid the groundwork for much of my research in nanostructured semiconductors. Megan was a great help editing my manuscripts. Her attention to detail was an inspiration and her availability in a clutch was a life saver. I'd like to thank Roy for teaching me glass blowing. Preparing glass electrodes is a critical skill for an electrochemist and many of the designs utilized in my experiments were his idea. Sean preformed all of the SEM image analysis which is presented in this work. His assistance running SEM helped me move my projects along quickly.

I'd like to thank the University of Michigan for a $600 travel grant and a one term summer research grant.

Table of Contents

List of Figures

List of Tables

Abstract

Obtaining high solar energy conversion efficiencies with materials that require minimal processing or refining is critical to next generation light-harvesting systems. Organic dyes and inorganic nanostructured semiconductors are two material types that address this need and are studied herein.

Two sets of organic chromophore systems were characterized. First, triarylamine multi-chromophore dendrimers with purposely designed biphenyl-based trap sites were investigated using fluorescence upconversion spectroscopy. A rise in the fluorescence from the biphenyl site after the excitation pulse demonstrated that excitons were trapped with 99% efficiency. These data show that excitons can be directed to a specific site in a molecular chromophore. Separately, thiophene macrocycles were investigated to determine if molecular systems could show high energetic degeneracy. The chromophore coupling constants of two thiophene rings were quantified using time-resolved fluorescence anisotropy measurements. The calculated chromophore coupling constants for the cyclic system were an order of magnitude higher than linear chains. In addition, the cyclic system had a two photon absorption cross section of 1470 GM, which is over a thousand times greater than the linear chain and useful for applications in imaging and lithography.

Nanostructured inorganic semiconductors were also the subject of study. In one set of experiments, the first example of macroporous p-GaP(100) was reported and its ability to perform photosynthetic water splitting was demonstrated and assessed. Macroporous films were prepared using a two-electrode cell with a halogen acid electrolyte and pulsed anodic etching voltage waveform. Control over the macroporous

film morphology was explored by varying halogen acid type, concentration, and etching voltage. Macroporous p-GaP has applications in photonic and light-harvesting systems. To this end, the relationship between optoelectronic properties and the obtainable solar energy conversion efficiency was determined in nanostructured semiconductors. The photocurrent-potential response of lightly and heavily doped silicon nanowires were quantified, with the heavily doped semiconductors demonstrating superior energy conversion. For low dopant density nanowires, the low energy conversion efficiencies were attributed to a lack of an internal electric field, which resulted in a high majority carrier recombination at the interface. These data provide design principles for efficient solar energy conversion systems based on nanostructured semiconductors.

Chapter 1
Introduction

I. Overview.

A. Motivation – Light harvesting systems are a sustainable long term solution for meeting human energy demands. Although the earth's crust contains enough coal to sustain our global energy use for several hundreds of years, the ecological impact of excess CO_2 production could eventually render the use of fossil fuels unsustainable.[1-2] Radiant power from the sun is the largest source of renewable energy on earth,[3-4] more than all of fossil fuels[3,5-6] and nuclear fuels[7] combined. While the current global energy use is approximately 13 TW (1.3×10^{13} W),[3,8] the sun delivers 3,850,000 TW (3.8×10^{19} W)[3,6] of power. Harvesting only a fraction of a percent of the yearly solar energy flux would meet current energy demands. This is in contrast to hydroelectric[6] and wind power,[4,9] which, even if fully utilized, would barely meet current energy demands and would leave little room for future increases in energy demand. If solar energy conversion systems could be made from earth abundant materials[10] their use could provide power without environmental impact.[11]

B. Solar Energy Conversion Systems - The research in this thesis is concerned with solar energy conversion systems that use light to generate energetic electrons and holes. Although solar energy conversion systems based on heat transfer are known,[12] they are not considered here. In solar-to-electric energy conversion systems (photovoltaics), an electrical current is generated. In solar-to-fuel energy storage systems, solar energy is stored in the chemical bonds of a generated fuel.[13] Both of these systems have an upper efficiency limit of 85% in a multiple absorber system.[14] In comparison, heat engines have much lower maximum energy conversion efficiency.[15] The work in this thesis aims to elucidate new design features for scalable solar energy conversion systems.

C. Challenge for Solar Energy Conversion Systems - Current photovoltaic technologies rely on high-purity, energy-intensive silicon, resulting in a 3- to 4-year payback time on

Table 1.1. A comparison of energy sources and energy use

Renewable Energy Source	Available Power /TW
Solar[a,b]	3,850,000
Wind[c,d]	14
Hydroelectric[b]	3
Energy Usage Rate in 2003[a,e]	13 TW

[a] Smil, V. Energy at the Crossroads: Global Perspecives and Uncertainties; MIT Press: Boston, 2003

[b] Goldemberg, J.; Johansson, T. B. World Energy Assessment Overview; United Nations Development Programme: New York, 2004. www.undp.org/energy/weaover2004.htm.

[c] Lu, X.; McElroy, M. B.; Kiviluoma, J. Proceedings of the National Academy of Sciences 2009, 106, 10933.

[d] Archer, C. L.; Jacobson, M. Z. J. Geophys. Res. 2005, 110, D12110.

[e] BP Statistical Review of World Energy 2004; BP: London, England. http://www.bp.com/subsection.do?categoryId=95&contentId=2006480

the energy cost of the device.[16] This aspect has prevented solar energy from supplanting fossil fuels as a primary energy resource. The objective of my graduate research is to identify and investigate novel materials for solar energy conversion systems. Two classes of materials, organic chromophores[17-18] and nanostructured crystalline inorganic semiconductors,[19-20] are considered.

II. Organic Chromophores.

A. Light Absorption in Organic Chromophores – All solar energy conversion systems require the ability to absorb light. Absorption bandwidth and absorptivity define the range of energies that can be absorbed and the needed amount of material to absorb light, respectively. The solar spectrum outputs energy over a wavelength range from 250 to 2500 nm (Figure 1).[21-22] Light harvesting systems need to absorb this wavelength range, but a larger absorption bandwidth is preferable. The absorptivity, which is different for each wavelength, defines the probability that a photon is absorbed. Materials with a low absorptivity need to be thicker for the same amount of light to be absorbed.[23] The goal of absorption is to cause an electronic transition, which generates an excited electron and leaves a vacancy, known as a hole. This electron-hole pair is bound by coulombic attraction and is referred to as an exciton. The exciton is separated and used to generate an electrical current or produce fuel.

The absorption bandwidth and absorptivity of a material is determined by the interaction of light with charged particles in the material. Electromagnetic radiation is an oscillating electric field. The frequency of these oscillations determines the characteristic energy of the photon.[24] As the photon passes through matter, nuclei and electrons feel the effect of this oscillating field and begin oscillating at the same frequency in response. In a simple hydrogen atom composed of one proton and one electron, the attractive force between these charged particles resembles a classical spring. The passing photon's electric field puts a force on the charged particles and causes the spring to oscillate. The electron can only occupy certain discreet distances from the nucleus, which each have a characteristic spring constants. The change in the dipole moment, which occurs as the electron moves from one orbital to another, along with the associated change in the spring constant is known as the transition dipole moment.

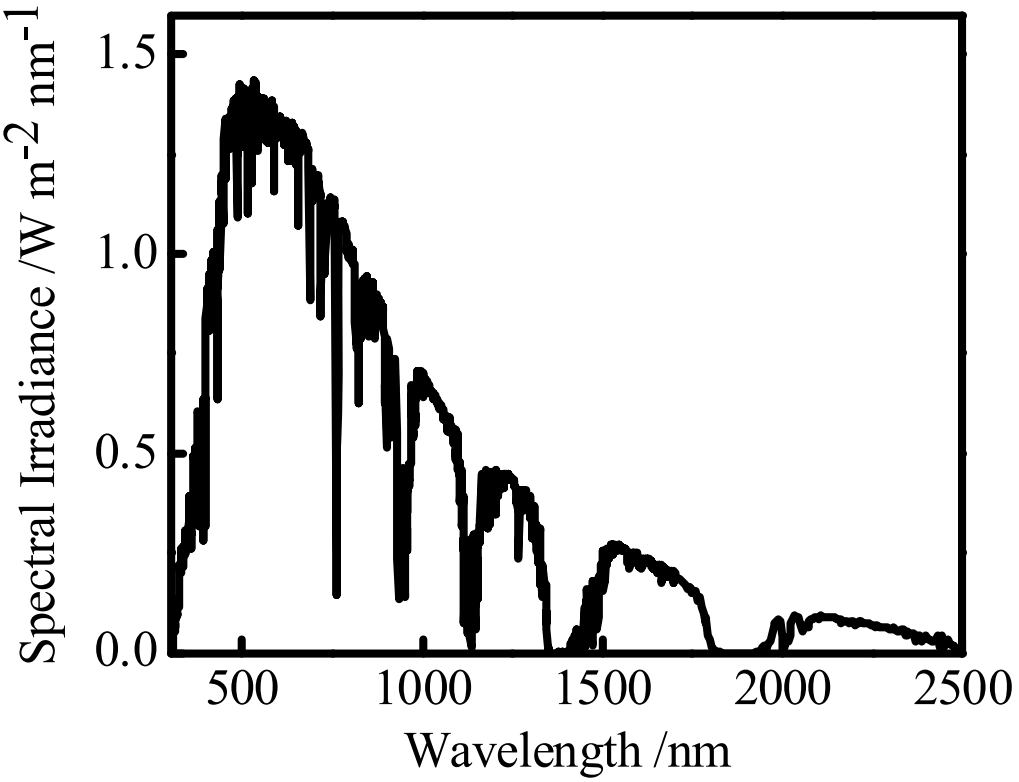

Figure 1.1. The solar spectral irradiance under AM 1.5 conditions from 250 nm to 2500 nm[21-22].

Absorption of a photon can occur if the photon's frequency matches the resonance frequency of the transition dipole moment. The absorption probability is highest when the frequency of light and the resonance frequency of the transition dipole match exactly.[24-26]

Absorption of light corresponding to an electronic transition can be understood using a simple spring analogy. If a transition involves only the nuclei and a single electron, the range of frequencies over which the transition is allowed will be very narrow. In contrast, molecular dyes are more complicated as they consist of an ensemble of many atoms. The transition dipole in these systems is a combination of an electronic transition and nuclear vibrations and rotations. This increases the range of wavelengths over which the molecule can absorb light, as different rotations and vibrations can couple to match the frequency of a range of wavelengths. On the other hand, these molecules are not modeled well as harmonic oscillators. The probability of absorption in these systems can be compared to perfect oscillators using a unitless coefficient called the oscillator strength, with values from 1 to 1 x 10^{-10} in organic chromophores.[24-25] Systems with very broad absorption spectra, like many inorganic complexes, do not model the harmonic oscillator well and have low oscillator strengths and low absorption probabilities.[27] Systems that model a harmonic oscillator well, like many laser dyes, have narrow absorption bands but high oscillator strengths and high absorption probabilities.[28] For perspective, strongly-absorbing dyes require a film thickness of 30 nm to collect 99% of incident light.[29-31] A challenge with organic chromophores is to find combinations of dyes that have high oscillator strengths (and by extension, absorptivity) and broad absorption bandwidths.

B. Exciton Migration in Organic Materials - Upon absorption of electromagnetic radiation, an electron-hole pair is generated, known as an exciton. This exciton needs to be separated to perform useful work (Figure 2). In organic chromophores, the energy binding the electron-hole pair is between 0.1 and 1 eV,[32-34] which is much greater than k_BT. Therefore, the energy barrier to separate excitons in organic chromophores is too high to happen spontaneously. The distance an exciton can travel is determined by the exciton diffusion length,[35-36] which is dependent on the lifetime of the exciton and diffusion:

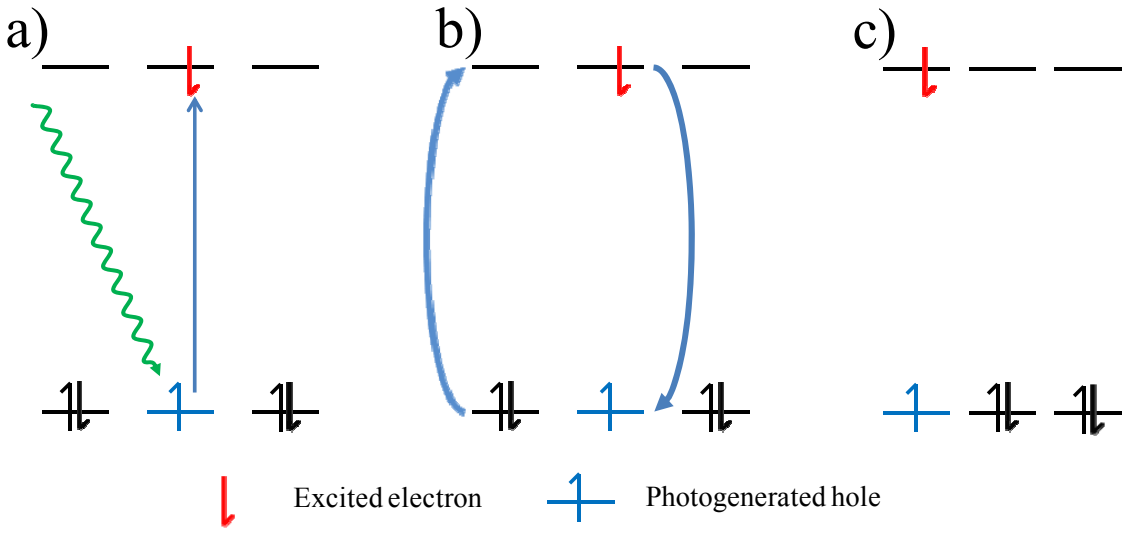

Figure 1.2. Schematic diagram illustrating the process by which excitons move in organic materials. (a) Generation of the exciton. (b) Exciton hopping. (c) Exciton after spatial movment.

$$L_e = \sqrt{D\tau} \quad (1)$$

where D is the exciton diffusion coefficient, and τ is the exciton lifetime. Exciton diffusion lengths are generally on the order of 10 nm.[37] The fact that only a 10 nm layer of dye can be used puts an important constraint on systems utilizing organic dyes. The process of exciton hopping is shown in Figure 2b and 2c.[32] In particular, only extremely thin dye layers around the semiconductor contacts contribute to the generation of charge carriers.

C. Challenges - Light harvesting systems utilizing organic chromophores, while attractive due to their simple processing, typically have low energy conversion efficiencies due to a mismatch between the exciton diffusion length and the thickness needed to absorb an adequate portion of the solar spectrum. In order to improve energy conversion efficiencies in these devices, the exciton diffusion length needs to be improved or new dyes with higher absorptivity and absorption bandwidths need to be developed. The exciton diffusion length in these materials is short because of the amorphous nature of the systems.[38-40] In amorphous systems, molecules are free to vibrate and rotate, generating trap sites within the molecule. Hopping to adjacent molecules is complicated as the distance between molecules varies.

D. Hypothesis – One method for studying trap sites is to intentionally include them. By including different types of traps and studying the effect they have on exciton diffusion length, the effect of various traps can be estimated in new materials. I have investigated a series of multi chromophore systems all of which are composed entirely of triarylamine chromophores, but differing in their connectivity. I investigated these multi chromophore systems in order to determine if the connectivity which included a biphenyl unit would trap excitations, by measuring the time-resolved fluorescence from the biphenyl unit.

Another method of improving exciton diffusion length is to find geometries that minimize trapping. One such geometry is a cyclic system. In a cyclic arrangement of chromophores, the system has improved uniformity because there are no 'end effects,' which change the energetics of chromophores on the end of molecules versus the core chromophores.[41-43] To determine if the cyclic arrangement affects energetic degeneracy,

fluorescence upconversion anisotropy measurements will be used to determine chromophore coupling constants, we predict that the coupling constant will be greater in the cyclical system than in the linear chains.

E. Relevant Experimental Methods - In order to better understand the operation of organic chromophores in the context of light harvesting, the absorptivity, the bandwidth of absorption, the exciton lifetime, the rate of exciton hopping between chromophores, and the rate of charge hopping between chromophores need to be measured. In this section, experimental techniques that were used to quantify these properties are described.

1. Absorption Spectroscopy - Absorption spectroscopy is a technique used to determine the oscillator strength and absorption bandwidth of a chromophore. In this experiment, the power of a beam of light is measured before and after interaction with a sample.[23] The absorbance of the bulk sample can be related to the absorptivity of a single molecule through beer's law:

$$A(\lambda) = \varepsilon(\lambda)Cl \tag{2}$$

where ε is the molar absorptivity, C is the concentration, and l is the path length.

2. Fluorescence Emission Spectroscopy - Fluorescence spectroscopy gives information about the excited state of a molecule, which can be used to infer structural information. In this experiment, short wavelength photons excite a sample, which then emit long wavelength photons. The incident light is generated by a lamp and separated into monochromatic light by a monochromator. The emitted photons are detected by a photodiode.[23]

3. Transient-Absorption Spectroscopy – Transient-absorption spectroscopy is a technique used to monitor a charge or exciton migration rate as it moves through a multi chromophore system. Transient-absorption spectroscopy is an extension of absorption spectroscopy. Here, the absorbance at a particular wavelength or range of wavelengths of a sample is measured as a function of time after excitation by a flash of light. In a typical experiment, both the light for excitation ('pump') and the light for measuring the absorbance ('probe') are generated by a pulsed laser. This experiment is shown in detail in Figure 3. Two pulses of light are incident on the sample: the first is a 'pump' pulse

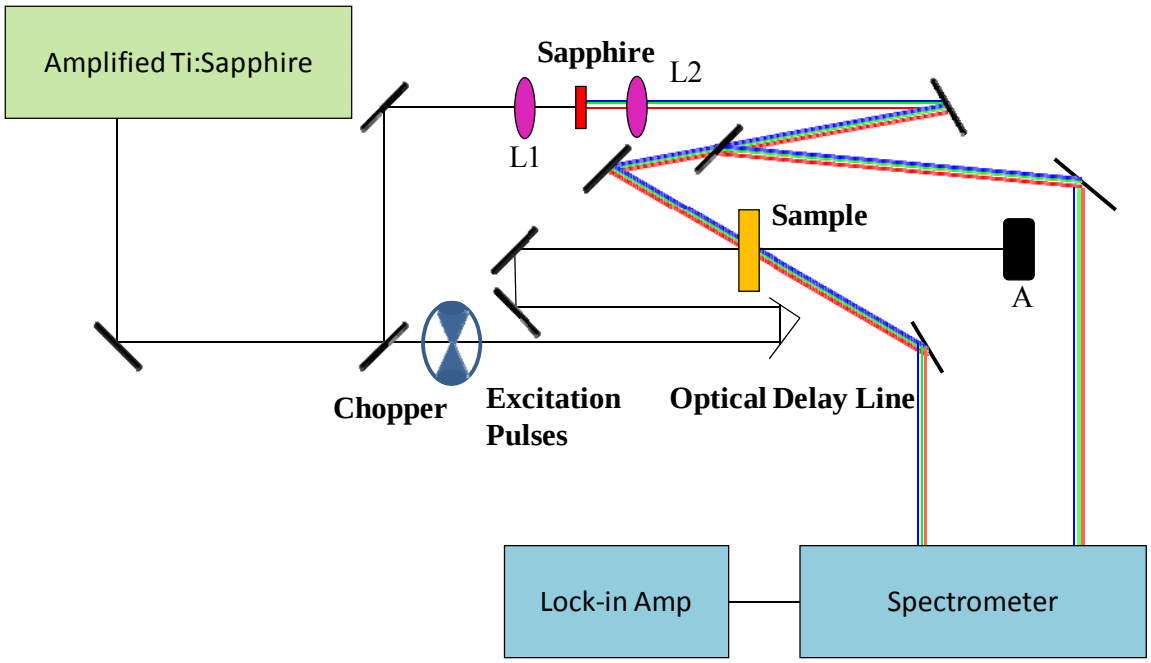

Figure 1.3. Schematic diagram showing the design of a transient absorption setup. Focusing lenses are denoted as L1 and L2. A black body absorber is located at A.

which excites the sample to a higher energy state; the second is a 'probe' pulse which is white light containing many wavelengths. The optical delay is moved back and forth to make the path length longer or shorter, which increases or decreases the time between the pump pulse and the probe pulse. When the probe pulse interacts with the sample, some amount of light is absorbed. The spectrometer records the number of photons in the presence and absence of the pump pulse. The change in the number of photons absorbed with varying amounts of time between the pump and probe is reported.[44-45]

4. Fluorescence Upconversion Spectroscopy - Time-resolved fluorescence spectroscopy is an extension of fluorescence spectroscopy, which is used to track excited-state populations on a particular chromophore as a function of time. Here, the fluorescence of a sample is monitored as a function of time after excitation by a flash of light. A short laser pulse acts as a gate for the detection of fluorescence light; only fluorescence light that arrives at the detector at the same time as the gate pulse is detected. This is shown in Figure 4. The BBO crystals at NC1 and NC2 convert 5% of the light incident on them into light with double the energy. That is, they combine two 1 eV photons into one 2 eV photon 5% of the time, on the condition that the photons arrive at exactly the same time. The BBO crystal at NC1 converts 5% of the 800 nm light into 400 nm light. The gate pulse then passes through an optical delay on its way to NC2. The excitation pulse excites the sample which begins to fluoresce. The fluorescence emission that arrives at NC2 at the same time as the gate pulse is recorded, as the BBO crystal will sum the energy of the gate pulse with the energy of the emitted photon. Since the emission wavelength is known, the energy of the resulting photon is known, and the monochromator can be set to only record light of this wavelength. The optical delay is moved to change the time that the gate pulse arrives at NC2 and therefore the timescale probed.[46]

5. Two-Photon Excitation Fluorescence Microscopy – The setup is similar to fluorescence spectroscopy, except a light pulse on the order of 100 fs is used for the excitation source. The power of the laser is attenuated by neutral density filters. Emission from the sample is recorded as a function of light intensity (I_o), if the emission intensity squared is proportional to the incident power, then the emission is due to two-

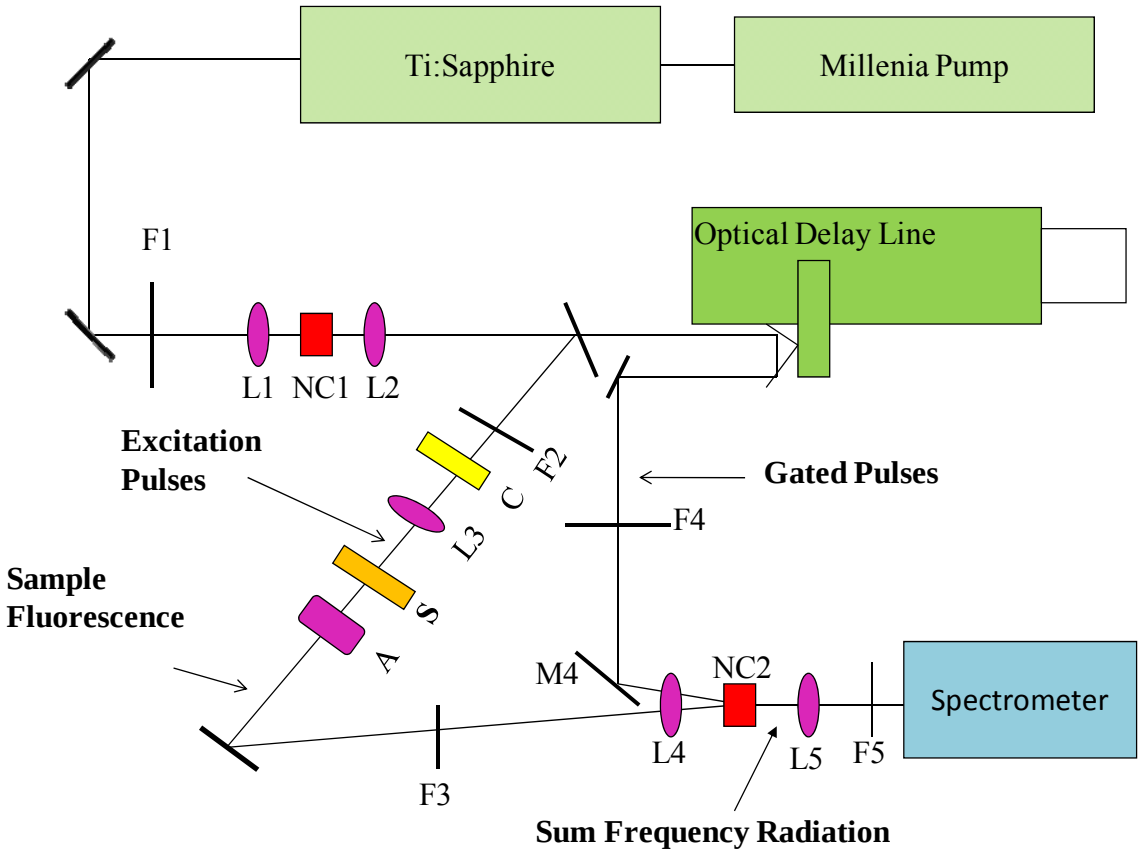

Figure 1.4. Schematic diagram showing the design of a fluorescence upconversion setup. Focusing lenses are denoted as L1-5, the non-linear optical BBO crystals are denoted NC1-2, the sample is denoted S, and the light polarization is changed with a compensator at C.

photon absorption.[47-48] Materials with high two-photon absorption cross sections are of importance to applications in lithography[49-50] and imaging.[51-52]

III. Inorganic Semiconductor Photoelectrodes.

A. Light Absorption in Inorganic Crystalline Semiconductors – A description of light absorption in semiconductors parallels light absorption in organic chromophores, with some notable exceptions. In a discrete molecule, the states are single-energy levels, and the energy of the photon must match the gap exactly. In crystalline materials, a continuous range of energy levels is available, known as a band. In semiconductor materials, two bands separated by a large gap are present. For a intrinsic semiconductor in the dark (and at 0 K), the valence band is completely filled with electrons, while the conduction band is completely empty. The bandgap refers to the space between the bands where no energy levels exist. This is shown graphically in Figure 5. A photon's energy must be greater than the bandgap energy to be absorbed. Regarding oscillator strength, semiconductor materials are broadly divided into indirect bandgap and direct bandgap materials. In an indirect bandgap semiconductor, generation of an electron-hole pair also requires a change in momentum. In order for momentum to be conserved, absorption of a photon in an indirect band gap material must also involve a lattice vibration, which provides the difference in momentum between the electron and hole momentum.[53-54] This additional requirement to absorption means that the probability of absorption is lower and the material needs to be thicker. Silicon is an indirect bandgap semiconductor and light with a wavelength of 1000 nm requires 156 μm of silicon to be absorbed.[55] The primary advantage of direct bandgap semiconductors is that thin film absorbers can absorb light in 100 nm of material.

B. Carrier Generation-Recombination – Photons absorbed by a semiconductor material generate free carriers, and are conducted to contacts as positive and negative charges. The binding energy of excitons in semiconductor materials is on the order of 0.01 eV.[34] The lifetime of photogenerated charge carriers is critically dependent on the structure and composition of the crystal. The oppositely-signed electrons and holes can recombine, giving up the excess energy as heat (non-radiative recombination) or as an emitted photon (radiative recombination). The longevity of these carriers depends on the

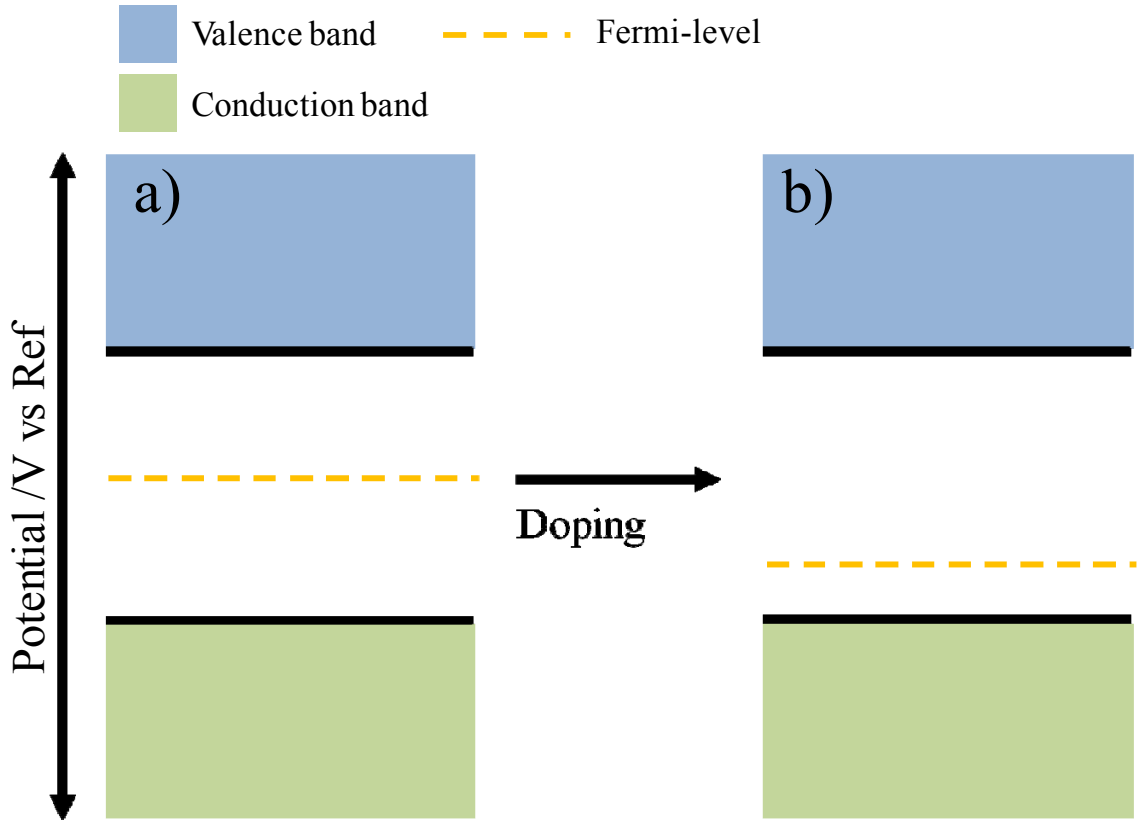

Figure 1.5. Schematic diagram showing the band structure of a semiconductor before and after doping with a p-type dopant. (a) An intrinsic semiconductor material. (b) The semiconductor material after adding a p-type dopant. In the doped material, the Fermi-level is reduced and the conductivity is increased.

available paths on which excess energy can be lost. In impure, defect-rich materials, energy states situated between the conduction and valence bands facilitate recombination,[54,56-57] which creates a trade-off between purity and device efficiency. More refined materials allow for longer lifetime photogenerated carriers.

The minority carrier diffusion length, L_d, describes the path length of a minority carrier in a field-free region and is a critical parameter for solar energy conversion. Like the exciton diffusion length, the average distance that a minority carrier can travel before recombining is determined by diffusion and the lifetime of the carrier, as shown in eq 3:

$$L_d = \sqrt{D\tau} \tag{3}$$

where D is the diffusion coefficient and τ is the carrier lifetime. This parameter is critical for energy conversion systems because charges generated within the bulk of the material need to reach the surface to perform useful work. Charges generated more than the diffusion length away from the interface recombine and do not contribute to the total current density. If low-purity materials are used in planar photovoltaic technologies, the current density would be prohibitively low due to small values for L_p.

C. Charge Carrier Collection - The simplest method of separating photogenerated charges is by using an electric field. An electric field develops when two materials having dissimilar work functions are brought into contact. The work function of a material is defined as the energy required to remove an electron from the bulk to a point an infinite distance away. In an intrinsic semiconductor, the average energy to remove an electron occurs midway between the bands. The probability of finding an electron is given by the Fermi function:

$$f(E) = \frac{1}{e^{(E-E_F)/k_BT}+1} \tag{5}$$

where *f(E)* is the probability of finding an electron at a specific energy, E is the energy level in question, E_F is the Fermi level, k_B is Boltzmann's constant, and T is the temperature. The probability of finding an electron is one-half at the Fermi-level. To change the work function of a semiconductor, a dopant can be added. If the dopant added

has fewer electrons than the semiconductor material, additional holes are introduced which increase conductivity and decrease the work function (Figure 5). The conducting media can be a variety of materials. If a solution is used, the Fermi-level is defined by species dissolved in solution. If a metal is used, the work function is defined by the identity of the metal. In the example of a p-type semiconductor in contact with a metal with a larger work function, a large concentration gradient of electrons exists between the semiconductor and the conductor due to the different work functions. If charges are free to transfer across the interface, the system will reach an equilibrium condition dictated by the electrochemical potential energy of electrons on either side of the interface and the energetic factors pertinent to heterogeneous charge transfer. For the condition where interfacial charge transfer is sufficiently fast so as not to be process limiting, charges will flow across the interface to render the electrochemical potential energy of electrons equal throughout the system. A result of this process is the development of a depletion layer within the near surface region of the semiconductor which is devoid of majority carriers. An electrical field is developed between the bulk and interface of the semiconductor which represent as electrostatic barrier for further charge transfer of majority carrier from the bulk across the interface.[53] The amount of charge that flows into or out of the material can be quantified using capacitance-voltage measurements. The space charge layer is illustrated in Figure 6.

D. Limitations of Conventional Photovoltaics – In configurations where light absorption and carrier collection occur in parallel, the minority carrier diffusion length and optical penetration depth are critical. Figure 7a is a cross section of a generic photovoltaic cell. Light is incident on the surface of the device, generating carriers in the material at the optical penetration depth. The photogenerated minority carrier must then diffuse back to the transparent contact to be collected. An alternative design for light harvesting is to orthogonalize the light absorption and carrier collection (Figure 7b). If the nanomaterial is designed such that carriers are generated within a diffusion length of the interface, all of the minority carrier can be collected. This effectively increases the volume in which charges can be collected, and in many cases has been shown to increase the short circuit current density of the device.[58-59] However, despite this apparent advantage, it has been observed that creating nanostructured devices does not always increase the current

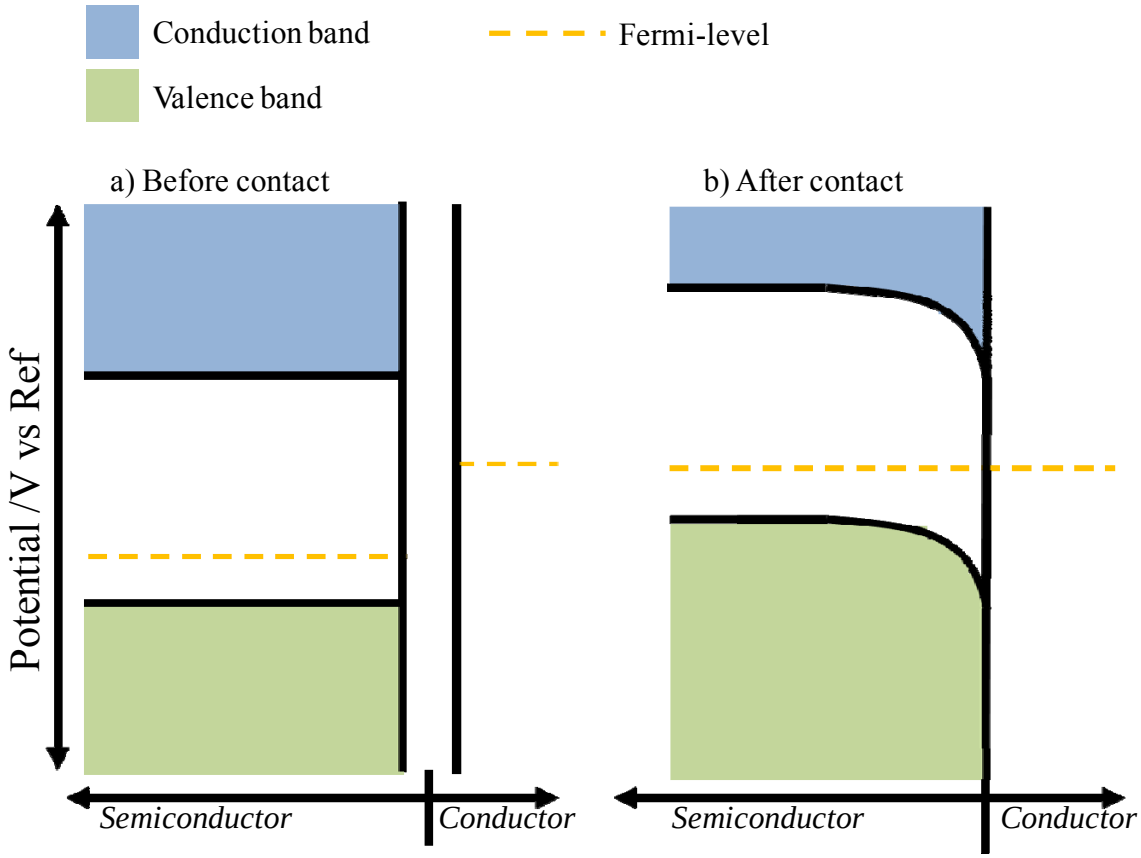

Figure 1.6. Schematic diagram showing the band structure of a p-type semiconductor device (a) before contact with a conducting material which has a smaller work function. (b) after contact with the conducting material, a field region forms at the surface which directs electrons towards the interface and holes away from the interface. This aids in charge separation.

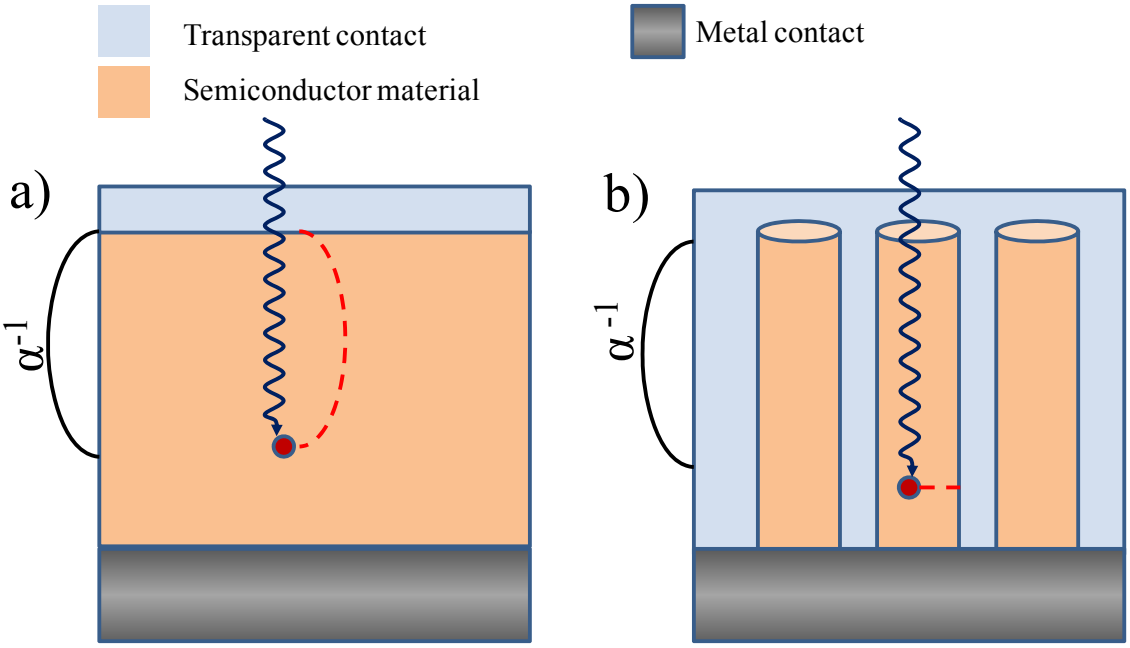

Figure 1.7. Schematic diagram showing a typical planar light harvesting device (a) and a nanostructured light harvesting device (b). In the planar light harvesting device the optical penetration depth and the distance that the minority carrier has to diffuse to be collected are coupled. In the nanostructured device the optical penetration depth and the carrier diffusion length can be decoupled.

density, which has been attributed to such things as slow heterogeneous charge transfer, recombination at the interface and charge recombination in the bulk of the material.[60]

E. Hypothesis – Gallium phosphide is used in the manufacture of light-emitting diodes,[61-63] is made from earth abundant materials,[64-66] and has favorable bandgap and electronic properties for fuel forming reactions.[67-69] However, due to poor minority carrier diffusion lengths and an indirect bandgap,[70-72] it has not found any practical use in solar cells. By making the material nanostructured, the short circuit current density can be increased to useful levels.[58-59] Nanostructured n-GaP has been investigated previously,[73-80] but n-type semiconductors suffer from problems with stability while performing photosynthetic water-splitting due to the formation of surface oxides, although new chemical treatments may help prevent the formation of oxides.[81-83] Macroporous p-GaP(100) photoelectrodes were prepared and the photocurrent density was compared to planar p-GaP(100) photoelectrodes under short-circuit conductions, the macroporous electrodes are expected to generate a larger current density corresponding to a larger carrier collection efficiency.

Despite the simplicity of the concept of using nanostructured systems, few materials have been able to effectively utilize the design.[84] A possible reason may be poor match between the size of the depletion region and the size of the nanostructure. For a barrier height of 1 eV and a dopant density of 1 x 10^{15} cm^{-1}, the depletion width is on the order of 500 nm. If the size of the morphological features in a nanostructured semiconductor is less than 500 nm, a full depletion region is not possible. Few studies have explored the effect that doping has on energy conversion efficiency.[85-86] I have prepared Si nanowires with identical morphologies and different dopant densities for the purpose of comparing the photoresponse of nanowires which do and do not support an internal electric field, nanowires which do not support an internal electric field are expected to demonstrate lower energy conversion efficiency.

F. Methods for Studying Inorganic Semiconductors - In order to better understand the operation of inorganic crystalline semiconductors in the context of light harvesting, the short-circuit current density, the open-circuit voltage, the absorptivity, the minority carrier diffusion length, the flatband potential, the surface recombination velocity, and the dopant density need to be measured. In this section, experimental techniques that were used to quantify these properties in the chromophores studied are described.

1. Regenerative Photoelectrochemical Cell and Fuel Forming Cells - Liquid media provide a convenient method for studying semiconductor materials for several reasons. First, the redox potential of the liquid media is determined by the redox couple dissolved in solution; changing the work function of the conducting solution is a simple matter of changing the species dissolved in solution. Second, the contact between a liquid solution and electrode is conformal. Third, the contact process is non-destructive. Placing the material to be studied into a liquid is perhaps the least destructive method of making contact. In photoregenerative cells, a redox couple is used, such as dimethyl Ferrocene/Ferrocinium ($dmFc/Fc^+$) so that each charge reaching the surface of the semiconductor oxidizes one molecule of dmFc to a molecule of $dmFc^+$. The solution conducts charges to the counter electrode as another molecule of $dmFc^+$ near the counter electrode is reduced from $dmFc^+$ to dmFc.

2. 3-Electrode Cell with Potentiostatic Control - 3-electrode cells are used to deconvolute the response of the working electrode from the counter electrode. Recording the current-voltage characteristics of a device requires two electrodes. The reference electrode is a half cell with a known reduction potential. Its only role is to act as a reference for measuring and controlling the working electrodes potential; at no point does it pass any current. The counter electrode passes all the current needed to balance the current observed at the working electrode. To achieve this current, the counter will often swing to extreme potentials at the edges of the solvent window, where it oxidizes or reduces the solvent or supporting electrolyte.

3. Steady-State Response as a Function of Light Intensity - Photocurrent-potential measurements were taken to determine parameters relevant to the energy conversion efficiency of electrode materials such as short-circuit current, open-circuit potential and fill factor. Simulated solar sunlight was used to illuminate the working electrode surface. The current-voltage characteristics report on the short-circuit current density, open circuit voltage and fill factor of a photoelectrode.

4. Quantum Yield-Wavelength Response Measurements - Spectral response measurements can be used to determine minority carrier diffusion length and report on the carrier collection efficiency as a function of the penetration depth of light into the material. The number of photons incident on the sample and number of electrons out are

recorded. A setup for this measurement is shown in Figure 8. A lock-in detection scheme is used to maximize the signal to noise ratio.

5. Capacitance-Voltage Measurements - These measurements can be used to determine dopant density and flatband potential of the semiconductor material. The depletion region of a semiconductor heterojunction behaves like a capacitor because it contains ionized charges. By varying the voltage applied to the junction, it is possible to vary the depletion width. The dependence of the depletion width upon the applied voltage provides information on the semiconductor's internal characteristics, such as its doping content and the energetics of the band edges. Measurements are obtained by applying a DC voltage in addition to a small-signal AC signal. The total voltage drop over the depletion region can be calculated from capacitance and is given by the Mott-Schottky relation provided in eq 5:

$$C_{SC}^{-2} = \frac{2}{e\varepsilon\varepsilon_o N_D}(V_{bi} - V_{app} - k_B T/q) \quad (5)$$

where C_{sc} is the capacitance, q is the elementary charge, ε and ε_o are the dielectric constant and the permittivity of free space, respectively, N_D is the dopant density, V_{bi} is the built-in voltage drop across the depletion region, V_{app} is the applied voltage.

IV. Statement of Dissertation Research.

The overarching purpose of this dissertation is to elucidate design features for efficient scalable solar energy conversion systems. In chapters 2 and 3 the focus is on molecular chromophore design. In chapters 4 and 5 the emphasis is on nanoscale semiconductor photoelectrode design.

A multi chromophore system where exciton traps sites have been purposefully built into the system are subject to study in Chapter 2. In this chapter, a series of molecules composed of identical materials chromophore units are investigated. It was found that the arrangement of chromophore atoms can create trap sites, which can be used to control and direct excitons. This is potentially useful for designing energy conversion systems where light is absorbed by a ‘black dye’ layer and for improving exciton diffusion lengths.

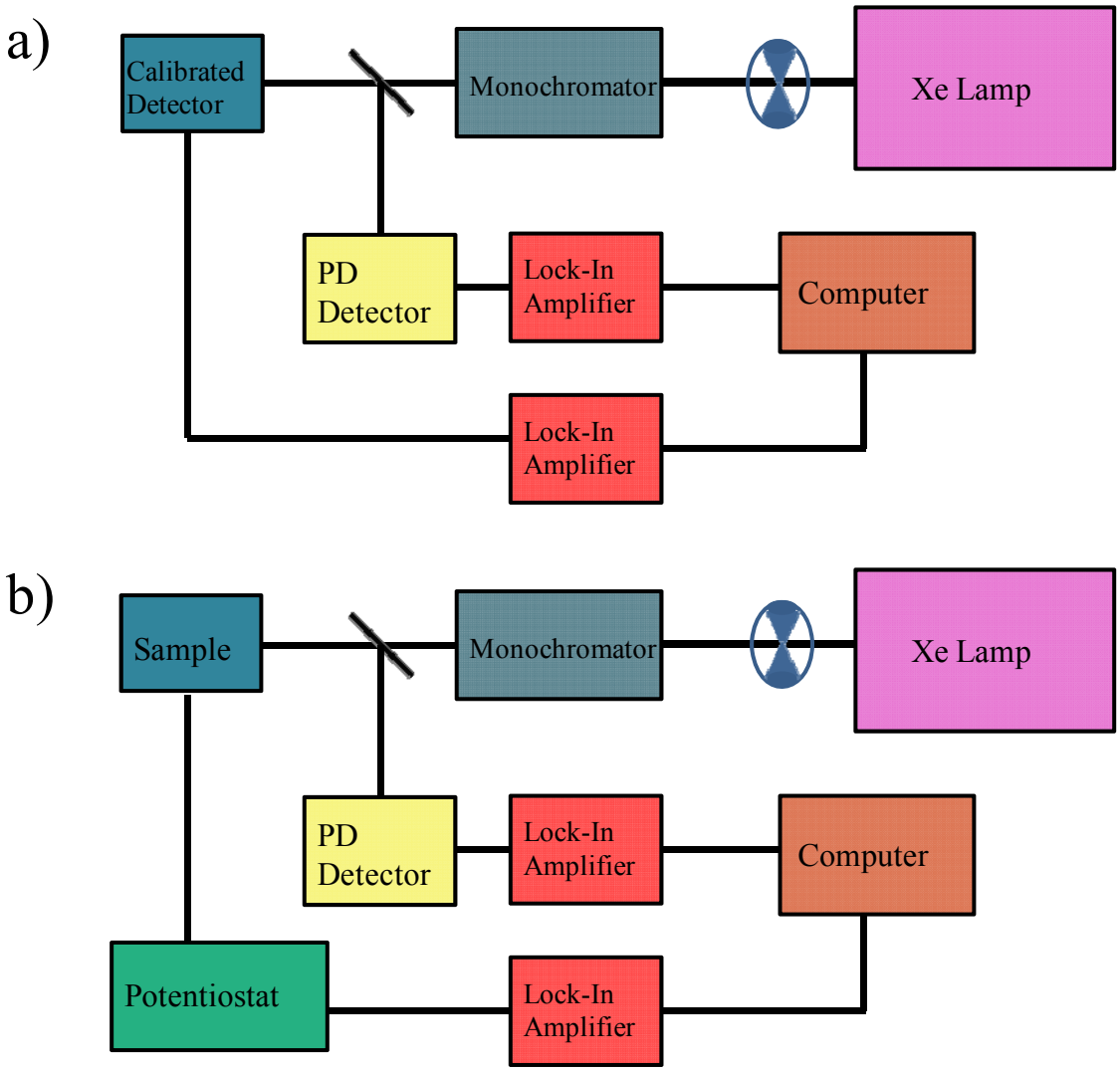

Figure 1.8. Schematic diagram of a spectral response system, the yield is determined by dividing the electrons collected from the sample by the photons collected by the calibrated detector. The yield is reported as a function of the excitation wavelength. A lock in detection scheme is used to improve the signal-to-noise ratio, as the illumination is only a few milliwatts of power. (a) The configuration used to count the incident photons using a calibrated detector. (b) The configuration used to count the electrons generated by a sample photoelectrode.

Chapter 3 investigates a series of chromophores with the highest possible symmetry, a series of chromophores arranged in a circle. The photophysical properties of cyclic thiophenes were determined. It was found that this arrangement gave interesting properties relating to exciton migration and two photon absorption. Excitons in this system were found to be delocalized over an unusually large number of chromophores. In addition, the two photon absorption cross section was the highest recorded at the time.

In Chapter 4, a novel macroporous system is reported: macroporous p-GaP(100). This chapter demonstrated the first example of macroporous p-GaP, and the ability of this material to perform photosynthetic water splitting was measured. Preliminary studies of the material did not show enhancement of the energy conversion properties, which was the subject of further study in Chapter 5. However, this chapter represents the first example of a novel class of material that will likely have interesting photonic and energy conversion properties.

In Chapter 5, the energy conversion efficiency as a function of the optoelectronic properties of nanowire semiconductors is quantified. Two sets of silicon nanowires with varying dopant densities were studied and the effect on energy conversion was determined. It was found that when the dopant density was low, such that the radius of the nanowire was larger than the depletion width, the nanowires were inactive for energy conversion. These results were paralleled in a two-dimensional software package (TeSCA),[87-89] and the relative effects of dopant density, surface recombination, and minority carrier diffusion length on carrier collection efficiency were explored. It was found that the dopant density was the most critical parameter for efficient energy conversion. This suggests new design rules for nanostructured materials,[90-92] as dopant density needs to be optimized for energy conversion to be efficient.

Chapter 6 summarizes the findings of chapters 2, 3, 4 and 5 and suggests future work. In this chapter, conclusions are drawn regarding the impact of this research and future directions for the research are considered.

The text of chapters 2, 3, 4 and 5 are reproduced from recently published works.[93-96]

V. References.

1. Oreskes, N. *Science* **2004**, *306*, 1686.
2. Lu, J.; Vecchi, G. A.; Reichler, T. *Geophys. Res. Lett.* **2007**, *34*, L06805.
3. Smil, V. *Energy at the Crossroads: Gloabal Perspectives and Uncertainties*; MIT Press: Boston, 2003.
4. Archer, C. L.; Jacobson, M. Z. *J. Geophys. Res.* **2005**, *110*, D12110.
5. *International Energy Annual 2006* U.S. Energy Information Administration: Washington, DC. http://www.eia.doe.gov/emeu/iea/res.html.
6. Goldemberg, J.; Johansson, T. B. *World Energy Assessment Overview*; United Nations Development Programme: New York, 2004. www.undp.org/energy/weaover2004.htm.
7. Price, R.; Blaise, J. R. *Nuclear Fuel Resources: Enough to Last?*; Organization for economic co-operation and development: Paris, France, 2002.
8. *BP Statistical Review of World Energy 2004*; BP: London, England. http://www.bp.com/subsection.do?categoryId=95&contentId=2006480.
9. Lu, X.; McElroy, M. B.; Kiviluoma, J. *P. Natl. A. Sci.* **2009**, *106*, 10933.
10. Hedrick, J. B. *Rare earths: U.S. Geological Survey Minerals Year-book, Metals and Minerals*; U.S. Department of the Interior: Washington, D.C., 2001; p. 61.1.
11. Fthenakis, V. *Energy Policy* **2000**, *28*, 1051.
12. Cadafalch, J. *Sol. Energy* **2009**, *83*, 157.
13. Fonash, S. *Solar Cell Device Physics*; 2nd ed.; Academic Press: Salt Lake City, UT, 2010.
14. Brendel, R.; Werner, J. H.; Queisser, H. J. *Sol. Energ. Mat. Sol. C.* **1996**, *41-42*, 419.
15. Takaishi, T.; Nakano, R.; Numata, A.; Sakaguchi, K. *Mitsubishi Heavy Industries Technical Review* **2008**, *45*, 21.
16. Shah, A.; Torres, P.; Tscharner, R.; Wyrsch, N.; Keppner, H. *Science* **1999**, *285*, 692.
17. O'Regan, B.; Grätzel, M. *Nature* **1991**, *353*, 737.
18. Nazeeruddin, M. K.; Kay, A.; Rodicio, I.; Humphry-Baker, R.; Muller, E.; Liska, P.; Vlachopoulos, N.; Grätzel, M. *J. Am. Chem. Soc.* **1993**, *115*, 6382.
19. Hu, X.; Li, G.; Yu, J. *Langmuir* **2010**, *26*, 3031.
20. Yang, P. *The Chemistry of Nanostructured Materials*; World Scientific Publishing Co.: Singapore, 2003.
21. Bird, R. E.; Hulstrom, R. L.; Lewis, L. J. *Sol. Energy* **1983**, *30*, 563.
22. Gueymard, C. *Sol. Energy* **2004**, *76*, 423.
23. Lakowicz, J. R. *Principles of Fluorescence Spectroscopy*; Kluwer Academic/Plenum: New York, 1999.
24. Turro, N. J. *Modern Molecular Photochemistry*; University Science Books: Sausalito, 1991.
25. Hilborn *Am. J. Phys.* **1982**, *50*, 982.
26. Turro, N. J.; Ramamurthy, V.; Scaiano, J. C. *Principles of Molecular Photochemistry*; University Science Books: Sausalito, 2009.
27. Liehr, A. D.; Ballhausen, C. J. *Phys. Rev.* **1957**, *106*, 1161.
28. Pavlopoulos, T. G. *Appl. Opt.* **1997**, *36*, 4969.
29. Barranco, A.; Groening, P. *Langmuir* **2006**, *22*, 6719.
30. Yang, P.; Wirnsberger, G.; Huanng, H. C.; R., C. S.; D., M. M.; Scott, B.; Deng, T.; Whitesides, G. M.; Cmelka, G. F.; Buratto, S. K.; Stucky, G. D. *Science* **2000**, *287*, 465.

31. Del Monte, F.; Mackenzie, J. D.; Levy, D. *Langmuir* **2000**, *16,* 7377.
32. Liang, W. Y. *Phys. Edu.* **1970**, *5*, 226.
33. Frenkel, J. *Phys. Rev.* **1931**, *37*, 17.
34. Wannier, G. *Phys. Rev.* **1937**, *52*, 191.
35. Milliron, D. J.; Gur, I.; Alivisatos, A. P. *MRS Bull.* **2005**, *30*, 41.
36. Shaw, P. E.; Ruseckas, A.; Samuel, I. D. W. *Adv. Mater.* **2008**, *20,* 3516.
37. Scully, S. R.; McGehee, M. D. *J. Appl. Phys.* **2006**, *100*, 034907.
38. Haugeneder, A.; Neges, M.; Kallinger, C.; Spirkl, W.; Lemmer, U.; Feldman, J.; Scherf, U.; Harth, A.; Gugel, A.; Müllen, K. *Phys. Rev. B* **1999**, *59*, 15346.
39. Huang, J.-H.; Li, K.-C.; Chien, F.-C.; Hsiao, Y.-S.; Kekuda, D.; Chen, P.; Lin, H.-C.; Ho, K.-C.; Chu, C.-W. *J. Phys. Chem. C* **2010**, *114*, 9062.
40. Fouassier, J.-P.; Rabek, J. F. *Lasers in Polymer Science and Technology*; CRC Press: Boca Raton, 1990.
41. Bednarz, M.; Reineker, P.; Mena-Osteritz, E.; Baeuerle, P. *J. Lumin.* **2004**, *110*, 225.
42. Chung, S.-J.; Kim, K.-S.; Lin, T.-C.; He, G. S.; Swiatkiewicz, J.; Prasad, P. N. *J. Phys. Chem. B* **1999**, *103*, 10741.
43. Drobizhev, M.; Rebance, A.; Suo, Z.; Spangler, C. W. *J. Lumin.* **2005**, *111*, 291.
44. Berera, R.; van Grondelle, R.; Kennis, J. *Photosynth. Res.* **2009**, *101*, 105.
45. Goodson III, T. *Acc. Chem. Res.* **2005**, *38*, 99.
46. Xu, J.; Knutson, J. R. In *Method. Enzymol.*; Ludwig, B., Michael, L. J., Eds.; Academic Press: 2008; Vol. Volume 450, p 159.
47. So, P. T. C.; Dong, C. Y.; Masters, B. R.; Berland, K. M. *Annu. Rev. Biomed. Eng.* **2000**, *2*, 399.
48. Xu, C.; Webb, W. W. *J. Opt. Soc. Am. B* **1996**, *13*, 481.
49. Park, S.-H.; Yang, D.-Y.; Lee, K.-S. *Laser Photonics Rev.* **2009**, *3*, 1.
50. Dong, X.-Z.; Zhao, Z.-S.; Duan, X.-M. *Appl. Phys. Lett.* **2007**, *91*, 124103.
51. Denk, W.; Strickler, J.; Webb, W. W. *Science* **1990**, *248*, 73.
52. Helmchen, F.; Denk, W. *Nat. Methods* **2005**, *2*, 932.
53. Bhattacharya, P. *Semiconductor Optoelectronic Devices*; 2nd ed.; Prentice-Hall, Inc.: Upper Saddle River, 1997.
54. Sze, S. M.; Ng, K. K. *Physics of Semiconductor Devices*; 3rd ed.; John Wiley & Sons, Inc.: Hoboken, NJ, 2007.
55. Green, M. A.; Keevers, M. J. *Progress in Photovoltaics: Research and Applications* **1995**, *3*, 189.
56. Allen, J. W. *Nature* **1960**, *187*, 403.
57. Dirac, P. A. M. *P. R. Soc.* **1926**, *112*, 661.
58. Maiolo, J. R.; Atwater, H. A.; Lewis, N. S. *J. Phys. Chem. C* **2008**, *112*, 6194.
59. Price, M. J.; Maldonado, S. *J. Phys. Chem. C* **2009**, *113*, 11988.
60. Garnett, E. C.; Yang, P. J. *J. Am. Chem. Soc.* **2008**, *130*, 9224.
61. Kramer, D. *U.S. Geological Survey: Mineral Commodity Summaries*; U.S. Department of the Interior: Washington, D.C., 2006.
62. Gershenzon, M.; Mikulyak, R. M. *J. Appl. Phys.* **1961**, *32*, 1338.
63. Grimmeiss, H. G.; Rabenau, A.; Koelmans, H. J. *J. Appl. Phys.* **1961**, *32*, 2123.
64. Carmichael, R. S. *CRC Practical handbook of Physical Properties of Rocks and Minerals*; CRC Press: Boca Raton, 1989.
65. Jorgensen, C. K. *Comments Astrophys.* **1993**, *17*, 49.

66. Taylor, S. R.; McLennan, S. M. *The contental crust: Its composition and evolution*; Blackwell Sci. Publ.: Oxford, 1985. pp 330.
67. Li, J.; Peat, R.; Peter, L. M. *J. Electroanal. Chem.* **1984**, *165*, 41.
68. Yoneyama, H.; Sakamoto, H.; Tamura, H. *Electrochim. Acta.* **1975**, *20*, 341.
69. Tomkiewicz, M.; Woodall, J. M. *Science* **1977**, *196*, 990.
70. Aspnes, D. E.; Studna, A. A. *Phys. Rev. B* **1983**, *27*, 985.
71. Peat, R.; Peter, L. M. *Appl. Phys. Lett.* **1987**, *51*, 328.
72. Gerischer, H. *J. Vac. Sci. Technol.* **1978**, *15*, 1422.
73. Föll, H.; Carstensen, J.; Langa, S.; Christophersen, M.; Tiginyanu, I. M. *Phys. Status Solidi A* **2003**, *197*, 61.
74. Langa, S.; Carstensen, J.; Christophersen, M.; Föll, H.; Tiginyanu, I. M. *Appl. Phys. Lett.* **2001**, *78*, 1074.
75. Langa, S.; Carstensen, J.; Tiginyanu, I. M.; Christophersen, M.; Föll, H. *Electrochem. Solid-State Lett.* **2001**, *4*, G50.
76. Ross, F. M.; Oskam, G.; Searson, P. C.; Macaulay, J. M.; Liddle, J. A. *Philos. Mag. A* **1997**, *75*, 525.
77. Rivas, J. G.; Lagendijk, A.; Tjerkstra, R. W.; Vanmaekelbergh, D.; Kelly, J. J. *Appl. Phys. Lett.* **2002**, *80*, 4498.
78. Tjerkstra, R. W. *Electrochem. Solid-State Lett.* **2006**, *9*, C81.
79. Tjerkstra, R. W.; Rivas, J. G.; Vanmaekelbergh, D.; Kelly, J. J. *Electrochem. Solid-State Lett.* **2002**, *5*, G32.
80. van Driel, A. F.; Bret, B. P. J.; Vanmaekelbergh, D.; Kelly, J. J. *Surf. Sci.* **2003**, *529*, 197.
81. Mukherjee, J.; Erickson, B.; Maldonado, S. *J. Electrochem. Soc.* **2010**, *157*, H487.
82. Richards, D.; Zemlyanov, D.; Ivanisevic, A. *Langmuir* **2010**, *26*, 8141.
83. Flores-Perez, R.; Zemlyanov, D. Y.; Ivanisevic, A. *J. Phys. Chem. C* **2008**, *112*, 2147.
84. Kayes, B. M.; Atwater, H. A.; Lewis, N. S. *J. Appl. Phys.* **2005**, *97*, 114302(1).
85. Kelzenberg, M. D.; Turner-Evans, D. B.; Kayes, B. M.; Filler, M. A.; Putnam, M. C.; Lewis, N. S.; Atwater, H. A. In *IEEE Photovoltaic Specialists Conference* 2009; Vol. 1, p 1449.
86. Yuan, G.; Zhao, H.; Liu, X.; Hasanali, Z.; Zou, Y.; Levine, A.; Wang, D. *Angew. Chem. Int. Ed.* **2009**, *48*, 9680.
87. Krueger, O.; Jung, C.; Gajewski, H. *J. Phys. Chem.* **1994**, *98*, 12653.
88. Krueger, O.; Jung, C.; Gajewski, H. *J. Phys. Chem.* **1994**, *98*, 12663.
89. Anz, S. J.; Kruger, O.; Lewis, N. S. *J. Phys. Chem. B* **1998**, *102*, 5625.
90. Kennedy, J. H.; Frese, K. W. *J. Electrochem. Soc.* **1978**, *125*, 709.
91. Abe, R.; Tsuyoshi, R.; Hideki, S.; Domen, K. *Chem. Lett.* **2005**, *34*, 1162.
92. Feng, X.; LaTempa, T. J.; Basham, J. I.; Mor, G. K.; Varghese, O. K.; Grimes, C. A. *Nano Lett.* **2010**, *10*, 948.
93. Bhaskar, A.; Ramakrishna, G.; Hagedorn, K. V.; Varnavski, O.; Mena-Osteritz, E.; Baüerle, P.; III, T. G. *J. Phys. Chem. B* **2007**, *111*, 946.
94. Hagedorn, K. V.; Varnavski, O.; Hartwig, J.; III, T. G. *J. Phys. Chem. C* **2008**, *112*, 2235.
95. Hagedorn, K.; Forgacs, C.; Collins, S.; Maldonado, S. *J. Phys. Chem. C* **2010**, *114*, 12010.
96. Hagedorn, K.; Collins, S.; Maldonado, S. *J. Electrochem. Soc.* **2010,** *157, D558.*

Chapter 2
Exciton Trapping in an Organic Dendrimer Possessing No Energy Gradient

I. Introduction.

As a result of the search for novel materials to be used in photovoltaic devices, significant progress has been made toward understanding how excitons migrate and are controlled by both natural[1-4] and artificial organic light harvesting systems.[5-11] Kopelman, Klafter and Moore first proposed that dendrimers could be engineered as antenna where a large number of chromophores on the peripheral of the molecule could absorb light with a large cross section and subsequently transfer the energy to a single core chromophore which could perform useful work.[7,11] Energy transfer in their macromolecules occurred via Förster (hopping) mechanisms where the chromophores involved were weakly coupled (isolated). Förster hopping is possible when the donor emission spectra overlaps with the acceptor absorption spectra, the rate of this transfer is critically dependent on the extent of overlap and the distance between chromophores, as there is a $1/r^6$ distance dependence. Since these initial papers, dendrimers have been synthesized with exciton transfer efficiencies near unity.[8] In addition, multistep energy transfer dendrimers have been synthesized where the outer most chromophores have a large HOMO-LUMO gap and the innermost chromophores have a small HOMO-LUMO gap and the excitation hops sequentially through a series of chromophores with progressively smaller band gaps, a strategy which can extend the distance over which energy transfer occurs and give a larger absorption cross section.[11] However, there is more that can be done to improve energy transfer. The natural light harvesting systems LH1 and LH2 have been investigated extensively by a number of spectroscopic tools and the data implies that both Förster (hopping) and strongly coupled dynamics contribute to a near unity energy transfer efficiency over a distance of microns while preserving the

*This chapter was adapted from a published work
Hagedorn, K.; Varnavski, O.; Hartwig, J.; Goodson, T. J. Phys. Chem. C 2008, 112, 2235.

excitation energy by not requiring that the acceptor be a Stokes shift lower in energy then the donor,[3] a feat which is may be impossible with the simple Förster hopping model.

If we are to mimic nature and create highly efficient synthetic organic light harvesting systems which can efficiently transfer energy over long distances, we must find novel ways of controlling strongly coupled dynamics in multichromophore systems. Specifically, chromophore-chromophore interactions are characterized by a coupling term, *V*. In weakly coupled systems where Förster mechanisms describe energy transfer well, the absorption and emission spectra of the chromophores are unchanged with respect to the monomers. In a strongly coupled system, the excitonic states are delocalized over the involved chromophores, this can be seen in the anisotropy as a very fast decay (less than 100 fs) in non-linear systems. Since the natural light harvesting system seems to use a hopping energy transfer mechanism between groups of strongly coupled chromophores, understanding how Förster theory changes in a situation where either the donor or acceptor is a strongly coupled chromophore system has been of recent interest.[12] In this report, we use the defined dendrimeric macromolecules shown in Figure 1 as a platform for conducting studies of strongly coupled dynamics. GAA-T2 (Figure 1, top)[13] has lower symmetry than the three-fold symmetric GAA-G2 (Figure 1 bottom), which was the subject of recent photophysical studies.[10] The reduced symmetry of GAA-T2 results from connecting two triarylamine dendrons with a biphenylene unit. This core of GAA-T2 is related to the structure of *N,N'*-Bis(3-methylphenyl)-*N,N'*-diphenylbenzidine (TPD), which is commonly used as a hole transport material in applications ranging from light emitting devices[14] to bulk heterojunction photovoltaic cells.[15]

We previously showed that absorption of light by GAA-G2 generates delocalized excitons.[10] Here we show that GAA-T2 generates similar excitations in its dendrimer system, but excitons are subsequently trapped onto the core structure with over 95% efficiency without the use of an apparent gradient between the donors and acceptor chromophores.

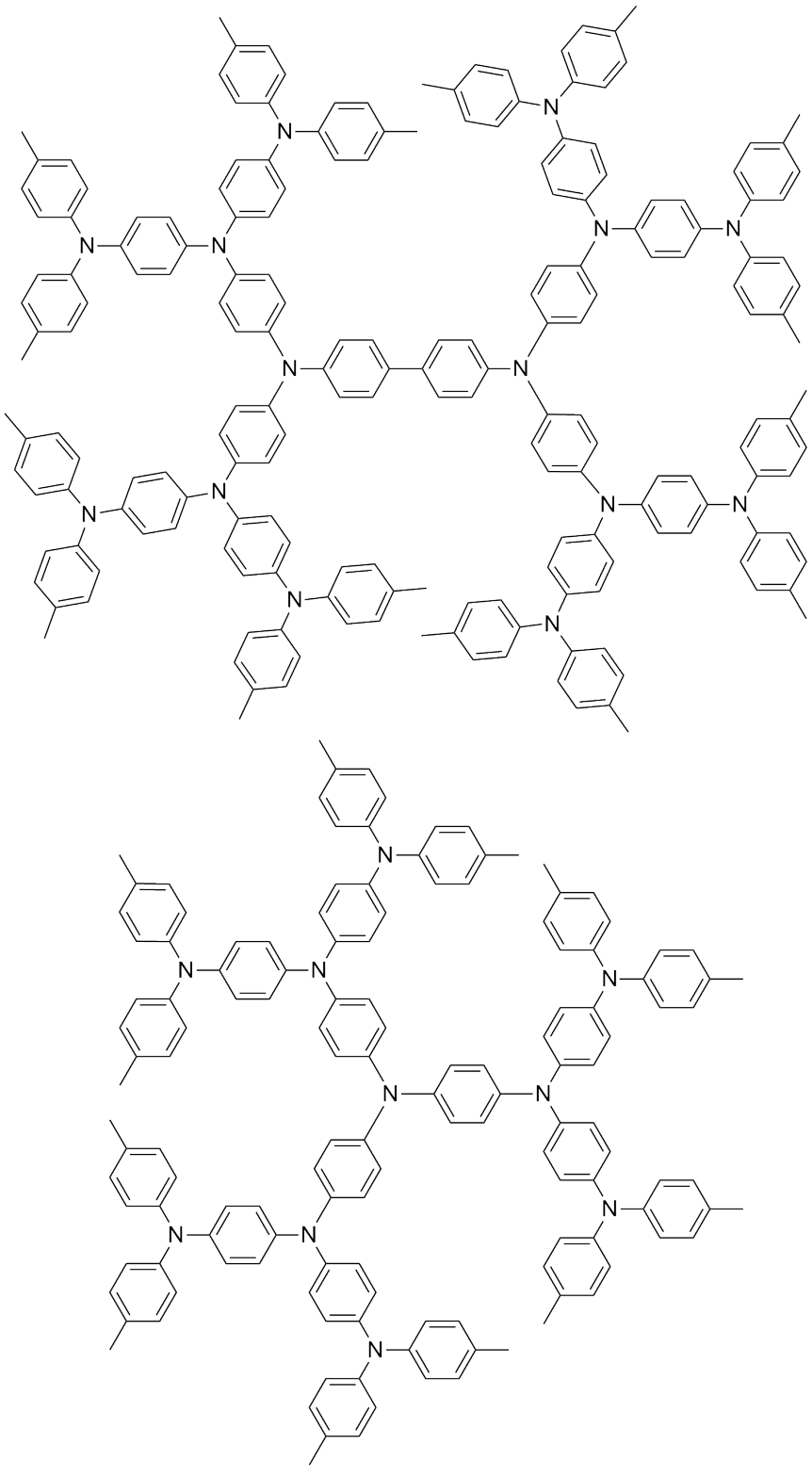

Figure 2.1. Dendrimers GAA-T2 (Top) and GAA-G2 (Bottom). GAA-G2 was previously investigated.

II. Experimental.

Materials - The preparation of these compounds is detailed in a previous work.[13] The samples were dissolved in toluene at a concentration which would give an absorbance of 0.2 to 0.6 at 385 nm in a 1 mm path length cell, an optimal value for our experiments. The actual concentrations used were 3.2×10^{-4}, 2.6×10^{-5} and 1.5×10^{-5} mol L^{-1} for compounds TPD, GAA-G2 and GAA-T2 respectively. Molar absorptivity for these compounds at 385 nm was found to be 5,698, 81,430 and 110,430 $cm^{-1}M^{-1}$ for TPD, GAA-G2 and GAA-T2 respectively.

Steady-State Measurements - The absorption spectra of the molecules were recorded using an Agilent (Model # 8341) spectrophotometer. The emission spectra were acquired using a Jobin Yvon Spex Fluoromax-2 spectrofluorimeter. The quantum yields of the molecules were measured using known procedures. Coumarin 307 was used as the standard.

Fluorescence-Lifetime Measurements - Time Correlated Single Photon Counting (TCSPC) was used to determine the fluorescence lifetimes of the dendrimers used in this study. The seed used was a mode locked Ti:Sapphire laser (Tsunami, Spectra Physics). This was amplified using a regenerative amplifier (Spitfire, Spectra Physics) which in turn was pumped by an Nd:YLF laser (Empower, Spectra Physics). The ~100 fs amplified pulses were obtained at 1 kHz, 770 nm.

Fluorescence Upconversion - Time-resolved polarized fluorescence of GAA-G2, GAA-T2 and TPD were studied using the femtosecond up-conversion spectroscopy technique. Specifically, our upconversion system used frequency-doubled light from a mode-locked Ti-sapphire laser (385 to 430nm). Polarization of the excitation beam for the anisotropy measurements was controlled using a Berek compensator. Horizontally polarized fluorescence emitted from the sample was up-converted in a nonlinear crystal of β-barium borate using a pump beam at 800 nm, which first passed through a variable delay line. Instrument response function (IRF) was measured using Raman scattering from water. Fitting the Gaussian peak from the Raman scattering yielded a sigma value of 105.9 fs which gives a full width half maximum of 243.6 fs. The excitation average power varied, but was around 0.8 ± 0.05 mW or around 1×10^{-11} J per pulse.

Fitting the Time-Resolved Fluorescence and Anisotropy - The fluorescence rise was found to have multiple components. The long rise time is well outside of the instrument response function and fitting can be accomplished without deconvolution as shown in Figure 2. Parameters for the long rise time were used as constants when deconvoluting the short rise time component from the instrument response function as shown in Figure 3. The model shown is given by the convolution of terms given in Equation 1.

$$(e^{\frac{-t^2}{2\sigma^2}})(e^{\frac{-t}{1550000}} - 0.175e^{\frac{-t}{1150}} - 0.5e^{\frac{-t}{24000}}) \quad (1)$$

The value of σ is given by the instrument response function as 105.92. This modeling shows that the time resolved fluorescence has three components, a 1.15 ps rise, a 24 ps rise and 1.55 ns decay. The 1 ps fluorescence rise is well outside of the instrument response function and contributes nearly 20% of the observed fluorescence. The major rise time component is the 24 ps component.

Energy Transfer Calculations - We calculated 95% energy transfer efficiency from the quantum yields of the three compounds. We assumed that the dendrons still had a quantum yield of 0.25% (calculated from dendrimer GAA-G2) and the core had a quantum yield of 27.8% (the QY of the small molecule). Solving Equation 2 yields 97.45%.

$$27.1 = 27.8x + 0.25(1 - x) \quad (2)$$

We feel this is a justified calculation because the anisotropy data shows that the core is not appreciably excited at 385 nm. Therefore, the high quantum yield of the dendrimer is a result of the excitation migrating from the dendrons to the core.

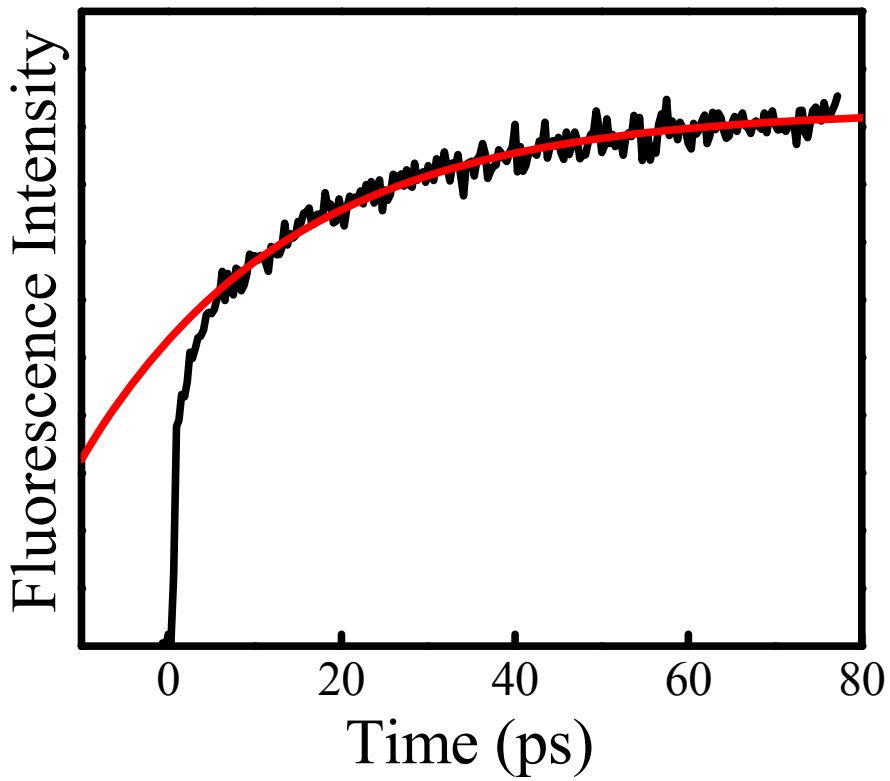

Figure 2.2. The fluorescence lifetime data is modeled with a single exponential. The time constant of the exponential rise was determined to be 24000 fs.

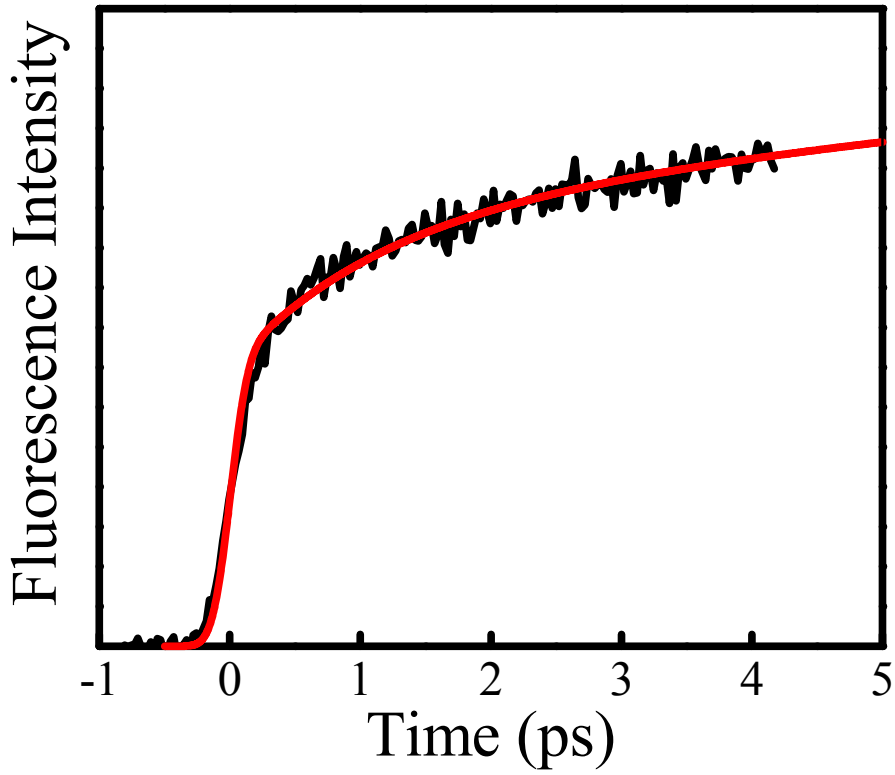

Figure 2.3. The fluorescence lifetime data was fitted with two exponentials and a Gaussian. The width of the Gaussian was 105 fs, the long lifetime exponential is modeled in Figure 2, the time constant of the short decay was found to be <100 fs.

III. Results and Discussion.

Figure 4 shows steady state spectra for TPD, GAA-G2 and GAA-T2. These spectra contain two absorption peaks at 312 nm and 354-357 nm for all three systems, and the peak shapes for the spectra of the dendrimers are similar to those of TPD with the exception that the dendrimers contain additional small absorption tails between 400 and 500 nm. The fluorescence emission bands for these systems are at 393 nm, 430 nm and 465 nm for TPD, GAA-G2 and GAA-T2, respectively. The steady state data indicates that Förster type energy transfer is not a significant mechanism in this system because the GAA-G2 dendrons are expected to have negligibly small overlap with the TPD core. Additionally, the core HOMO-LUMO gap is larger than the emission wavelength from the dendrons, making both the kinetics and thermodynamics of the Förster mechanism unfavorable. Measurements of the fluorescence quantum yield (QY) of GAA-T2, GAA-G2 and TPD were 27.1%, 2.5% and 27.8%, respectively. Thus, the QY of the GAA-T2 dendrimer is nearly as high as TPD, even though anisotropy data presented below and molar absorptivity indicates that direct excitation of the TPD unit, as an individual ch1romophore in the GAA-T2 structure, is not significant.

To probe the mechanism of energy transport in GAA-T2, additional ultrafast fluorescence measurements were performed.[9] Fluorescence upconversion results are shown in Figure 5.

Upconversion results show a rise time, which is one property that can reflect energy transfer and appears to vary between the 2-fold(GAA-T2) and 3-fold(GAA-G2) symmetric dendrimers. Upon excitation with 385 nm light, the rise time of GAA-G2 and TPD were not detected, while the rise time of GAA-T2 was clearly observed. The fluorescence rise is observed at multiple detection wavelengths and is not present in the similar sized system GAA-G2. These observations exclude the possibility that the rise is due to environmental effects and suggests that the rise is intrinsic to the structure of GAA-T2. The significance of this rise being intrinsic to the dendrimer structure is that the emitting species is gaining excited state population after the excitation pulse, an indication of energy transfer to this species. We postulate that this emitting species is associated with the TPD core because 1) the dendrimer is entirely uniform except at the core, 2) the quantum yield is similar to that of TPD (which is the structure at the core),

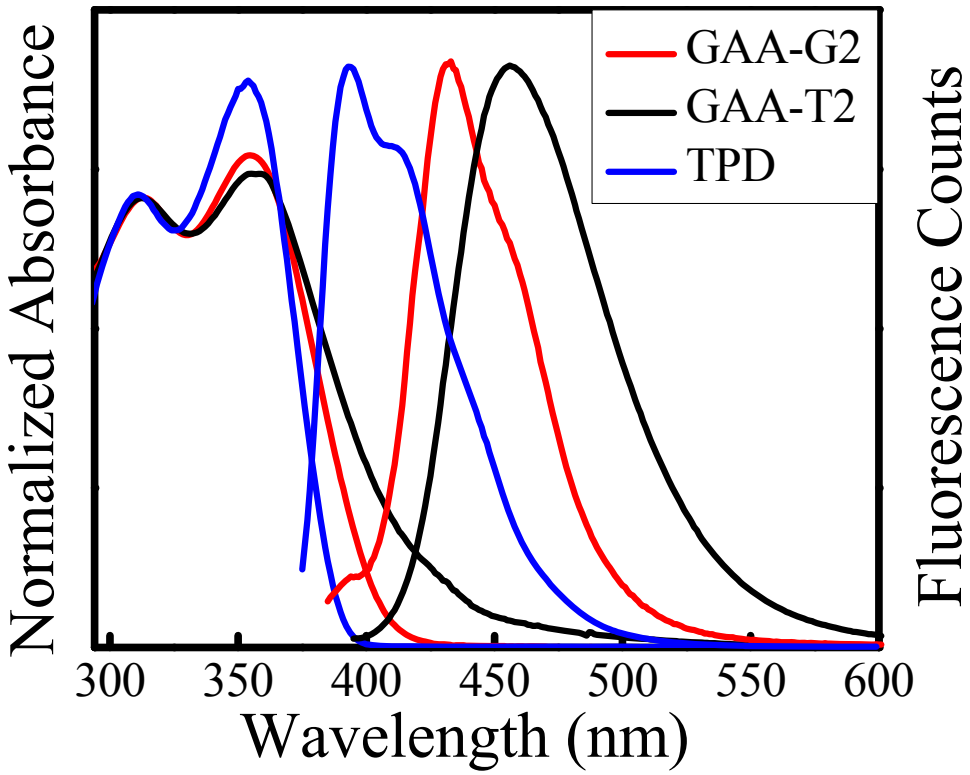

Figure 2.4. Left: steady state absorption and emission for TPD (Blue), GAA-G2 (Red) and GAA-T2 (Black). The intensity of absorbance and fluorescence has been normalized to compare spectral features.

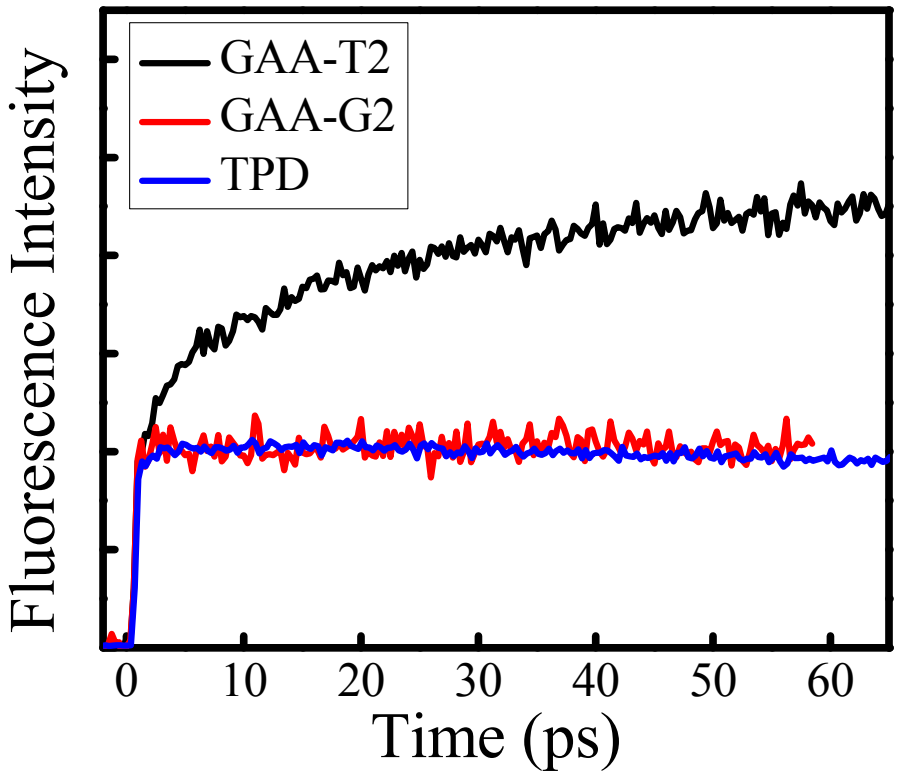

Figure 2.5. Time resolved fluorescence for these systems. All three system were excited by 385 nm light and the detection wavelength was 400, 430, 465 nm for TPD, GAA-G2 and GAA-T2, respectively. The detection wavelength was the chosen to be close to the emission maximum for each of these compounds.

and 3) the dendrons are similar to those in TAA-G2 (which had a low QY and is therefore less likely to be the emitting state).

Fitting the fluorescence rise in GAA-T2 yielded a biexponential rise time, the first time being ~1 ps and the second being ~25 ps. The 25 ps component makes the majority of the contribution to the fluorescence but both components are significant. A summary of the data is presented below in Table 1.

To further understand the energy transfer mechanism in these systems, the ultra-fast anisotropy decays were also investigated. The anisotropic data for the GAA-T2 dendrimer and TPD are shown in Figure 6. The results for GAA-G2 were reported previously.[10] Both GAA-T2 and GAA-G2 have fast coherent dynamics leading to depolarization times < 100 fs. This fast rate of anisotropy decay can only be explained by a fast delocalization of the exciton though the macromolecule. Our previous work implied that this fast anisotropy decay was due to coherent excitations in the dendron system, and such delocalized excitations are present in the GAA-T2 dendron system as well.

The ultra-fast anisotropy decay also illustrates that direct excitation of TPD, as an individual chromophore, is small. Figure 6 shows that the slow anisotropy decay of TPD occurs on the order of 124 ps while the same decay of GAA-T2 occurs in less than 100 fs. If the TPD core of GAA-T2 were excited directly, then we would expect to see a high anisotropy which was not observed.

IV. Summary.

The excitation wavelength chosen, 385 nm, is more likely to excite the dendrons then the core TPD structure, as suggested by the molar absorptivity of these compounds. The fast depolarization observed supports this supposition and also shows that the exciton is initially delocalized in the dendron system. However, the fluorescence rise and quantum yield being similar to that of TPD indicates that the exciton migrates to the core TPD structure with 95% yield. The energy in this system is collected in the dendron antenna and transferred to the core. The mechanism of this energy transfer is unlikely to be Förster because of the weak spectral overlap and lack of an energy gradient. Strongly

	GAA-T2	GAA-G2	TPD
Fluoresence QY	0.271	0.025	0.278
Fluoresence lifetime	1.55 ns	1.66 ns	0.9 ns
Fluoresence rise time	1.15 ps, 24 ps	None	None
Anisotropy Decay	<100 fs[a]	<100 fs[10,a]	124.5 ps

[a] Best fit result is faster then instrument response function

Table 2.1. Fluorescence lifetime and quantum yield

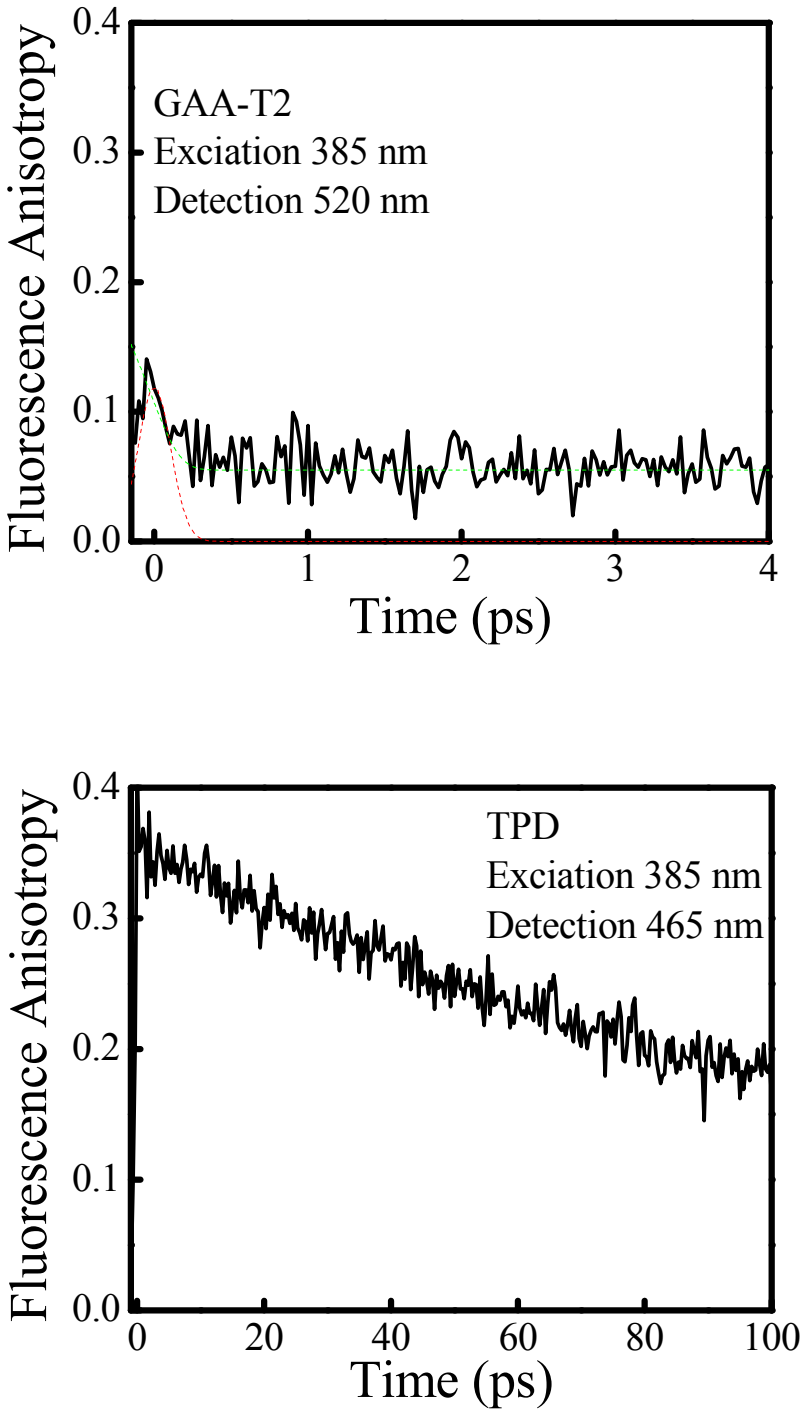

Figure 2.6. Time resolved fluorescence anisotropy. GAA-T2 is shown on the top and is given on a 5 ps scale, shown with the instrument response function (red) and fitting (green). TPD is shown on the bottom and is given on a 100 ps scale.

coupled dynamics and excited state relaxation likely play a large role in understanding the GAA-T2 system.

Organic molecules and single crystals where a delocalized exciton will become localized during excited state relaxation (exciton self-trapping) has been of interest to theoreticians for some time.[16] Recently, calculations have shown that this process can occur in a uniform linear polymer.[17] While exciton self trapping has not been previously demonstrated in dendrimers, Bardeen showed almost the opposite effect in phenylacetylene dendrimers, where weakly coupled chromophores with localized excitations became strongly coupled in the excited state and the emission was from delocalized states.[5, 6]

To explain the energy transfer phenomenon in GAA-T2 could possibly be due to exciton self-trapping. The Stokes shift of GAA-T2 is large, about 110 nm. The Stokes shift of GAA-G2 is about 75 nm. One would expect both systems to undergo similar excited state relaxations in the dendron systems, but GAA-T2 also contains the biphenylene molecule at its core which has some well studied excited state dynamics. As an isolated molecule, biphenylene is known to planarize in the excited state[18] and an analogous planarization is observed in the biphenylene rings of TPD after excitation.[19, 20] We believe that a similar excited state relaxation process occurs in GAA-T2. If the core system and dendrons in GAA-T2 are initially strongly coupled, but planarization of the biphenylene segment significantly decreases the HOMO-LUMO band gap, then the core could become more decoupled from the dendrons. The result would be an exciton which is localized on the core, rather than delocalized over the entire system. This exciton trapping during excited state relaxation (exciton self-trapping) can explain the energy transfer and does not require a gradient between HOMO-LUMO gaps of the donor and acceptors. Rather, it requires the chromophores to have similar HOMO-LUMO band gaps in the ground state (similar absorption spectra) and a strongly coupled chromophore which can undergo significant change to electronic structure in the excited state to have a decreased band gap (additional Stokes shift), which in turn decouples the chromophore from the rest of the system.

In summary, this investigation of GAA-T2 implies that energy traps with over 95% efficiencies can be created in triarylamine systems by adding biphenyldiyl linkages.

This type of controlled energy transfer in systems without energy gradients is important for the design of future organic light harvesting and energy storage devices. In addition, if the mechanism is correct, this also represents the first example of light-harvesting via exciton self-trapping in dendrimers.

V. References.

1. Engel, G. S.; Calhoun, T. R.; Read, E. L.; Ahn, T.-K.; Mančal, T.; Cheng, Y.-C.; Blankenship, R. E.; Fleming, G. R. *Nature* **2007,** *446*, 782.
2. Jimenez, R.; Dikshit, S. N.; Bradforth, S. E.; Fleming, G. R. *J. Phys. Chem.* **1996**, *100*, 6825.
3. Nagarajan, V.; Parson, W. W. *Biochemistry* **1997**, *36*, 2300.
4. vanOijen, A. M.; Ketelaars, M.; Köhler, J.; Aartsma, T. J.; Schmidt, J. *Science* **1999**, *285*, 400.
5. Gaab, K. M.; Thompson, A. L.; Xu, J.; Martinez, T. J.; Bardeen, C. J. *J. Am. Chem. Soc.* **2003**, *125*, 9288.
6. Thompson, A. L.; Gaab, K. M.; Xu, J.; Bardeen, C. J.; Martinez, T. J. *J. Phys. Chem.* **2004**, *108*, 671.
7. Devadoss, C.; Bharathi, P.; Moore, J. S. *J. Am. Chem. Soc.* **1996**, *118*, 9635.
8. Dichtel, W. R.; Hecht, S.; Fréchet, J. M. J. *Org. Lett.* **2005**, *7*, 4451.
9. Goodson III, T. *Acc. Chem. Res.* **2005**, *38*, 99.
10. Ranasinghe, M. I.; Varnavski, O. P.; Pawlas, J.; Hauck, S. I.; Louie, J.; Hartwig, J. F.; Goodson III, T. *J. Am. Chem. Soc.* **2002**, *124*, 6520.
11. Bar-Haim, A.; Klafter, J.; Kopelman, R. *J. Am. Chem. Soc.* **1997**, *119*, 6197.
12. Jang, S.; Newton, M. D.; Silbey, R. J. *Phys. Rev. Lett.* **2004**, 92, 218305.
13. Louie, J.; Hartwig, J. F. *J. Am. Chem. Soc.* **1997**, *119*, 11695.
14. Bulovic, V.; Gu, G.; Burrows, P. E.; Forrest, S. R.; Thompson, M. E. *Nature* **1996**, *380*, 29.
15. Bach, U.; Lupo, D.; Comte, P.; Moser, J. E.; Weissörtel, F.; Salbeck, J.; Spreitzer, H.; Grätzel, M. *Nature* **1998**, *395*, 583.
16. Rashba, E. I. *J. Lumin.* **2000**, *87*, 1.
17. Tretiak, S.; Saxena, A.; Martin, R. L.; Bishop, A. R. *Phys. Rev. Lett.* **2002**, *89*, 097402.
18. Beenken, W. J. D.; Lischka, H. *J. Chem. Phys.* **2005**, *123*, 144311.
19. Low, P. J.; Paterson, M. A. J.; Pushmann, H.; Goeta, A. E.; Howard, J. A. K.; Lambert, C.; Cherryman, J. C.; Tackley, D. R.; Leeming, S.; Brown, B. *Chem-Eur. J.* **2004**, *10*, 83.
20. Vragović, I.; Calzado, E. M.; García, M. A. D. *Chem. Phys.* **2006**, *332*, 48.

Chapter 3
Enhancement of Two-Photon Absorption Cross-Section in Macrocyclic Thiophenes with Cavities in the Nanometer Regime

I. Introduction.

The search for new optical devices has inspired the creation of novel materials with tailored structure-property relationships. Multi-chromophore and self-assembly approaches have been applied toward the creation of superior light harvesting, light emitting and nonlinear optical materials. This has included organic polymers, dendrimers, rotaxanes, fullerenes, and two-dimensional bis-annulene structures[1-3]. An important characteristic that is common to many of these materials is that the multi-chromophore architecture possesses collective excitations where several chromophores in the architecture contribute to the optical response. For applications involving nonlinear optical (NLO) processes, this collective behavior is utilized and it results, in some cases, to enhanced properties beyond what is expected for the isolated or localized set of chromophores. Previous reports in regards to organic branched structures have categorized the excitations in such systems as either incoherent (a hopping regime) or coherent (and strongly coupled) [4-5]. It was found that for cases of coherent interactions in multi-chromophore systems, strong enhancement of the two-photon absorption (TPA) effects was possible[6]. The investigation of this effect in several dendrimer systems has inspired possible applications in two-photon imaging and photodynamic therapy.

There have been reports which have related the structure-property relationships in certain organic materials such as conjugation length[7-8], substituents[9-10], dimensionality (dipoles, quadrupoles, and octupoles) [11-14] and intramolecular interactions[6] among others. The majority of the reports have concentrated on linear and branched architectures. In terms of particular structures, various organic chromophores have been studied for their

*This chapter was adapted from a published work
Bhaskar, A.; Ramakrishna, G.; Hagedorn, K.; Varnavski, O.; Mena-Osteritz, E.; Bäuerle, P.; Goodson, T. J. Phys. Chem. B 2007, 111, 946.

nonlinear optical (NLO) behavior as well as in photonics. In this regard, oligo- and polythiophenes are among the primary candidates for organic electronics[15-21]. They are used as hole transport materials for Organic Light Emitting Diodes (OLEDs) [22-23], Field Effect Transistors (FETs) [24-25], photovoltaic cells [26-27] and light modulators [28-29]. Thiophenes are more amenable to synthetic modifications by virtue of enhanced reactivity at the α and β positions of the thiophene ring. This enables one to synthesize a variety of molecules with systematic variations in the structure[30]. Donor-acceptor substituted thiophene derivatives have been investigated for their TPA behavior[31-32]. However, these investigations involved linear, quadrupolar molecules. To best of our knowledge, the nonlinear optical properties of thiophenes in geometries other than linear chromophores have not been explored in detail. For example, macrocyclic thiophenes with relatively large cavities have not been explored for their TPA properties or their collective excitations. Electronic structure calculations of thiophene-based systems have been investigated previously.[33] Marsella et al[34] have proposed that they can be used as molecular muscles[34]. Also, applications in biological areas have been proposed[35-37]. Other applications in opto-electronics and photonics have also been determined[38].

In this report, we present the optical properties of conjugated macrocyclic oligothiophenes in a circular geometry consisting of terthiophene and diacetylene units C[3T-DA]$_n$. The structures of the cyclo(terthiophene-diacetylenes) are presented in Figure 1. The advantage circular chromophores have over linear systems is that there are no "end-effects", which in particular in shorter oligomers influence the conjugation length and consequently the electronic and optical properties [33, 39-40]. We have studied the NLO properties of two cyclo(terthiophene-diacetylenes) with different ring sizes, the cyclodimer C[3T-DA]$_2$ and the cyclopentamer C[3T-DA]$_5$. The macrocycles include nanometer sized cavities, which renders them attractive for several potential applications. Their TPA cross section (δ) spectra were measured using Two-photon Excited Fluorescence (TPEF) method. We have also investigated the fluorescence dynamics and the excited state absorption dynamics in these systems. Because the number of [3T-DA] repeating units differ in the molecule, the chromophore density in cyclopentamer C[3T-DA]$_5$ is 2.5 times higher than in the cyclodimer C[3T-DA]$_2$. An interesting question is the cooperative enhancement in TPA cross section as a result of increase in chromophore

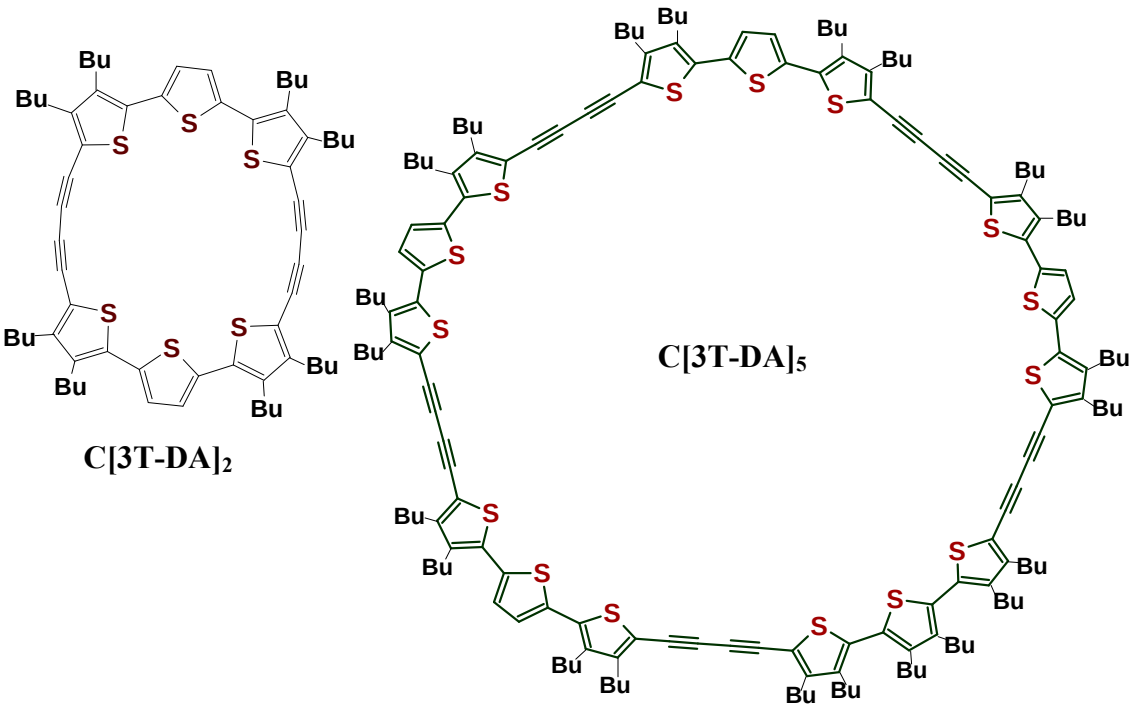

Figure 3.1. Structures of the macrocyclic terthiophene-diacetylenes studied in this investigation.

density. The extent of enhancement might elucidate the extent of intra-molecular interactions in these cyclic systems. This leads to the theoretical model of the electronic structure of these systems.

It has been found in previous theoretical studies that the main differences in the absorption spectra of cyclothiophenes in comparison to the corresponding linear oligo-thiophenes are caused by different selection rules as a consequence of their different geo-metries. The cyclothiophenes have transition dipole moments mainly arranged in the ring plane with a very small perpendicular component, which results in a forbidden S_0-S_1 transition, but allowed S_0-S_2- transition. A theoretical paper on the relation between conformations of a series of cyclothiophenes (C6T-C30T) on their electronic properties, e.g., their HOMO-LUMO energy levels and gaps has been published.[33, 41] These reports showed an increase in the coupling between excited energy levels with an increases in ring size (increase in number of monomer chromophores).

II. Experimental.

Synthesis and Structural Characterization - The synthesis of the two macrocyles used in this report has been previously reported.[38] Structural characterization using X-Ray measurements[42] of single crystals revealed have shown a nearly perfect circular shape for C[3T-DA]$_2$ and the diameter of the circular cavity was estimated to be 1.1 nm.

Steady-State Measurements - Unless stated otherwise, all the experiments were perfor-med in toluene. The absorption spectra of the molecules were recorded using an Agilent (Model # 8341) spectrophotometer. The emission spectra were acquired using a Jobin Yvon Spex Fluoromax-2 spectrofluorimeter. The quantum yields of the molecules were measured using a known procedure[43]. Coumarin 307 was used as the standard.

Two-Photon Excited Fluorescence Measurements - In order to measure the two-photon absorption cross-sections (δ), we followed the two photon excited fluorescence (TPEF) method[44]. A 1 x 10^{-4} M Coumarin 307 solution in methanol was used as the reference over a wavelength range of 700-800nm. Fluorescein (pH=11) was used as a standard over 800nm-900 nm range. In order to measure the TPA cross-sections for wavelengths less than 700nm, MSB dissolved in cyclohexane was used as the reference[45]. A mode-locked Ti:Sapphire laser (Kapteyn Murnane (KM)) was used for determining the δ over 760-

820nm. For the remaining wavelengths (630-760 nm and 820-900 nm), an Optical Parametric Amplifier (OPA-800C, Spectraphysics) was employed. The seed used was a mode locked Ti:Sapphire laser (Tsunami, Spectra Physics). This was amplified using a regenerative amplifier (Spitfire, Spectra Physics) which in turn was pumped by a Nd:YLF laser (Empower, Spectra Physics). The amplified pulses were obtained at 1 KHz, 800 nm and ~100 fs. This was used for pumping the OPA.

Fluorescence Lifetime Measurements - Time Correlated Single Photon Counting (TCSPC) was used to determine the fluorescence lifetimes of the macrocycles used in this study. The laser used was the KM system described earlier. The second harmonic from the 800 nm output was used for these measurements.

Fluorescence Upconversion - Time-resolved polarized fluorescence of C[3T-DA]$_5$ and C[3T-DA]$_2$ was studied using the femtosecond up-conversion spectroscopy technique. The upconversion system used in our experiments has been previously described[20, 62]. Specifically, our upconversion system used frequency-doubled light from a mode-locked Ti-sapphire laser (385 to 430nm). Polarization of the excitation beam for the anisotropy measurements was controlled using a Berek compensator and the rotating sample cuvette was 1 mm thick. Horizontally polarized fluorescence emitted from the sample was up-converted in a nonlinear crystal of β-barium borate using a pump beam at 800 nm, which first passed through a variable delay line. Instrument response function (IRF) was measured using Raman scattering from water. Fitting the Gaussian peak from the Raman scattering yielded a sigma value of 105.92 fs which gives a full width half maximum of 243.6 fs. Spectral resolution was achieved by using a monochromator and photomultiplier tube. The excitation average power varied, but was around 0.8 ± 0.05 mW or around 1 x 10^{-11} J per pulse.

Excited State Measurements - Transient absorption was used to investigate the excited state dynamics of the cyclic thiophenes. The pump beam was produced by the OPA-800C described above. The pump beams used in the present investigation were obtained from the fourth harmonic of signal and idler beams and were focused onto the sample cuvette. The probe beam was delayed with a computer controlled motion controller and then focused into a 2 mm sapphire plate to generate white light continuum. The white light was then overlapped with the pump beam in a 2 mm quartz cuvette containing the sample

and the change in absorbance for the signal was collected by a CCD detector (Ocean optics). Data acquisition was controlled by the software from Ultrafast systems inc. Typical power of probe beam was < 0.1 μJ while the pump beam was around ~0.5 to 1 μJ per pulse. Magic angle polarization was maintained between the pump and probe using a wave plate. The pulse duration was obtained by fitting the solvent response, which was ~130 fs. The sample was stirred with a rotating magnetic stirrer.

III. Results and Discussion.

The linear and nonlinear optical properties of the cyclothiophenes are summarized in Table 1. Results obtained from individual measurements are discussed below.

A. Steady-State Absorption and Fluorescence - The absorption and emission spectra of the cyclothiophenes are presented in Figure 2. It is interesting to note that the molecules have different absorption maxima but same emission maximum. A shoulder in the range of 440 to 500 nm is observed in C[3T-DA]$_2$. The absorption maximum at 400 nm is assigned to the S_0-S_2 transition according to the selection rules. The shoulder is therefore assigned to the S_0-S_1 transition. This shoulder is not seen in the absorption spectrum of C[3T-DA]$_5$. There is only one distinct absorption maximum at 433 nm. Hence, the S_0-S_2 transition shows a bathochromic shift attributed to increase in conjugation and it is suggested that single peak results due to the close proximity between S_2 and S_1 states, which would now be separated by a smaller energy gap. This conclusion is further corroborated by the parameter "full width at half maximum" (FWHM) which is 4000 cm^{-1} for the cyclodimer C[3T-DA]$_2$ and much larger for the cyclopentamer (5526 cm^{-1}).

The excitation spectra of the molecules are presented Figure 3. The absorption spectra are also provided for reference. It is seen that the excitation spectrum for C[3T-DA]$_2$ shows a bathochromic shift with respect to its absorption spectrum. This indicates that the emitting state is different from the absorbing state. On the other hand, no such red-shift is observed for C[3T-DA]$_5$. Based on these results, it is suggested that the absorbing state in both molecules is the S_2 state, whereas the emitting state is the S_1. This supports the suggestion regarding the close proximity of the higher excited states in C[3T-DA]$_5$. The present excitation spectrum for C[3T-DA]$_2$, along with its absorption

Molecule	λ_{abs} /nm	λ_{em} /nm	Φ [a]	δ_{max} /GM	τ_{FL} /ns
C[3T-DA]$_2$	400	540	0.04	105 (52.5)[b]	0.395
C[3T-DA]$_5$	433	541	0.12	1470 (294)[b]	0.408

[a] Quantium yield was measured at 430 nm

[b] Figures in parenthesies indicate the value for a single [3T-DA] unit

Table 3.1. Summary of the linear and nonlinear optical properties of cyclothiophenes.

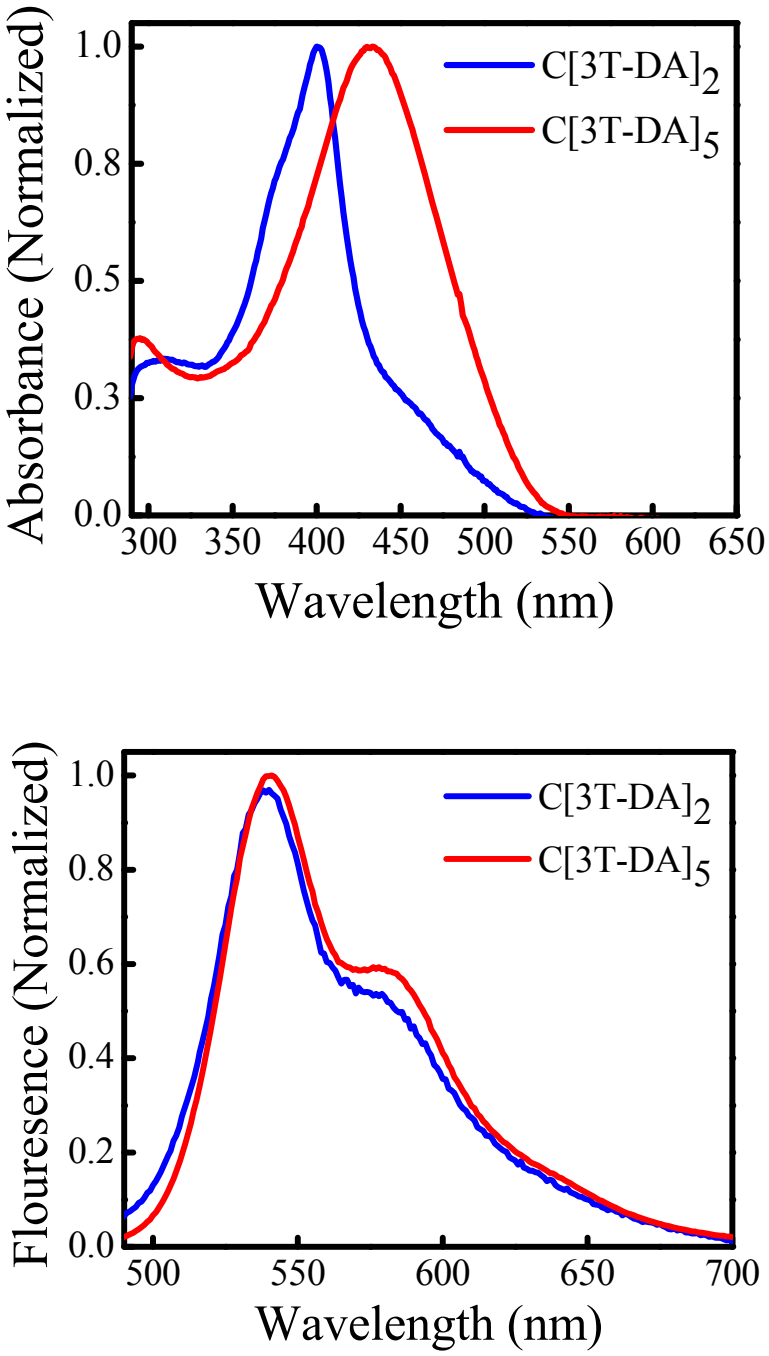

Figure 3.2. Absorption and emission spectra of $C[3T\text{-}DA]_2$ and $C[3T\text{-}DA]_5$.

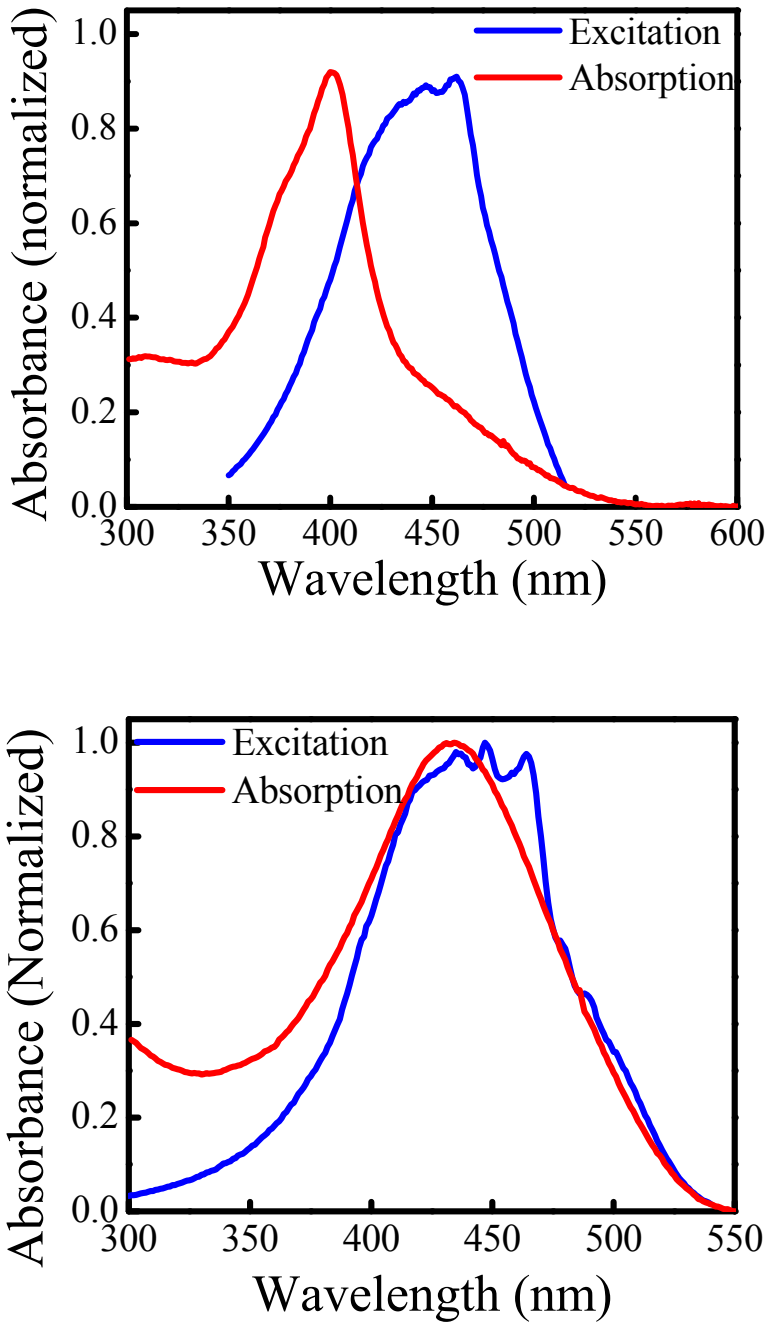

Figure 3.3. Excitation spectra of C[3T-DA]$_2$ and C[3T-DA]$_5$ respectively.

spectrum, also suggests that there is no emissive pathway from S_2 to ground state and that S_2 and S_1 states are not efficiently coupled.

B. Fluorescence Quantum Yield and Lifetime - The fluorescence quantum yields for these cyclothiophenes were measured at two excitation wavelengths, namely 400 nm and 430 nm. These corresponded to S_1 and S_2 states respectively. The fluorescence quantum yields were found to be 0.01 and 0.04 respectively for C[3T-DA]$_2$, whereas C[5T-DA]$_2$ showed a constant value of 0.12 at both excitation wavelengths. This suggests that in the case of C[3T-DA]$_2$, there is a nonradiative pathway from the S_2 state. The low quantum yields for these cyclothiophenes in general suggest that there is an efficient non-radiative decay from S_1 state (see below). Figure 4 shows the results obtained from TCSPC. The fluorescence lifetimes for C[3T-DA]$_2$ and C[3T-DA]$_5$ were found to be 395 ps and 408 ps, respectively. The similarity in fluorescence lifetimes again indicates that the emitting states are similar for both molecules. The radiative lifetimes were found to be 9.9 ns and 3.4 ns respectively.

C. TPA Cross Section - The TPA cross section (δ) spectra for both rings are shown in Figure 5. It is seen that both rings show a maxima around 760 nm, suggesting that the first TPA state has similar energetic location for both macrocyles. However, the bigger ring C[3T-DA]$_5$ shows a δ_{max} of 1470 GM which is about 14 times the δ_{max} of C[3T-DA]$_2$ (105 GM), suggesting more than an order of magnitude increase in δ. Considering that there are two [3T-DA] units, the δ per [3T-DA] unit is 52.5 GM. The same for C[3T-DA]$_5$ is 294 GM. Hence, it is seen that an increase in chromophore density by a factor of 2.5 results in 5.6 times enhancement of TPA cross-section.

The higher TPA cross-section for the larger ring suggests that the conjugation is extended over a significant fraction of the ring, if not over the entire ring. It is to be accentuated that these systems do not possess any charge transfer character. Considering the same, we believe that the δ values obtained for our cyclothiophene systems are quite large and even comparable with some of the quadrupolar derivatives reported in the literature[46]. Hence, we also suggest that by adding strong donor acceptor groups to our cyclic systems, it is possible to engineer novel molecules with even higher TPA cross sections.

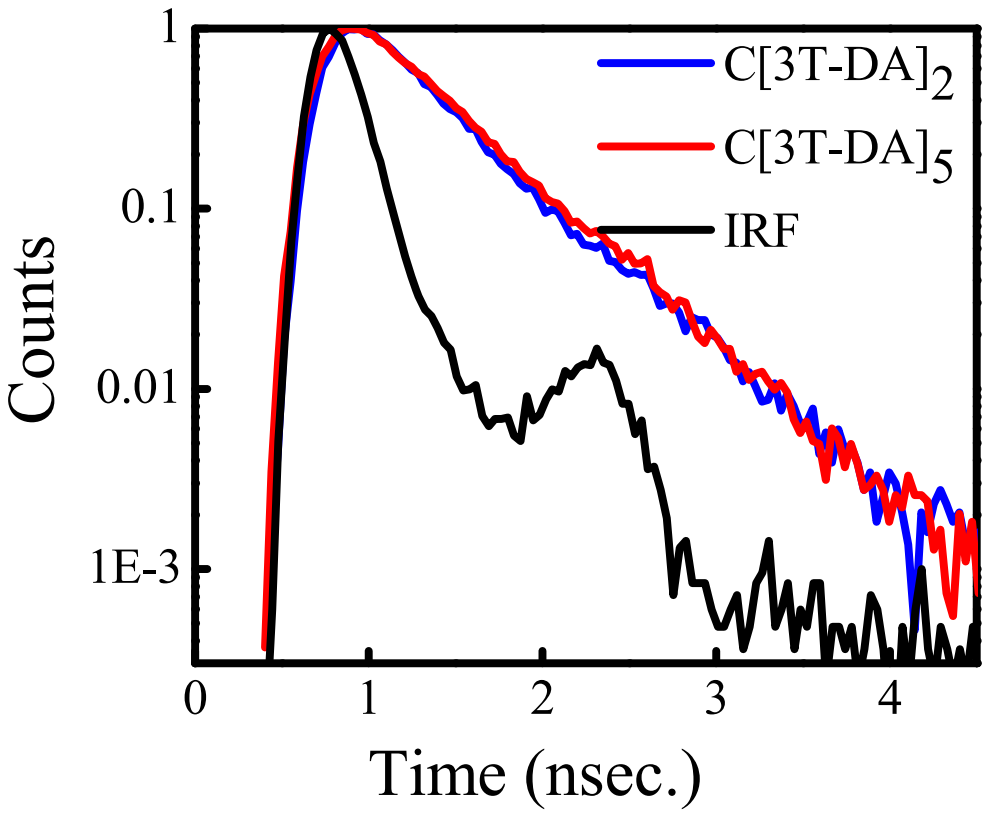

Figure 3.4. TCSPC results for $C[3T\text{-}DA]_2$ and $C[3T\text{-}DA]_5$. Also shown is the IRF, instrument response function.

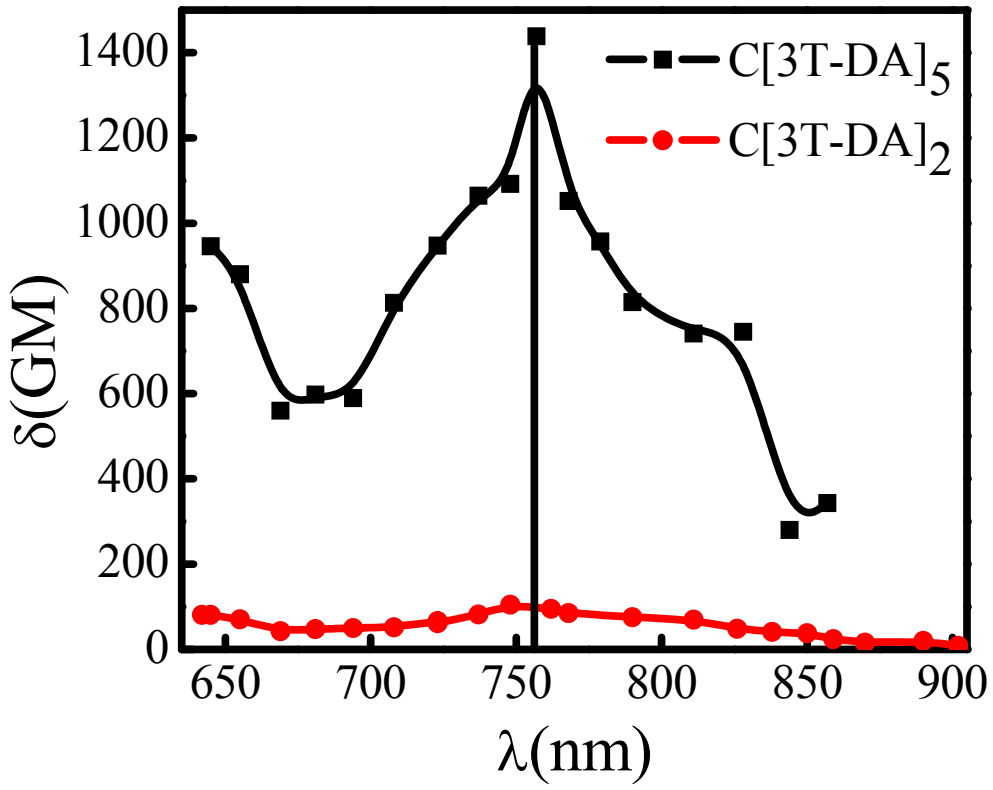

Figure 3.5. TPA cross sections of $C[3T\text{-}DA]_2$ and $C[3T\text{-}DA]_5$ at different wavelengths.

D. Transient Absorption - As mentioned above, we are interested in the mode of energy transport in these systems. In order to understand the process of excited state deactivation of the cyclo-thiophenes, ultrafast transient absorption measurements have been carried out. Figure 6 (top) shows the transient absorption at different time delays from 6 ps to 800 ps of C[3T-DA]$_2$ in Toluene after excitation at 420 nm. At a time delay of 6 ps, excited state absorption (ESA) with a maximum at 690 nm has been observed and has been ascribed to singlet-singlet absorption. As a time delay is increased from 6 ps to 800 ps, the singlet-singlet ESA decays with a growth in the region of 450 to 600 nm with a maximum at 500 nm. A clear isobestic point at 540 nm suggests that the singlet state is decayed to form a new transient which is long lived. Figure 6 (bottom) shows the kinetic decay traces at 700 nm and 490 nm. It can be clearly seen that there is a growth of transient at 490 nm and it is long lived (> 1 ns, time limit of instrument). As this ESA is long lived, it has been ascribed to triplet-triplet absorption.

However, interesting transient absorption features are observed when we follow the transient at shorter time delays. Figure 7 (top) shows the transient absorption spectra of C[3T-DA]$_2$ in toluene at time delays of 150 fs to 6 ps. Broad transient absorption from 450 to 750 nm has been observed at a time delay of 150 fs. As the time delay is increased, this broad ESA is decayed to give rise to ESA with a maximum at 690 nm with a time constant of 350 fs This broad ESA can be attributed to S_2 state's ESA. The ESA with a maximum at 690 nm has already been ascribed to singlet state excited state absorption. Kinetic traces at 490 nm and 690 nm at a very short time scale show that the initial ESA (S_2 state) decaying to give rise to the S_1 state.

Figure 7 (bottom) shows the kinetic decay trace at 520 nm and the growth of transient at 720 nm. The dynamics of growth (~350 fs) and decay clearly matched, suggesting that there is an internal conversion from S_2 (Franck-Condon) to S_1 state. However, as the excitation spectrum did not match with the absorption spectrum for C[3T-DA]$_2$, it can be concluded that there is an efficient non-radiative pathway (with a lifetime of ~300 fs) from S_2 state to some other non-radiative state. If the entire population of S_2 state is transferred to S_1 state, we might have observed a clear isobestic point at the initial time delays which is found to be absent suggesting that there is a cascade relaxation of population to another non-radiative state. However, as seen above,

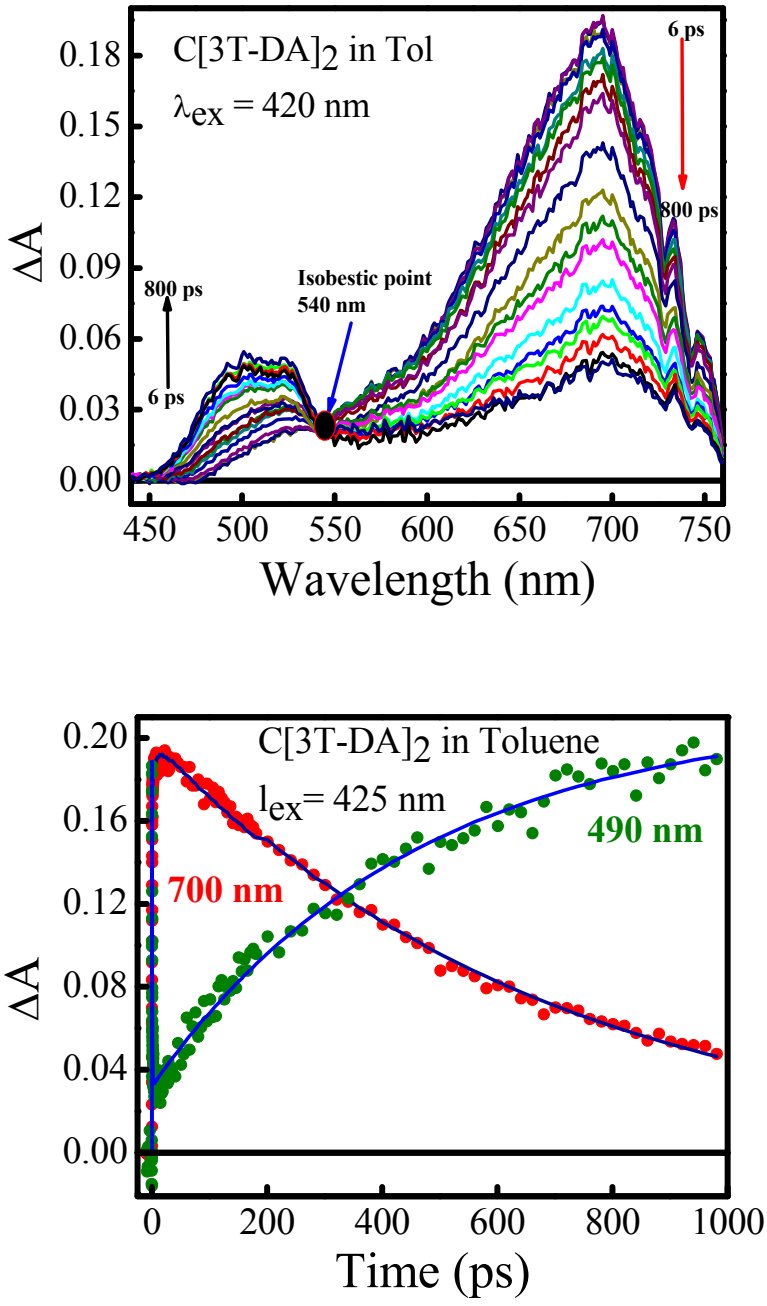

Figure 3.6. (top) Transient absorption of C[3T-DA]$_2$ in Toluene at different time delays from 6 ps to 800 ps. (bottom) Kinetic traces at 700 nm and 480 nm of C[3T-DA]$_2$ in Toluene after excitation at 420 nm.

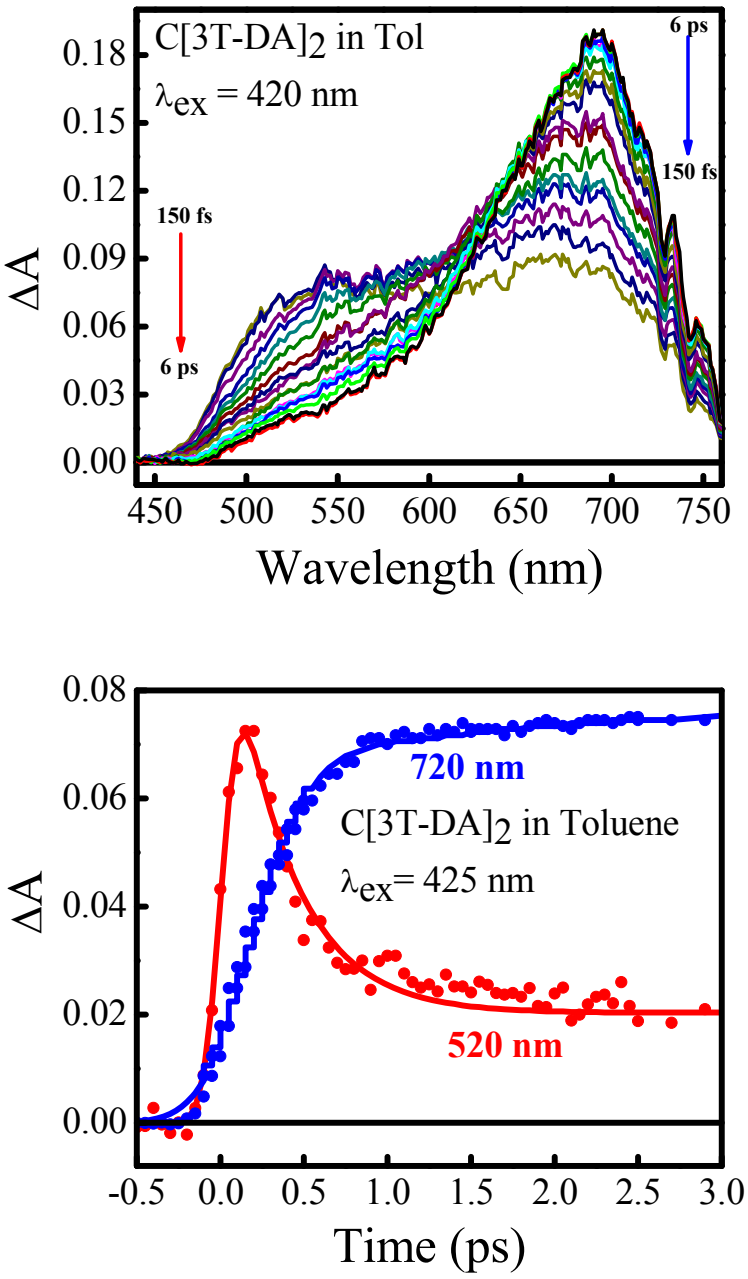

Figure 3.7. (top) Transient absorption of C[3T-DA]$_2$ in Toluene at different time delays from 150 fs to 6 ps. (bottom) Kinetic traces at 700 nm and 480 nm of C[3T-DA]$_2$ in Toluene after excitation at 420 nm.

there is an efficient population transfer from S_1 to triplet is observed (inter system crossing, ISC) (Figure 7 top) with a clear isobestic point at 540 nm and with a time constant of ~350 ps. As ISC process is a radiation less one, it explains the low fluorescence quantum yield observed for the molecule.

It has been observed from steady state emission measurements that C[3T-DA]$_5$ shows higher quantum yield than C[3T-DA]$_2$. In an effort to clarify the mechanism we have carried out transient absorption measurements of C[3T-DA]$_5$ dissolved in toluene and respective excited state absorption features and kinetics are shown in Figure 8. It can be observed that observed ESA spectral features are different from C[3T-DA]$_2$. Figure 8 (top) shows the transient absorption spectra from 5 ps to 900 ps. The transient absorption spectrum at a time delay of 6 ps consists of bleach in the region of 450 to 650 nm with characteristic bleach maxima around 490, 545 and 585 nm and a positive absorption with a maximum around 690 nm. The bleach with a maximum at 545 and 585 nm can be ascribed to stimulated emission from the S_1 state. However, the bleach with a maximum at 490 nm is due to the disappearance of ground state. As the time delay is increased, the bleach has decayed to give rise to a positive transient. The transient absorption spectrum at 900 ps had shown a positive absorption spectrum whole in the visible region from 450 to 750 nm with maxima around 520 nm and 690 nm. It has been observed from fluorescence measurements that the lifetime of the S_1 state of the molecule is around 400 ps and thus the transient present at 900 ps can be attributed to triplet-triplet absorption.

It can be observed from the kinetic trace shown in Figure 8 (middle) that the stimulated emission recovers back to give rise to positive ESA corresponding to triplet state absorption. The growth of this triplet is found to be around 300 ps, which is comparable to the observed fluorescence lifetime. However, Figure 8 (middle) shows no decay to form a triplet state. This can be because of the overlapping absorptions of singlet and triplet states. It can be observed from the kinetics shown in Figure 8 (middle) and 8 (bottom) that there exist interesting excited state dynamics at early time scales. Shown in Figure 9 (top) is the transient absorption spectrum of [C-3TDA]$_5$ in shorter time window (from 150 fs to 5 ps). Immediately after the photoexcitation, negative absorption with a maximum at 480 nm and positive absorptions with maxim around 540 nm and 700 nm are observed. The negative absorption at 480 nm is due to the bleach of ground state

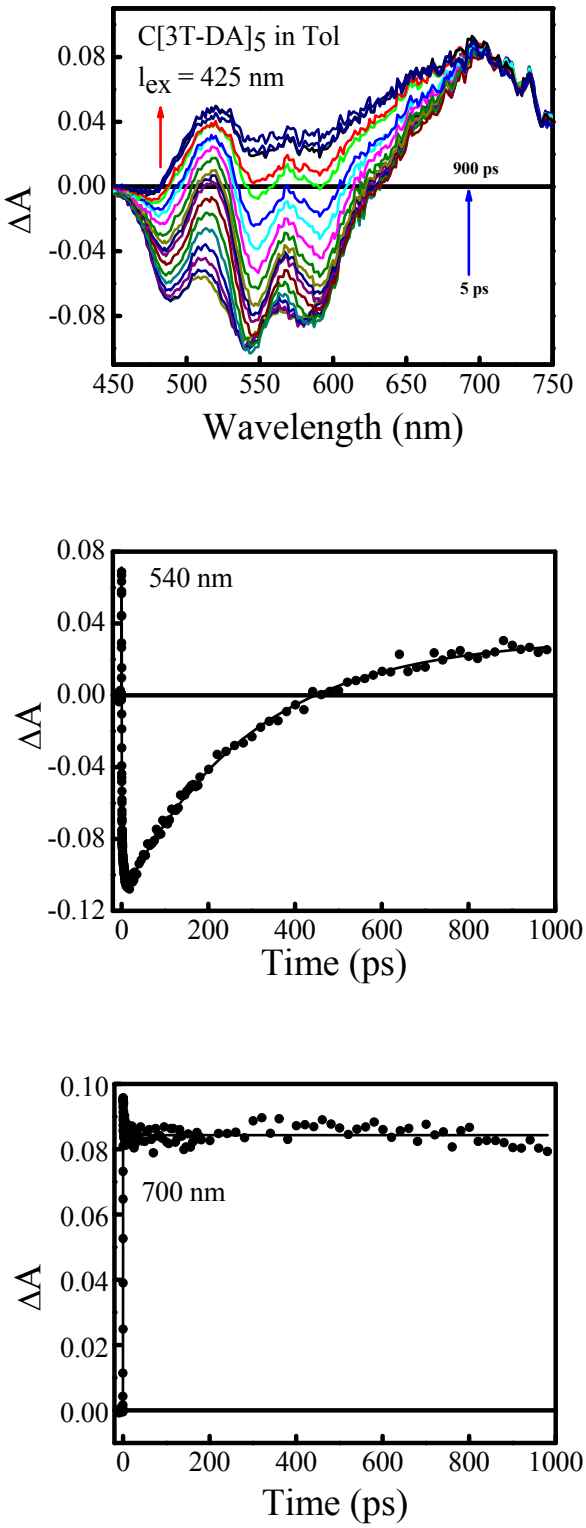

Figure 3.8. (top) Transient absorption spectra at different time delay from 6 ps to 800 ps of $[C\text{-}3TDA]_5$ in toluene. (middle) Kinetic trace at 540 nm (bottom) Kinetic decay trace at 700 nm.

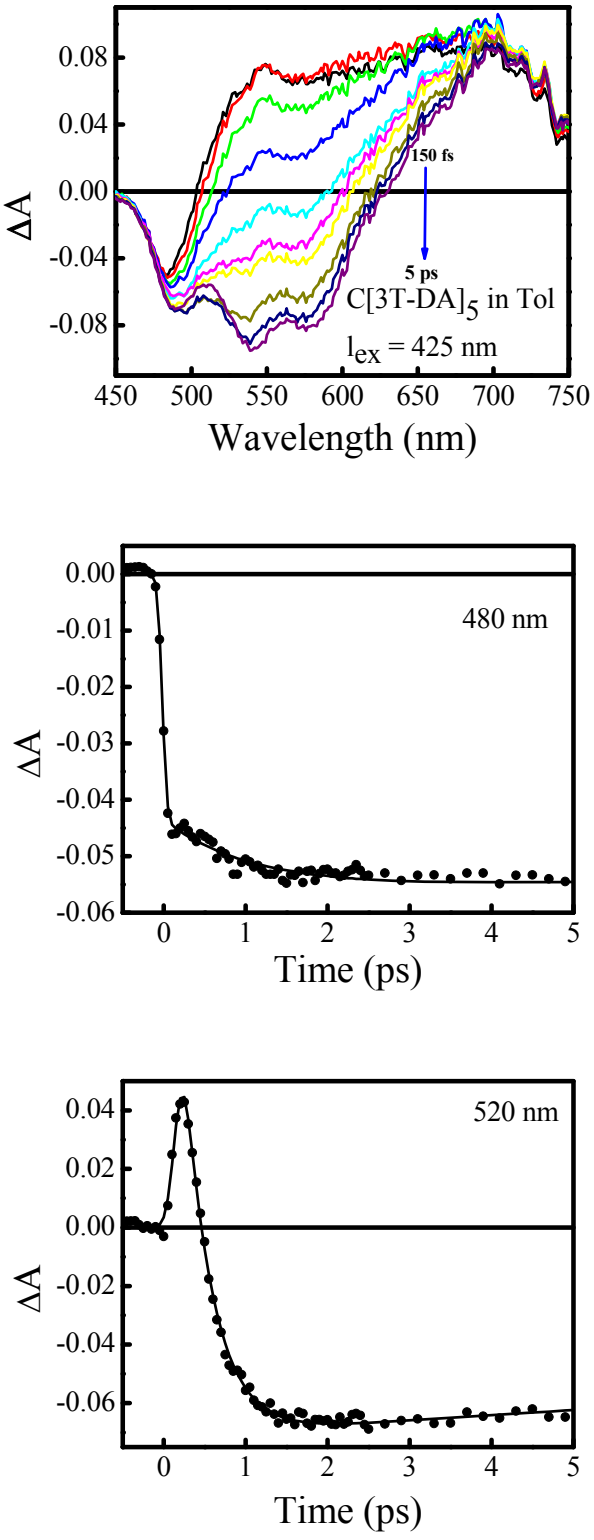

Figure 3.9. (top) Transient absorption spectra at of $[C\text{-}3TDA]_5$ in toluene in shorter time window from 150 fs to 5 ps. (middle) Kinetic trace at 480 nm (bottom) Kinetic decay trace at 520 nm.

absorption. The positive absorption bands at 480 nm and 700 nm can be ascribed to the ESA of S_2 state. The fact that the S_2 state's ESA is decaying to S_1 state emission unambiguously suggest that S_2 and S_1 states are intimately connected.

Kinetic decay trace corresponding to bleach of ground state absorption is provided in Figure 9 (middle). The fact that there is no recovery of bleach suggest that there is no ultrafast pathway from S_2 state back to ground state and the S_2 state is decaying to give the stimulated emission from S_1 state. This information is further established by the kinetic decay trace at 520 nm shown in Figure 9 (bottom). Global fit analysis had shown that the decay time from S_2 state to S_1 state is around 460 fs. Presence of another non-radiative state in C[3T-DA]$_2$ observed from the transient measurements explain the lower quantum yield in C[3T-DA]$_2$ than C[3T-DA]$_5$. The results further suggest the proximity between S_2 and S_1 states and efficient coupling between them in C[3T-DA]$_5$. Hence, these detailed transient absorption measurements confirm the existence and importance of the S_2 and S_1 states. These results also compare and elucidate the efficiency of coupling between the two states and also explain the differences in observed fluorescence quantum yields of the thiophene macrocycles.

E. Fluorescence Upconversion - We have also carried out fluorescence up conversion measurements to investigate the mode of energy transport in the thiophene macrocycles C[3T-DA]$_5$ and C[3T-DA]$_2$. This technique has been extensively used to probe energy transport properties in a number of branched and macromolecular architectures.[4] After obtaining parallel and perpendicular polarized fluorescence measurements, Equation 1 was used to find the anisotropy.[47]

$$\Gamma = \frac{I_{par} - I_{per}}{I_{par} + 2I_{per}} \qquad (1)$$

Depolarization of the emission can be caused by a number of phenomena, for these molecules only two depolarization times were observed, one was very fast (less than 100 fs) the other was very slow (over one nanosecond). The first depolarization is a fast process due to migration of the exciton to other chromophores in the ring, the second depolarization is due to rotational diffusion. After deconvoluting the data from the

instrument response function (Figure 10), it was found that the initial anisotropy decay in C[3T-DA]$_5$ was 27 ± 10 fs, this supports a coherent transport of excitons. A Förster hopping mechanism would be excluded with these results because Förster hopping occurs on the order of picoseconds. In this case, the Förster energy transfer mechanism cannot be applied with physically reasonable parameters when energy transfer is so fast. Similarly, the system C[3T-DA]$_2$ has an initial anisotropy decay of 20 ± 10 fs, thus our data supports a coherent energy migration in both systems. We can compare these systems to the natural photosystem LH2 of the purple bacteria *Rhodobacter sphaeroides* which has nine chromophores and experiences a combination of Förster and wavelike energy migration. The natural system LH2 presents two anisotropy decay times of 100 fs and 300-500 fs. 100 fs is too fast for Förster type energy migration, but the presence of the 300-500 fs decay supports the theory of an LH2 photosystem where the energy is delocalized over four chromophores and hops to the remaining chromophores.[48]

Initially, chromophore transition moments are oriented randomly in a plane, and the residual fluorescence anisotropy value is 0.1.[47] After the initial anisotropy decay, the steady state anisotropy value of C[3T-DA]$_5$ was calculated to be 0.081 ± .01 with little observed anisotropy decay for up to 200 ps. The rotational diffusion time of C[3T-DA]$_5$ was crudely calculated using the Debye-Stokes-Einstein (DSE) equation to be longer than one nanosecond, a timescale considerably longer than the time scales we observed which explains why a significant drop in anisotropy up to 200 ps due to rotational diffusion was not observed.[47] The smaller ring system C[3T-DA]$_2$ had a anisotropy residual value of 0.11 ± .01 and a decrease in anisotropy due to rotational diffusion was apparent and by fitting the data to a exponential decay the rotational diffusion was calculated to be 850 ps. Terthiophene, an oligomer with three thiophene rings, has a rotational diffusion time of 175 ps.

We suggest that there are two ways for which we can account for the residual anisotropy of C[3T-DA]$_5$ being 0.081 ± .01 while the theoretical anisotropy for a planar system is 0.1. Either some fraction of the rings are deformed from a planar arrangement, or the chromophores are twisted with respect to the plane of the molecule. Demidov and Andrews discussed the effect of chormophore orientation with respect to the plane of the ring on the residual anisotropy and obtained from Equation 2.[49]

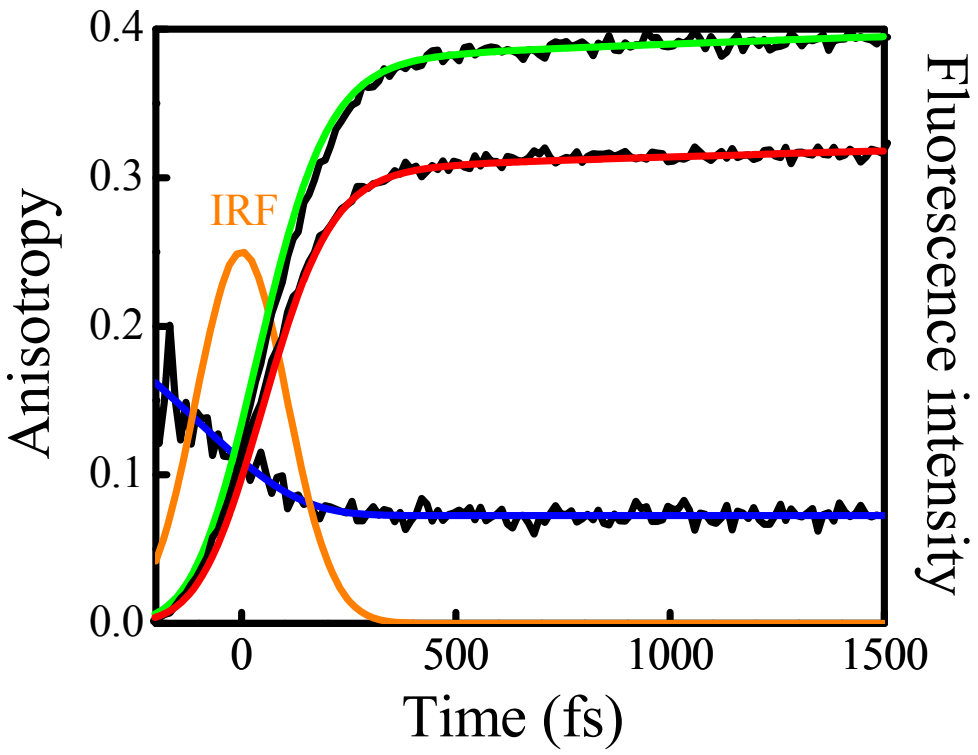

Figure 3.10. Raw data shown in the parallel and perpendicular measurements above is convoluted with the instrument response function. A mathematical procedure removes the instrument response function leaving the experimental decay, shown in the anisotropy curve.

$$R = 0.1\left(9Cos^4(\theta) - 6Cos^2(\theta) + 1\right) \quad (2)$$

Using this formula we can calculate that if the anisotropy of our system is 0.081 and a planear system is expected to have an anisotropy of 0.1, then the difference could be explained if the chromophores average inclination angle with respect to perpendicular is 7.9 ± 1 degrees.

The average value for the anisotropy decay time was found to be 27 fs. Combining this with spectroscopic information can give us an idea of the type of energy transfer (exciton or hopping dynamics).[47-49] A large homogeneous linewidth would indicate strong interaction between the environment and the chromophores, lending to a hopping type energy transfer, while fast anisotropy decay times would indicate strong interaction between chromophores and lend to wavelike energy transfer.[47-49] This is a relatively simple approach which neglects inhomogenous line broadening and can be quantified by an equation developed by Leegwater.[47] Equation 3 s a general expression for the anisotropy decay rate k_{dep} in a ring molecular system at high temperature.

$$k_{dep} = \Gamma\left(1 - \frac{1}{N}\sum_{k=1}^{N} \frac{\Gamma^2}{\Gamma^2 + 16J^2 \sin^2\left(\frac{2\pi}{N}\right)\sin^2\left(\frac{2\pi k}{N}\right)}\right) \quad (3)$$

In this equation Γ is the homogeneous linewidth and N the number of chromophores. For a system of 5 chromophores the expression becomes Equation 4.

$$k_{dep} = \frac{7.236\Gamma\left(\Gamma^2 + 7.236J^2\right)J^2}{\left(\Gamma^2 + 5J^2\right)\left(\Gamma^2 + 13.09J^2\right)} \quad (4)$$

We obtained plots of the decay time vs interaction strength in order to estimate the mode of energy transport in the thiophene macrocycles. Each curve represented a different value of gamma in Equation 4. Utilizing this model, our time-resolved

depolarization data places the anisotropy decay time at 27 fs, which according to the Leegwater's theory would mean that excitation transfer in this system cannot be accounted for by pure Förster hopping mechanism and the excitation delocalization over substantial part of the ring should be considered.

IV. Summary.

In conclusion, we have investigated the linear and nonlinear optical properties of two new conjugated macrocycles containing terthiophene-diacetylenes as repeat units. We were also able to experimental examine the nature and coupling between the electronic states in these thiophene rings. The absorption spectrum for $C[3T\text{-}DA]_2$ showed almost decoupled S_1 and S_2 states, whereas $C[3T\text{-}DA]_5$ did not due to the red-shift of the S_2 state and subsequent coupling between S_1 and S_2. Quantum yields at different excitations suggested the presence of an efficient nonradiative pathway from S_2 in case of $C[3T\text{-}DA]_2$. TCSPC and emission spectra suggested the possibility of similar absorbing and emitting states for $C[3T\text{-}DA]_5$ while the absorption and emission states were found to be different for $C[3T\text{-}DA]_2$. TPA cross section spectra determination showed that $C[3T\text{-}DA]_5$ showed a 550% enhancement over $C[3T\text{-}DA]_2$. Ultrafast transient absorption measurements elucidated the excited state dynamics and provided the proof for the presence of S_1 and S_2 excited states in case of $C[3T\text{-}DA]_2$ and $C[3T\text{-}DA]_5$. It corroborated the suggestion regarding efficient coupling between S_2 and S_1 states in case of $C[3T\text{-}DA]_5$ while it may not be the case for $C[3T\text{-}DA]_2$. The presence of a triplet state is observed for both cyclothiophenes and the ISC of S_1 to T_1 state is provides an efficient non-radiative pathway. Fluorescence upconversion showed good inter-chromophore coupling within the macrocycles and a planarized geometry of the emitting state. We believe that the TPA cross sections obtained for these thiophene rings are quite large and can be further enhanced by adding donor and acceptor groups to the cyclic systems, rendering them attractive for potential optical and possibly electronic applications.

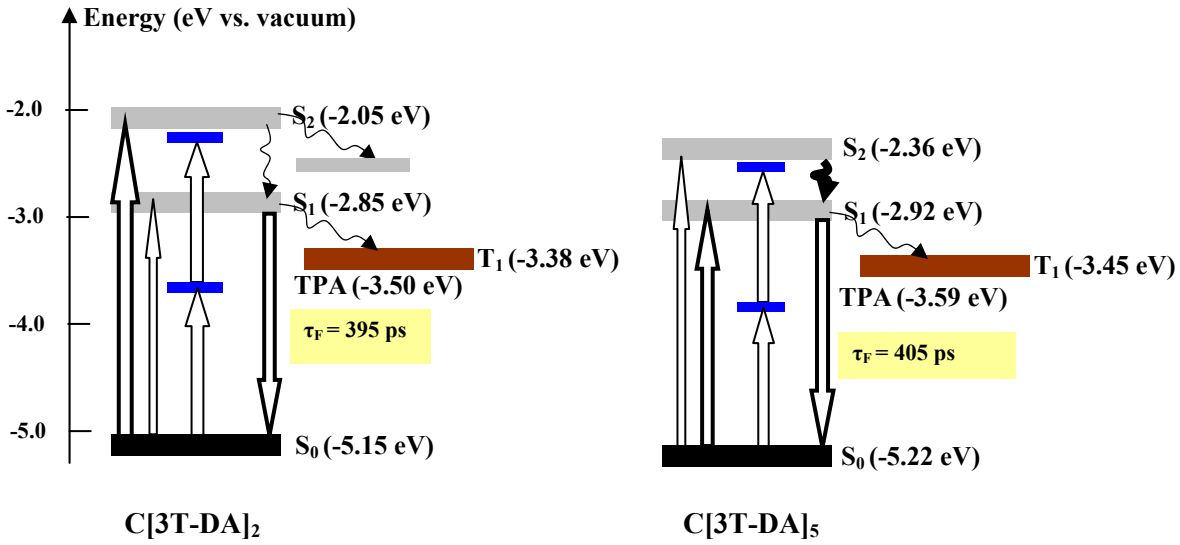

Figure 3.11. Energy level diagram for cyclo(terthiophene-diacetylenes) C[3T-DA]$_2$ and C[3T-DA]$_5$. The energies for the S_0 ground states are taken from cyclic voltammetry and the potential of the ferrocene/ ferricenium reference electrode set to -4.8 eV vs. vacuum. The other energy levels are taken from the optical investigation.

V. References.

1. McQuade, D. T.; Hegedus, A. H.; Swager, T. M. *J. Am. Chem. Soc.* **2000**, *122*, 12389.
2. Franco, C.; Wilson, J. S.; Jasper, M. J.; Clement, D.; Silva, C.; Friend, R. H.; Severin, N.; Samori, P.; Rabe, J. P.; O'Connell, M. J.; Taylor, P. N.; Anderson, H. L. *Nat. Mater.* **2002**, *1*, 160.
3. Bhaskar, A. ; Ramakrishna, G. ; Haley, M. M.; Goodson III, T., *J. Am. Chem. Soc.* **2006**, 128(43), 13972.
4. Goodson III, T. *Acc. Chem. Res.*, **2005**, *38*, 99. b) Goodson III, T. *Ann Rev. Phys. Chem.*, **2005**, *56*, 581
5. Varnavski, O. P.; Ostrowski, J. C.; Sukhomlinova, L.; Twieg, R. J.; Bazan, G., C.; Goodson III, T. *J. Am. Chem. Soc.* **2002**, *124*, 1736.
6. Wang, Y.; He, G. S.; Prasad, P. N.; Goodson III, T. *J. Am. Chem. Soc.* **2005**, *127*, 10128.
7. Albota, M. *Science* **1998**, *281*, 1653.
8. Reinhardt, B. A.; Brott, L. L.; Clarson, S. J.; Dillard, A. G.; Bhatt, J. C.; Kannan, R.; Yuan, L.; He, G. S.; Prasad, P. N. *Chem. Mater.* **1998**, *10,* 1863.
9. Mongin, O.; Porres, L.; Moreaux, L.; Mertz, J.; Blanchard-Desce, M. *Org. Lett.*, **2002**, *4*, 719.
10. Brunel, J.; Mongin, O.; Jutand, A.; Ledoux, I.; Zyss, J.; Blanchard-Desce, M. *Chem. Mater.*, **2003**, 1*5*, 4139.
11. Beljonne, D.; Wenseleers, W.; Zojer, E.; Shuai, Z.; Vogel, H.; Pond, S. J. K.; Perry, J. W.; Marder, S. R.; Bredas, J.-L. *Ad*v. *Funct. Mater.* **2002**, *12*, 631.
12. Wang, Y.; Ranasinghe, M. I.; Goodson III, T. *J. Am. Chem. Soc.* **2003**, *125*, 9562.
13. Varnavski, O. P.; Ostrowski, J. C.; Sukhomlinova, L.; Twieg, R. J.; Bazan, G., C.; Goodson III, T. *J. Am. Chem. Soc.* **2002**, *124*, 1736.
14. Katan, C.; Terenziani, F.; Mongin, O.; Werts, M. H. V.; Porre´s, L.; Pons, T.; Mertz, J.; Tretiak, S.; Blanchard-Desce, M. *J. Phys. Chem. A* **2005**, *109*, 3024.
15. Martin, R. E.; Diederich, F. *Angew. Chem. Intl. Ed.* **1999**, *38*, 1350.
16. Meier, H. *Angew. Chem.* **1992**, *104*,1425.
17. Kraft, A. ; Grimsdale, A. C.; Holmes, B. C. *Angew. Chem.* **1998**, *110*, 416.
18. Loutfy, R. O.; Hor, A. M..; Hsiao, C. K.; Baranyi, G.; Kazmaier, P. *Pure. Appl. Chem.* **1988**, *60*, 1047.
19. Feringa, L.; Jager, W. F.; de Lange, B. *Tetrahedron* **1993**, *49*, 8267.
20. Marsella, M. J.; Yoon, K.; Tham, F. S. *Org. Lett.* **2001**, *3*, 2129.
21. Dürr, H. *Angew. Chem.* **1989**, *101*, 427.
22. Kraft, A. ; Grimsdale, A. C.; Holmes, B. C. *Angew. Chem.* **1998**, *37*, 403.
23. Thompson, J.; Blyth, R. I. R.; Mazzeo, M. *Appl. Phys. Lett.* **2001**, *79*, 560.
24. Katz, H. E.; Laquindanum, J. G.; Lovinger, A. J. *Chem. Mater.* **1998**, *10*, 633.
25. Horowitz, G. *Adv. Mater.* **1998**, *10*, 365.
26. Noma, N.; Tsuzuki, T.; Shirota, Y. *Adv. Mater.* **1995**, *7*, 647.
27. Noda, T.; Imae, I.; Noma, N.; Shirota, Y. *Adv. Mater.* **1997**, *9*, 239.
28. D. Fichou, D.; Nunzi, J. M.; Charra, F.; Pfeffer, N. *Adv. Mater.* **1994**, *6*, 64.
29. McCullough, R. D.; *Adv. Mater.* **1998**, *10*, 93.
30. Müllen, K.; Wegner, G. *Electronic Materials: The Oligomer Approach*, 2nd ed.; Wiley-VCh: Weinheim, 1998, pp. 105-197.

31. Zhao, M. –T.; Singh, B. P.; Prasad, P. N.; *J. Chem. Phys.* **1988**, *89*, 5535.
32. Marder, S. R.; Kippelen, B.; Jen, A. K.; Peyghambarian, N. *Nature* **1997**, *388*, 845.
33. Bednarz, M.; Reineker, P.; Mena-Osteritz, E.; Baeuerle, P. *J. Lumin.,* **2004**, *110*, 225.
34. Marsella, M. J.; *Acc. Chem. Res.* **2002**, *35*, 944.
35. Brault, L.; Miginau, E.; Neguesque, A.; Battaglia, E.; Bagrel, D.; Kirsch, G. *Eur. J. Med. Chem.* **2005**, *40*, 757.
36. Sarkar, A.; Haley, M. M. *Chem. Comm.* **2000**, *18*, 1733.
37. Yamada, T.; Azumi, R.; Hiroaki, S.; Hideki, A.; Abe, M.; Baeuerle, P.; Matsumoto, M. *Chem. Lett.* **2001**, *10*, 1022.
38. Kroemer, J.; Carreras, I. R.; Fuhrmann, G.; Musch, C.; Wunderlin, M.; Debaerdemaker, T.; Mena-Osteritz, E.; Baeuerle, P. *Angew. Chem. Intl. Ed.*, **2000**, *39*, 3481.
39. Chung, S.-J.; Kim, K.-S.; Lin, T.-C.; He, G. S.; Swiatkiewicz, J.; Prasad, P. N. *J. Phys. Chem. B* **1999**, *103*, 10741.
40. Drobizhev, M.; Rebane, A.; Suo, Z.; Spangler, C. W. *J. Lumin.* **2005**, *111*, 291.
41. Baeuerle, P. *Adv. Mater.*, **1992**, *4,* 102.
42. Fuhrmann, G.; Debaerdemaker, T.; Baurerle, P. *Chem. Comm.* **2003**, *8*, 949.
43. Maciejewski, A.; Steer, R. P. *J. Photochem.* **1986**, *35*, 59.
44. Xu, C.; Webb, W. W.; *J. Opt. Soc. Am. B* **1996**, *13*, 481.
45. Beljonne, D.; Wenseleers, W.; Zojer, E.; Shuai, Z.; Vogel, H.; Pond, S. J. K.; Perry, J. W.; Marder, S. R.; Bredas, J.-L. *Adv. Funct. Mater.* **2002**, *12*, 631.
46. Zhao, M. –T.; Singh, B. P.; Prasad, P. N. *J. Chem. Phys.* **1988**, *89*, 5535.
47. Leegwater, J. A. *J. Phys. Chem*. **1996**, *100*, 14402.
48. Bradforth, S. E.; Jimenez, R.; VanMourik, F.; van Grondelle, R.; Fleming, G. *J. Phys. Chem.* **1995**, *99*, 16179.
49. Demidov, A.; Andrews, D. *Photochem. Photobiol*. **1996**, 63(1), 39.
50. Kumble, R.; Palese, S.; Visschers, R.; Dutton, P.; Hochstrasser, R. *Chem. Phys. Lett*. **1996**, *261*, 396.

Chapter 4
Preparation and Photoelectrochemical Activity of Macroporous p-GaP(100)

I. Introduction.

Phosphide semiconductors have attractive optoelectronic properties for solar-powered H_2O splitting systems. Multiple phosphides show chemical stability in water and demonstrate appropriate bandgap energetics.[1-8] Notably, indium-based phosphides decorated with Pt electrocatalysts are the most active known materials for using sunlight to reduce H^+ to H_2 in water.[4,6,9-11] However, the scarcity of raw indium (In) precludes the practical use of In-phosphides in solar energy technologies at scale. Gallium phosphide (GaP) is a related phosphide with potentially compatible photoelectrochemical properties for photoelectrochemical fuel production.[3,10,12-16] Both Ga and P are among the most plentiful elements on the surface of the earth, with Ga nearly as abundant as zinc (Zn) and several orders of magnitude more prevalent than indium, tungsten, or molybdenum.[17] The Shockley-Quiessier energy conversion efficiency limit at an optimized GaP heterojunction is 20% at under solar insolation.[18] Notably, GaP has already been utilized for decades in commercial light emitting diodes, a testament to the usability and feasibility of GaP as a material for optoelectronic technologies at scale.[19-21]

Although GaP is a technologically mature material, two distinct challenges have prevented the development of GaP-based light harvesting technologies. First, GaP interfaces are prone to deleterious oxidation. New chemical strategies have been recently reported to address these issues.[22-23] The second limitation is the weak absorption of visible light by thin GaP films. Short minority carrier diffusion lengths relative to the depth of penetration by visible photons result in substantially decreased photocurrent densities. As a result, the attainable solar energy conversion efficiency is poor.[24-26] Erné et. al. first demonstrated the photogenerated charge collection efficiencies of n-GaP photoelectrodes could be increased in strong reverse bias through the use of a high-

*This chapter was adapted from a published work
Hagedorn, K.; Collins, S.; Maldonado, S.; J. Electrochem. Soc. 2010, 157, D558.

aspect-ratio electrode n-GaP form factor.[27] A more recent report by Maldonado and co-workers[28] illustrated that carefully prepared macroporous n-GaP photoelectrodes could in fact support simultaneously large photocurrents and large photovoltages, greatly increasing the potential of GaP for photoelectrochemical energy conversion and storage.

To date, high-aspect-ratio photoelectrode form factors have not been demonstrated with p-GaP photocathodes. Although electrochemical etching of n-GaP for the formation of macroporous films has been extensively detailed,[29-36] there are no prior reports on the preparation of macroporous p-GaP. The preparation of macroporous p-GaP(100) is demonstrated for the first time through a pulsed electrochemical etching procedure. The preparation and characterization of macroporous p-GaP(100) films are detailed herein, and the photoelectrochemical responses of as-prepared macroporous p-GaP(100) photoelectrodes for H_2 evolution in aqueous solutions are demonstrated.

II. Experimental.

Materials - All chemicals were used as received. Single-side polished, p-type GaP(100) wafers with a resistivity 0.41 Ω-cm (ITME) were diced into ~0.5 cm^2 sections, washed with water, methanol and acetone, and then dried under N_2(g) before use. Ohmic contacts to p-GaP were first made to each wafer section by lightly scratching the back face, briefly etching in conc. HF(aq) (48% v/v, Transene) to remove the native oxide, and soldering with In (Aldrich). The soldered In film was annealed at 400°C for 10 min in a 95:5 mixture of flowing H_2/N_2(g). Each annealed GaP section was then mounted onto a coiled, tinned copper wire and fixed with additional Ag epoxy (GC electronics) for mechanical support. The samples were then insulated with inert epoxy (1C Hysol, Loctite), exposing only the front polished wafer section plane. Electrode areas were determined through computer-captured optical images and image analysis software. Electrochemical etching was conducted under potentiostatic control in a variety of electrolytes (vide supra). Etching waveforms were generated with a NI USB-6008 multifunction voltage generator interfaced and controlled by custom-designed LabVIEW software. The output of the waveform generator was used to drive a separate potentiostat (Autolab 302A Eco Chemie) which could supply ±2A and ±30V. All etching was conducted in the absence of direct illumination.

Scanning Electron Micrographs - Scanning electron micrographs of the etched materials were performed using a Phillips XL30 FEG operated with a 15 kV beam voltage and a back-scatter detector. Steady-state photoelectrochemical responses were obtained with light from an ELH (Osram) lamp and a quartz cell filled with 1M H_2SO_4(aq) and recorded with a separate digital potentiostat (402A, CH Instruments). Wavelength-dependent measurements of external quantum yields were obtained with the same equipment and methodology as described previously.[28] A Pt mesh electrode and a Ag/AgCl electrode were used as the counter and reference electrodes, respectively. The bandwidth of illumination was controlled with bandpass bandfilters. The reported results represent the steady-state responses of the p-GaP(100) photoelectrodes after preparation and after correction for solution *iR* drop and concentration overpotential.[37]

Impedance Measurements - Impedance measurements were taken with a three-electrode cell consisting of an etched, planar p-GaP(100) working electrode, a Ag/AgCl reference electrode, and a Pt mesh counter electrode immersed in 1M H_2SO_4(aq). Immediately before use, p-GaP(100) working electrodes were etched as described previously, rinsed with water, and dried in a stream of N_2(g). H_2(g) was bubbled through solution for 30 min. prior to and during experiments. An Autolab 302A potentiostat equipped with a FRA was used to record the impedance characteristics of the cell. A series of sinusoidal excitation signals (± 10 mV) with frequencies ranging from 10 Hz to 100 kHz were used while the working electrode was held in reverse bias (-0.5 to -1.5 V vs. NHE) in the absence of illumination.

III. Results.

A. Electrochemical Etching - Electrochemical etching of p-GaP was conducted with a two terminal cell operated under potentiostatic control using a Pt counter electrode which was separated from the working electrode by about 1 cm. Several potential waveforms were explored to etch macropores in p-GaP(100). In aqueous acid electrolytes with an ionic strength of 1M, a large (>>2 V) positive bias applied continuously for 45 min resulted in bulk electropolishing of the p-GaP(100) interface. Specifically in either H_2SO_4(aq) or HNO_3, bulk etching by this waveform selectively left behind a p-GaP(100) interface covered with optically visible metallic Ga spots. In halide-containing acids

(HBr, HCl, and HI), the surface was roughened but with no residual Ga spots. At small (< 0.5 V) applied biases for both long and short times, no significant bulk etching or morphological change to the surface was apparent. A pulsed excitation waveform was also explored. Figure 1 shows the potential waveform that was determined empirically to favor etching that resulted in macropores. The p-GaP(100) electrodes were stepped to a large positive bias for 2.8 s and then stepped back down to a less positive bias for 90 s. The time duration for the large positive potential step was varied. In general, time spans less than 1 s did not yield macroporous films and time spans greater than 5 s caused the macroporous films to delaminate. Critical to the formation of macropores, the p-GaP(100) electrodes could not be left at open-circuit between the large positive potential pulses. Doing so resulted in bulk etching of the interface, albeit at a slower rate. Depending on the electrolyte, the necessary small positive bias between the brief large positive potential steps for macroporous etching was between 0.2 and 0.8 V. Etching at the threshold voltage would allow a film thickness of 40 microns, but thicker films were never obtained. Using etching voltages in excess of the threshold voltage seemed to result in films which were thinner than 40 microns, examples are shown in Figure 3b and Figure 5a.

Several observations were made regarding the two-electrode cell during the etching process. For example, the etching solvent gained a faint yellow hue and the threshold etching voltage was slightly reduced after many etching cycles in the 1M HBr. The identity of the yellow solute was never determined. It was also observed that the maximum peak current density oscillated by a few hundred mA cm^{-2} over many etching cycles, as shown in Figure 2, when the electrode was not etching. When an etching voltage was applied that caused the formation of macropores, the current density stopped oscillating. The origin of this process is unknown, but it was of some utility in preparing the macroporous layers because it gave an early indication of the macroporous film formation. This process was particularly useful for etching at the threshold voltage, as the yellow hue on the working electrode would not appear for 6-10 etching cycles. However, the peak current density indicated a macroporous etching after only 3 cycles.

Three different halide acids (HBr(aq), HCl(aq), and HI(aq)) were investigated as possible electrolytes for macroporous etching. To effect macroporous etching at the

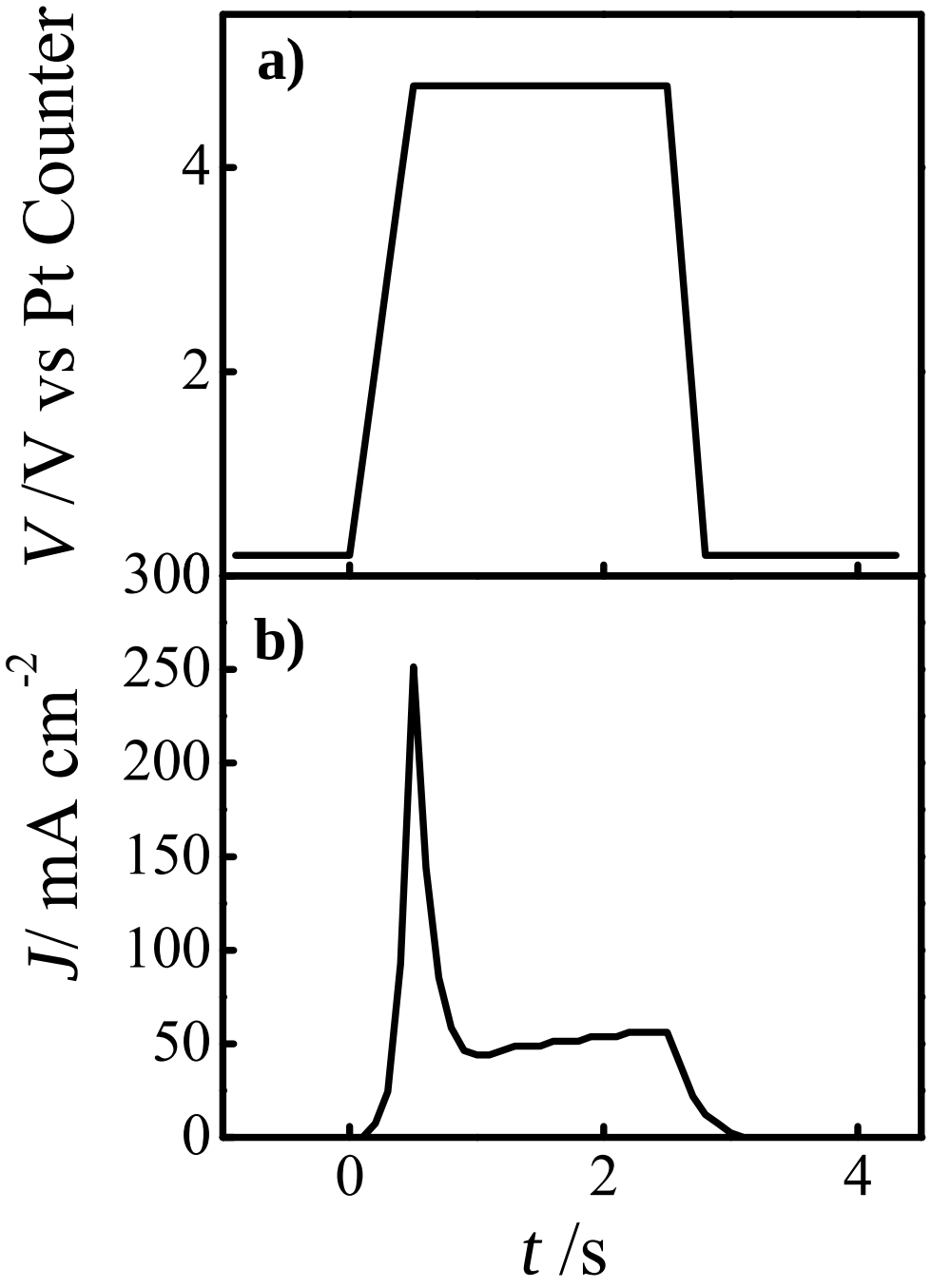

Figure 4.1. Pulsed voltage waveform (a) which favored the porous etching of p-GaP(100) and the accompanying current density (b) the resultant current-time profile recorded during etching.

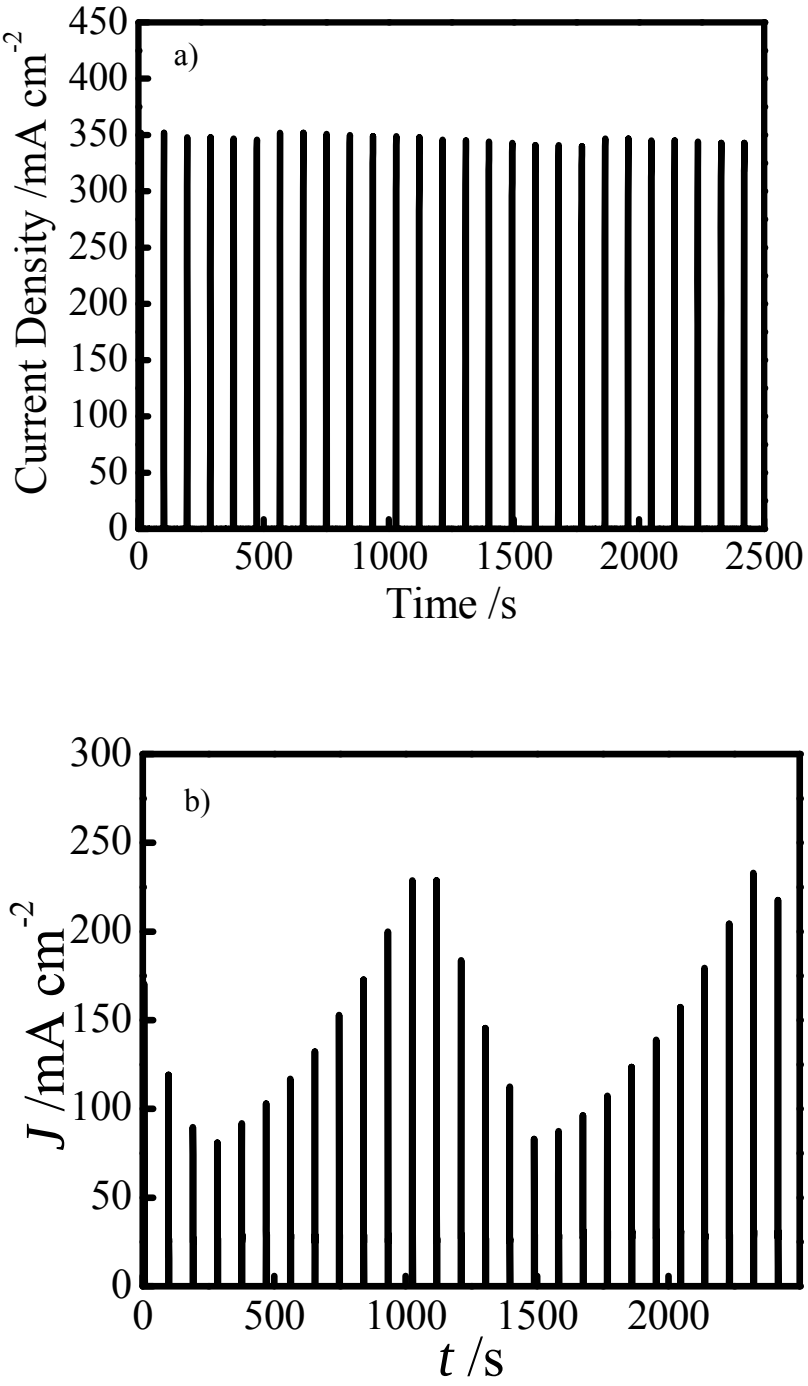

Figure 4.2. (a) The current-time profile which produced macroporous p-GaP(100). (b) The current-time profile which did not produce macroporous p-GaP(100).

same recorded current densities, considerably different values for the potential steps were necessary for each halide acid: 9 V (HCl), 4.85 V (HBr), and 3.8 V (HI). Figure 3 contrasts the morphology of p-GaP(100) electrodes after electrochemical etching under these conditions. In 1 M HI(aq), the p-GaP interface was unevenly roughened. It was also observed that during etching with HI, a dark yellow compound was formed at the interface. This solute turned the solution a deep yellow after a few etching cycles. In 1 M HCl(aq), the electrode possessed large, uneven, and deep pits. In contrast, in 1 M HBr(aq), thick, macroporous films were consistently prepared under these conditions on p-GaP(100) electrodes. In contrast to macroporous n-GaP, the pores formed with p-GaP(100) could neither be described as following a particular crystalline orientation[30,32] or as 'current line' pores.[31] The pores were not long or straight, and more closely resembled a disordered honeycomb structure. However, the pore size and wall thickness were uniform throughout the electrode film. Similar to macroporous n-GaP,[28] macroporous p-GaP appeared yellow to the eye.

A set of ionic strengths was explored for etching in HBr(aq) electrolytes. The epoxy used to insulate the back side of the p-GaP(100) sections was not stable in concentrated HBr(aq), so a range between 5 M and 0.1 M was explored. Figure 4 summarizes the results for etching in electrolytes with varied concentrations of HBr. In 5 M HBr(aq), the p-GaP(100) electrodes attained a yellow hue after 2-3 cycles in the etching process. However, macroporous GaP readily flaked off the surface and thick macroporous films could not be prepared. In 0.1 M HBr(aq), p-GaP could also be etched to form macroporous films, but the pore size was on average smaller than for films prepared in 1 M HBr(aq). In addition, these macroporous p-GaP films were less uniform.

Addition of ethylene glycol has previously been used to effect more uniform macroporous etching of single crystalline Si and iron oxide.[38-39] The influence of ethylene glycol on the electrochemical etching process of p-GaP(100) in 1 M HBr(aq) was investigated. An addition of 1.7M ethylene glycol in 1 M HBr(aq) caused a significant change to the observed macroporous film. The visible color of these macroporous p-GaP films was still yellow, but the hue was noticeably greener than for electrodes etched without ethylene glycol (Figure 5). Instead of improving the homogeneity of the macropores, the variation in the pore diameters increased. Lower

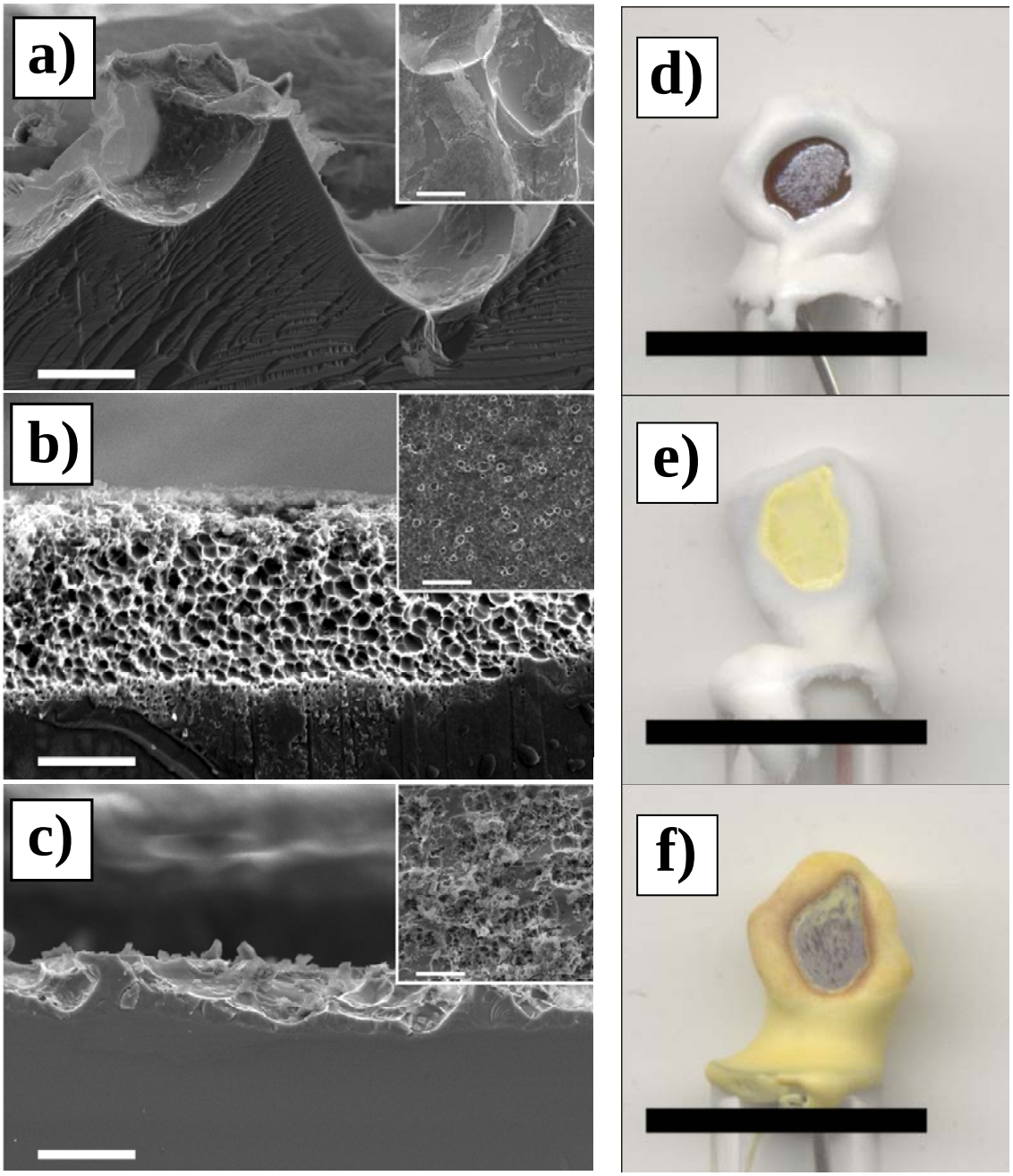

Figure 4.3. Cross-sectional scanning electron micrographs (left) and optical images (right) of macroporous p-GaP(100) electrochemically etched in (a,d) 1M HCl(aq), (b,e) 1M HBr(aq), and (c,f) 1M HI(aq). Insets in the electron micrographs show top-down view. Scale bars: 20 μm (left) and 1 cm (right).

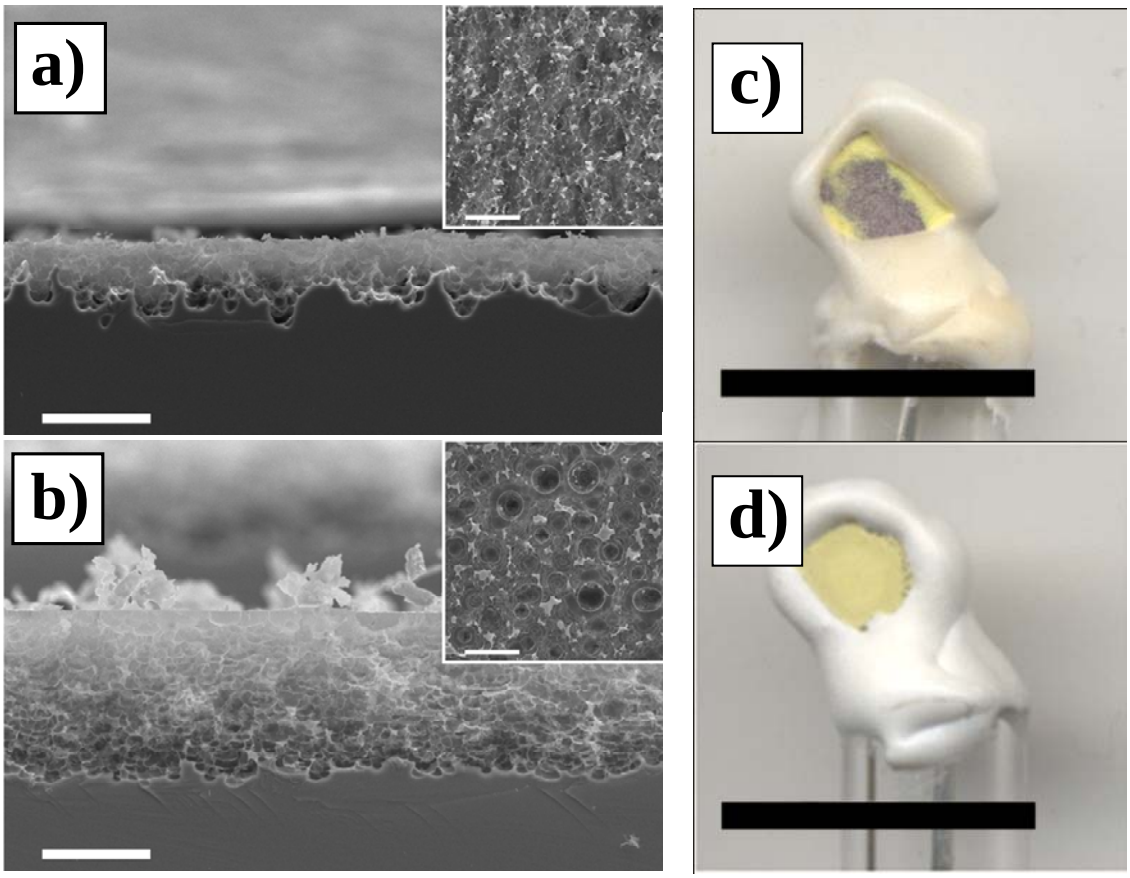

Figure 4.4. Cross-sectional scanning electron micrographs (left) and optical images (right) of macroporous p-GaP(100) electrochemically etched in (a,c) 5M HBr(aq) and (b,d) 0.1M HBr(aq). Insets in the electron micrographs show top-down view. Scale bars: 20 μm (left) and 1 cm (right).

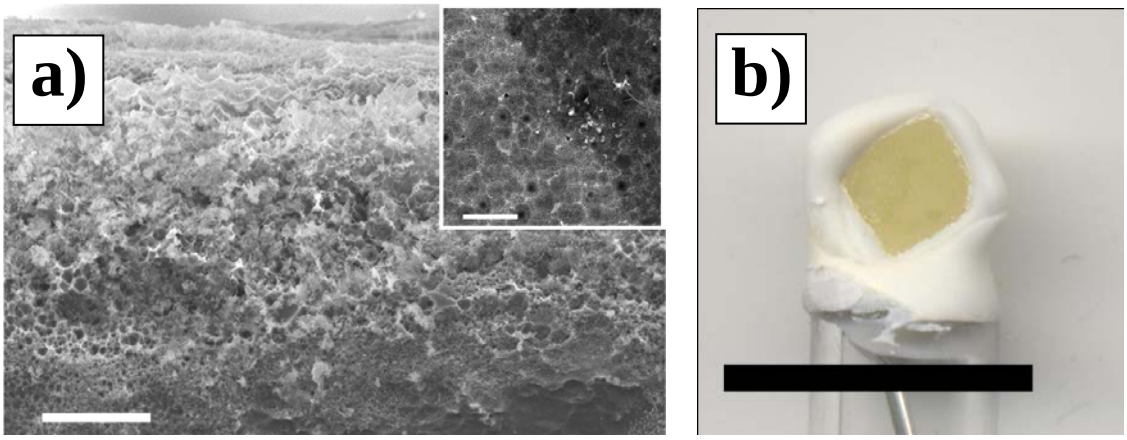

Figure 4.5. Scanning electron micrographs of cross-sections (a) and optical images (b) of macroporous p-GaP(100) prepared in a two-electrode cell using pulsed voltage anodic etching and a 1M HBr electrolyte with 10% ethylene glycol. Insets in the electron micrographs show top-down view. Scale bars: 20 μm (a) and 1 cm (b).

concentrations of ethylene glycol did not substantially influence the final macroporous film structure.

Changes in the magnitude of the anodic potential pulses in 1 M HBr(aq) were also studied. Figure 6 highlights the resultant films for electrochemical etching in 1 M HBr(aq) using more positive potential steps. At 6 V applied bias, the film morphology changed slightly. Macroporous films remained even throughout the face of the electrode, but the pores were larger with an average pore diameter of 6 ± 2 μm. At 8 V applied bias, the apparent pore diameters was 28 ± 4 μm. With 8 V potential pulses, the macroporous film quickly delaminated off the surface after 3 pulse repetitions and stable, thick films could not be obtained.

B. Photoelectrochemical Activity of Macroporous p-GaP(100) - The activities of planar p-GaP(100) and macroporous p-GaP(100) (prepared in 1 M HBr(aq) as in Figure 7b) photoelectrodes with the same bulk optoelectronic properties were analyzed in 1 M H_2SO_4(aq). Figure 7a shows the 100 mW cm^{-2} white-light responses of planar and macroporous p-GaP(100) for H^+ reduction to H_2. For planar p-GaP(100), the photoresponse characteristics in Figure 7a match those reported previously by Tamura et. al.[12] and Peat et. al.[25] for materials with short (< 100 nm) minority carrier diffusion lengths. The wavelength-dependent external quantum yields in Figure 7b for planar p-GaP(100) verified that the small photocurrents were attributable to the inefficient collection of visible light, $\lambda > 450$ nm efficiently. For comparison, the white-light photoresponse characteristic of macroporous p-GaP(100) photoelectrodes are also shown in Figure 7a. In contrast to previous reports for macroporous n-GaP(100), the p-GaP(100) macroporous photoelectrodes passed much lower photocurrent densities than the corresponding planar photoelectrodes by almost a factor 10. The wavelength-dependent external quantum yields in Figure 7b corroborated the data in Figure 7a, showing poorer external quantum yields for wavelengths $\leq$ 460 nm. However, for wavelengths > 450 nm, the macroporous p-GaP(100) photoelectrodes exhibited slightly larger external quantum yields than the corresponding planar photoelectrodes. A second set of white-light photoresponses were collected in 1 M H_2SO_4(aq) with a high-pass filter ($\lambda > 450$ nm). At these long wavelengths, the macroporous p-GaP(100) photoelectrodes exhibited higher photocurrent densities than the corresponding planar p-GaP(100)

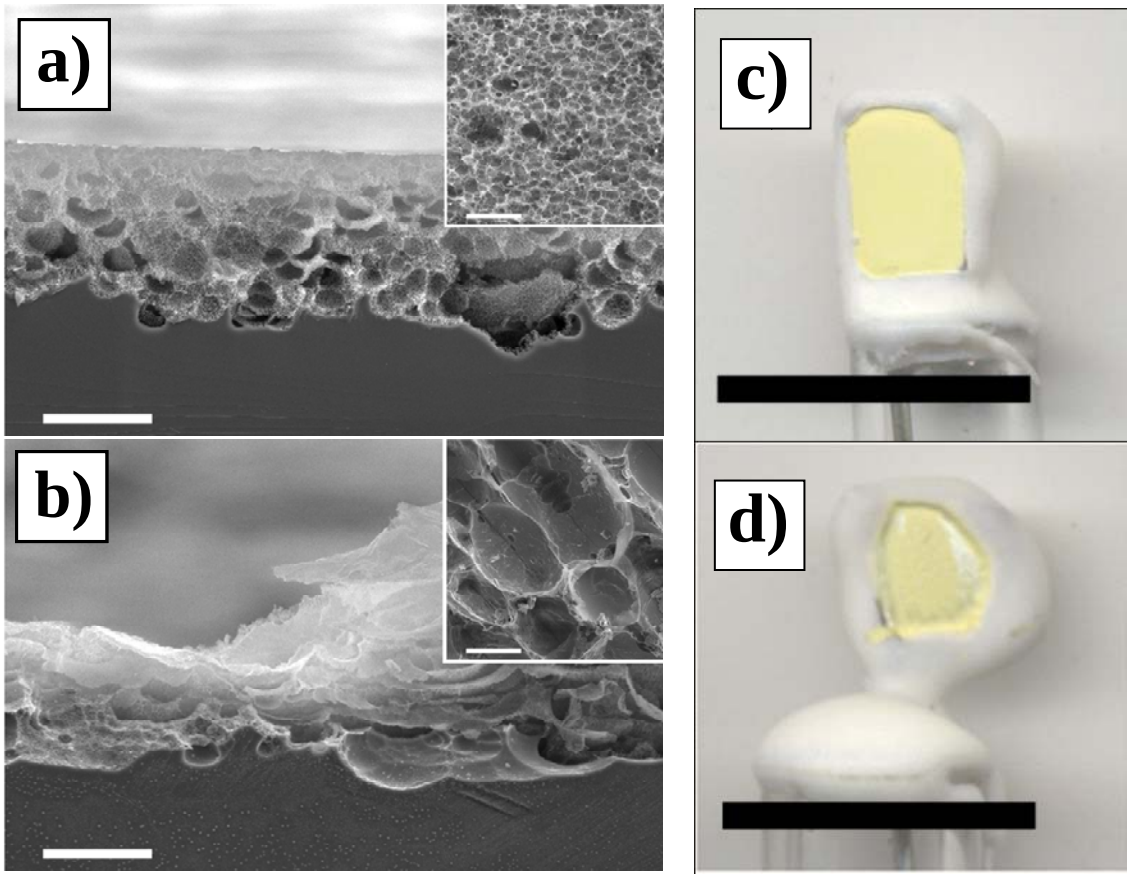

Figure 4.6. Cross-sectional scanning electron micrographs (left) and optical images (right) of macroporous p-GaP(100) electrochemically etched in 1M HBr(aq) with an applied pulse bias of (a,c) 6 V and (b,d) 8 V. Insets in the electron micrographs show top-down view. Scale bars: 20 μm (left) and 1 cm (right).

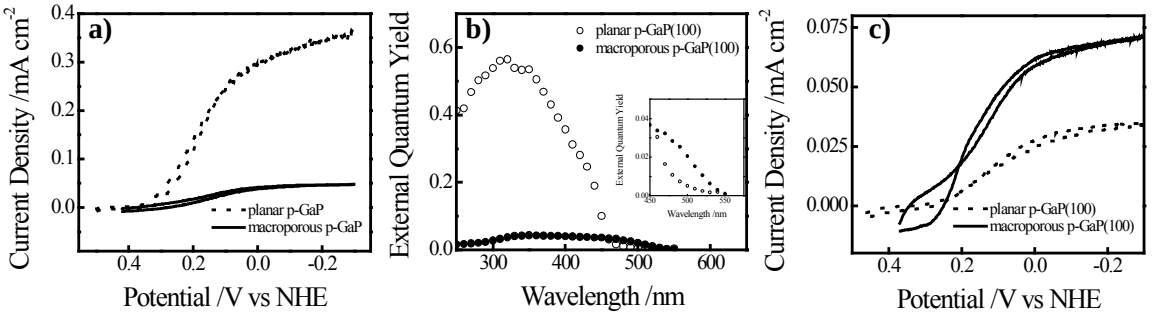

Figure 4.7. (a) Steady-state *J-E* responses for (dashed line) planar p-GaP(100) and (solid line) macroporous p-GaP(100) photocathodes immersed in 1 M H_2SO_4(aq) under 100 mw cm^{-2} white light illumination. (b) Wavelength-dependent external quantum yield data for (open symbols) planar p-GaP(100) and (dark symbols) macroporous p-GaP(100) photocathodes in 1 M H_2SO_4(aq) at E = 0 V vs NHE. (c) Steady-state *J-E* responses for (dashed line) planar p-GaP(100) and (solid line) macroporous p-GaP(100) photocathodes immersed in 1 M H_2SO_4(aq) under illumination with $\lambda > 450$ nm.

photoelectrodes. These responses were consistent over several samples and did not deteriorate with time. In both Figures 7a and 7c, the apparent open-circuit photovoltage, V_{oc}, did not substantially differ between the planar and macroporous photoelectrodes. This observation stands in contrast to a related, prior report on the comparison of the responses of planar and macroporous n-GaP photoelectrodes.[27-28]

C. Impedance Measurements - Figure 8 shows a plot of the reciprocal impedance-potential (C^{-2}-E) responses for this cell. Linear impedances responses consistent with a simple parallel *RC* circuit were only observed over a limited frequency range (47.1 - 1.91 kHz). The data in Figure 8 was used to calculate the built-in potential (and correspondingly the interfacial barrier height) according to Eq 1,[40]

$$C^{-2} = \frac{2}{qA^2\varepsilon_r\varepsilon_0 N_D}\left(\frac{k_B T}{q} - \left(\Phi_b + \frac{k_B T}{q}\ln\left(\frac{N_D}{N_{CB}}\right)\right) + E\right) \quad (1)$$

where C is the measured capacitance, q is the unit coulombic charge, A is the heterojunction area, ε and ε_0 are the static GaP dielectric constant (11.1) and the permittivity of free space, respectively, T is the temperature, k_B is Boltzmann's constant, N_D is the dopant density, N_{VB} is the effective density of states in the valence band, Φ_b is the equilibrium interfacial barrier height, and E is the potential applied to the working electrode.

IV. Discussion

A. Macroporous p-GaP(100) by Electrochemical Etching - The etching behaviors for macroporous p-GaP(100) film preparation strongly differ from the reported electrochemical etching behaviors of n-GaP(100) in aqueous acid electrolytes.[41-42] Although the specific morphology of n-type GaP produced by electrochemical etching is sensitive to changes in electrolyte, ionic strength, and applied potential,[33-35] the defining process in electrochemical etching of n-type semiconductors is the slow transport of holes (minority carriers) to the interface.[43] For p-GaP, holes are the majority carriers and the corresponding flux to the surface is accordingly much larger, limited only by thermionic emission of holes over the interfacial barrier height established between p-GaP(100) and

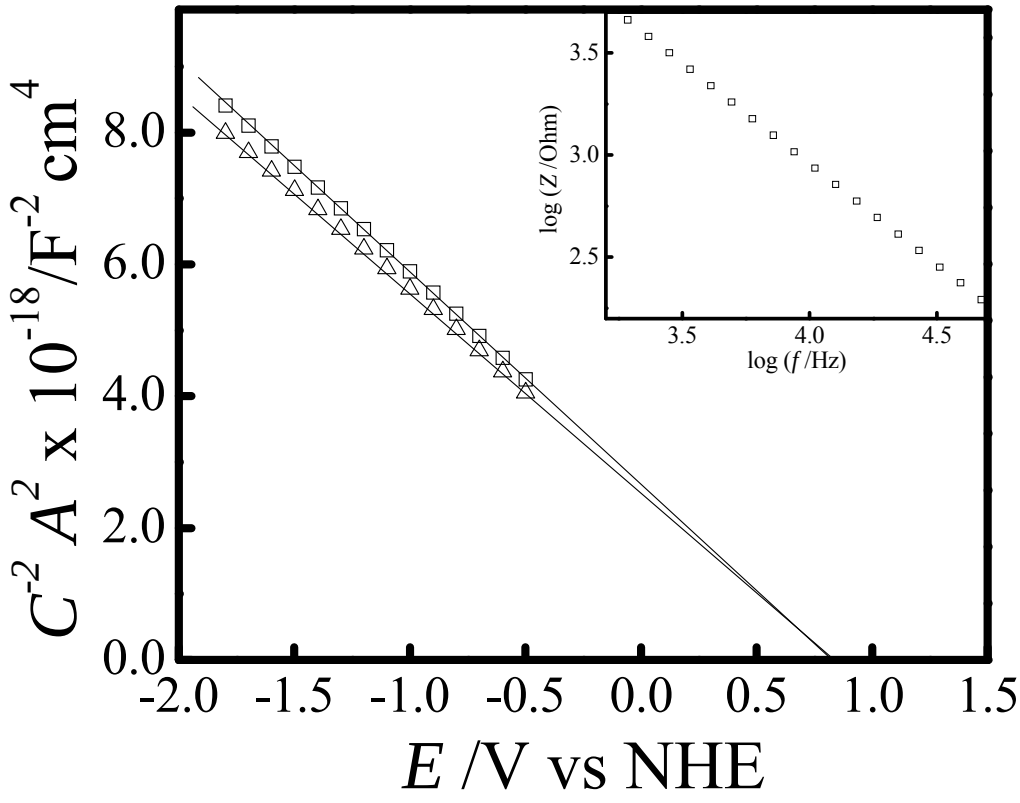

Figure 4.8. Impedance characteristics of p-GaP(100) electrode immersed in 1M H_2SO_4(aq) at 10.4 kHz (squares) and 1.9 kHz (circles). The inset shows the bode slope for this electrode at -1V vs NHE.

the liquid electrolyte. In strongly acidic solutions, this condition alone is apparently not sufficient to favor pore etching over plane etching of the entire surface. Macroporous etching was only effected in electrolytes that also contained dissolved anions that could be electrochemically oxidized.

Previous reports on the interaction of halide acids with crystalline GaP indicate that persistent adsorption of halide anions can occur at GaP surfaces.[22] In HCl(aq) and HBr(aq) electrolytes, bubbles were visible during the more positive potential steps, indicating that at least a portion of the anodic current at large positive biases was constituted by the oxidation of halide anions. The oxidized halide species apparently facilitates rapid chemical attack of the GaP(100) surface. The data suggest that a chemical etching mechanism also facilitated the formation of pores rather than bulk etching, if the chemical and electrochemical processes are properly balanced. For the conditions investigated here, 1 M HBr(aq) was the only electrolyte where the confluence of the chemical and electrochemical processes were best matched with regards to macroporous formation.

Macropores etched into p-GaP(100) in HBr(aq) could not be characterized as following either 'crystallographic orientation' or 'current-line orientation' etching, as is the case for crystalline n-GaP electrodes.[29,42-43] Rather, macropores for p-GaP(100) were more akin to randomly distributed 'compartments'. In this way, etched volumes did not propagate linearly from the surface into the bulk. Instead, the void space comprised a tortuous path from the surface to the interior bulk crystal. The data shown here do not rule out a particular permutation of etching conditions/substrate materials that could result in more ordered pores. In particular, the literature on macroporous p-Si films indicate that degenerately doped substrates tend to form straighter, more regular macropores as compared to non-degenerately doped substrates.[44] Degenerately doped p^+-GaP(100) substrates were not available to determine whether increased doping density similarly influences macroporous p-GaP(100).

The addition of an organic additive, ethylene glycol, that physisorbs on electrode surfaces[45-50] resulted in more finely sized macropores that approximated microporous structure. Although this work was not primarily directed at preparing microporous materials, the data in Figure 5 suggest microporous p-GaP(100) may be formed with

additional variation in additive concentration. In addition to blue-shifting the visible color of the porous layer (Supporting Information), microporous morphologies in semiconductors often effects a change in the photoluminescent properties.[51-52] Hence, although not the intended focus of this report, the use of an organic additive may facilitate the design and development of microporous p-GaP(100) luminescent materials. Separate measurements are underway to explore this avenue.

B. Macroporous p-GaP(100) as a Photocathode in Water - Several general conclusions can be reached from the results for the photoelectrochemical activity of macroporous p-GaP(100) prepared in 1 M HBr(aq). First, the enhanced activity of these films for solar-to-chemical storage with visible light was qualitatively in accord with past observations for macroporous n-GaP photoelectrodes. The data in Figures 7b and 7c are consistent with the premise that photons with long optical penetration depths can be more efficiently collected at interfaces with a high-aspect-ratio form factor. For visible light, the data in Figure 7c suggest that the macroporous p-GaP(100) photoelectrodes had a greater cumulative efficiency than the planar photoelectrodes by more than a factor of 2. However, the total collection yield of the macroporous p-GaP(100) photoelectrode for wavelengths up to 550 nm was still << 1, indicating these electrode form factors were not as efficiently designed as in previous reports of macroporous n-GaP(100).[27-28] In addition, the lack of difference in V_{oc} between the planar and macroporous photoelectrodes suggest that these systems are not ideally-behaving heterojunctions.[28] Poor electrocatalytic activity for H^+ reduction and deleterious surface traps at these GaP interfaces could contribute to this observation as well as the poor observed fill factors. Attempts to address these issues through deliberate chemical surface modification may improve certain features of the photoresponses. However, two morphological factors likely contribute to the small magnitudes for the internal quantum yields. The non-linear connectivity of these macroporous films is not favorable for mass-transport throughout the entire depth of the film. This aspect could lead to limited attainable current densities at all wavelengths, as seen in Figure 7b. The use of slow scan rates (<< 0.01 V s^{-1}) did not improve the steady-state photoresponses, indicating mass transport was not the sole limiting factor. The length scale of the macropore walls, in relation to the depletion width, was not optimized in these materials.[53] Since the dopant density is proportional to

the width of the near-surface depletion region within the semiconductor in a heterojunction,[54] the dopant density effectively defines the minimum length scale that a nanostructured photoelectrode must possess in order to support an electric field. The macroporous p-GaP(100) photoelectrodes used here possessed a wall thickness of 30±10 nm. From the bulk dopant density (N_D = 3.98 10^{17} cm^{-3}) and the measured barrier height at the p-GaP(100)/electrolyte interface at pH=1 (0.86±0.04 V, Supporting Information), the minimum wall thickness needed to support an internal electric field is≥ 100 nm. The uniformly low and flat external quantum yields in Figure 7b for the macroporous p-GaP(100) photoelectrode are thus fully consistent with the premise that these macroporous films featured wall thicknesses poorly matched with the bulk doping levels, effecting inefficient solar energy conversion.[53] Further work is necessary to determine appropriate etching/substrate combinations to yield p-GaP(100) photoelectrodes with better matched morphological features.

V. Summary.

A method for the preparation of macroporous p-GaP(100) by anodic etching has been presented. Pulsed anodic etching of p-GaP(100) in acidic electrolytes favored the formation of macroporous p-GaP(100). A range of etching conditions were explored, including acid type, electrolyte concentration, pulse potentials, and the addition of an organic additive. Each explored condition yielded p-GaP(100) surfaces with different textural features but only etching in 1 M HBr(aq) consistently produced stable macroporous films on p-GaP(100) These macroporous films demonstrated photoactivity as photocathodes for water-splitting applications. Although macroporous p-GaP(100) photocathodes did not show high external quantum yields across the visible and near-UV, these films did demonstrate an enhanced response at wavelengths longer than 450 nm as compared to planar p-GaP(100) photocathodes. This work is thus the first demonstration of both the preparation of macroporous p-GaP(100) and application of a high-aspect-ratio p-GaP(100) film as a photocathode with enhanced visible-light responses. The presented data indicate further refinement in electrochemical etching methods is needed to produce an optimized p-type macroporous GaP photoelectrodes for fuel-forming photoelectrochemical reactions.

VI. References.

1. Deutsch, T. G.; Head, J. L.; Turner, J. A. *J. Electrochem. Soc.* **2008**, *155*, B903.
2. Memming, R.; Schwandt, G. *Electrochim. Acta.* **1968**, *13*, 1299.
3. Li, J.; Peat, R.; Peter, L. *J. Electroanal. Chem. Interfacial Electrochem.* **1984**, *165*, 41.
4. Heller, A.; Aharon-Shalom, E.; Bonner, W. A.; Miller, B. *J. Am. Chem. Soc.* **1982**, *104*, 6942.
5. Khaselev, O.; Turner, J. A. *Science* **1998**, *280*, 425.
6. Szklarczyk, M.; Bockris, J. M. *J. Phys. Chem.* **1984**, *88*, 5241.
7. von Känel, H.; Gantert, L.; Hauger, R.; Wachter, P. *Int. J. Hydrogen Energ.* **1985**, *10*, 821.
8. Ingler, W.; Shaban, Y.; Khan, S. *ECS transactions* **2008**, *16*, 73.
9. Aspnes, D. E.; Heller, A. *J. Phys. Chem.* **1983**, *87*, 4919.
10. Bockris, J. M.; Uosaki, K. *J. Electrochem. Soc.* **1977**, *124*, 1349.
11. Goodman, C. E.; Wessels, B. W. *Appl. Phys. Lett.* **1986**, *49*, 829.
12. Yoneyama, H.; Sakamoto, H.; Tamura, H. *Electrochim. Acta.* **1975**, *20*, 341.
13. Harris, L. A.; Gerstner, M. E.; Wilson, R. H. *J. Electrochem. Soc.* **1977**, *124*, 1511.
14. Nakato, Y.; Ohnishi, T.; Tsubomura, H. *Chem. Lett.* **1975**, *4*, 883.
15. Tomkiewicz, M.; Woodall, J. *Science* **1977**, *196*, 990.
16. Wilson, R. H.; Harris, L. A.; Gerstner, M. E. *J. Electrochem. Soc.* **1977**, *124*, 1233.
17. Hedrick, J. B. *Rare earths: U.S. Geological Survey Minerals Year-book, Metals and Minerals*; U.S. Department of the Interior: Washington, D.C., 2001; Vol. v. 1. p. 61.1.
18. Shockley, W.; Queisser, H. J. *J. Appl. Phys.* **1961**, *32*, 510.
19. Kramer, D. *U.S. Geological Survey: Mineral Commodity Summaries*; U.S. Department of the Interior: Washington, D.C., 2006.
20. Gershenzon, M.; Mikulyak, R. M. *J. Appl. Phys.* **1961**, *32*, 1338.
21. Grimmeiss, H. G.; Rabenau, A.; Koelmans, H. J. *J. Appl. Phys.* **1961**, *32*, 2123.
22. Mukherjee, J.; Erickson, B.; Maldonado, S. *J. Electrochem. Soc.* **2010**, *157*, H487.
23. Richards, D.; Zemlyanov, D.; Ivanisevic, A. *Langmuir* **2010**, *26*, 8141.
24. Aspnes, D. E.; Studna, A. A. *Phys. Rev. B* **1983**, *27*, 985.
25. Peat, R.; Peter, L. M. *Appl. Phys. Lett.* **1987**, *51*, 328.
26. Gerischer, H. J. *J. Vac. Sci. Technol.* **1978**, *15*.
27. Erne, B. H.; Vanmaekelbergh, D.; Kelly, J. J. *J. Electrochem. Soc.* **1996**, *143*, 305.
28. Price, M. J.; Maldonado, S. *J. Phys. Chem. C* **2009**, *115*, 11988.
29. Foll, H.; Carstensen, J.; Langa, S.; Christophersen, M.; Tiginyanu, I. *Phys. Status Solidi A* **2003**, *197*, 61.
30. Langa, S.; Carstensen, J.; Christophersen, M.; Foll, H.; Tiginyanu, I. M. *Appl. Phys. Lett.* **2001**, *78*, 1074.
31. Langa, S.; Carstensen, J.; Tiginyanu, I. M.; Christophersen, M.; Foll, H. *Electrochem. Solid-State Lett.* **2001**, *4*, G50.
32. Ross, F. M.; Oskam, G.; Searson, P. C.; Macaulay, J. M.; Liddle, J. A. *Philos. Mag. A* **1997**, *75*, 525.
33. Rivas, J. G.; Lagendijk, A.; Tjerkstra, R. W.; Vanmaekelbergh, D.; Kelly, J. J. *Appl. Phys. Lett.* **2002**, *80*, 4498.
34. Tjerkstra, R. W. *Electrochem. Solid-State Lett.* **2006**, *9*, C81.

35. Tjerkstra, R. W.; Gomez Rivas, J.; Vanmaekelbergh, D.; Kelly, J. J. *Electrochem. Solid-State Lett.* **2002**, *5*, G32.
36. van Driel, A.; Bret, B. P. J.; vanmaekelbergh, D.; Kelly, J. J. *Surf. Sci.* **2003**, *529*, 197.
37. Bard, A. J.; Faulkner, L. R. *Electrochemical Methods: Fundamentals and Applications*; John Wiley & Sons: Hoboken, 2001.
38. Kilian, K. A.; Böcking, T.; Gaus, K.; Gal, M.; Gooding, J. J. *Biomaterials* **2007**, *28*, 3055.
39. Albu, S. P.; Ghicov, A.; Schmuki, P. *phys. status solidi-R* **2009**, *3*, 64.
40. Sze, S. M. N., Kwok K. *Physics of Semiconductor Devices*; 3 ed.; John Wiley & Sons: Hoboken, 2007.
41. Muller, K.; Wloka, J.; Schmuki, P. *J. Solid State Electrochem.* **2009**, *13*, 807.
42. Wloka, J.; Mueller, M.; Schmuki, P. *Electrochem. Solid-State Lett.* **2005**, *8*, B72.
43. Christophersen, M.; Langa, S.; Carstensen, J.; Tiginyanu, I. M.; Föll, H. *Phys. Status Solidi A* **2003**, *197*, 197.
44. Lehmann, V. *Electrochemistry of Silicon*; Wiley-VCH: Weinheim, 2002.
45. Buldini, P.; Zini, Q.; Ferri, D. *J. Electrochem. Soc.* **1981**, *128*, 1062.
46. Gole, J.; Dixon, D. *J. Phys. Chem. B* **1998**, *102*.
47. Huang, N.; Michel, R.; Voros, J.; Textor, M.; Hofer, R.; Rossi, A.; Elbert, D.; Hubbell, J.; Spencer, N. *Langmuir* **2001**, *17*, 489.
48. Kenausis, G. L.; Voeroes, J.; Elbert, D.; Huang, N.; Ningping, H.; Hofer, R.; Ruiz-Taylor, L.; Textor, M.; Hubbell, J.; Spencer, N. D. *J. Phys. Chem. B* **2000**, *104*, 3298.
49. Lee, S.; Mueller, M.; Ratoi-Salagean, M.; Voeroes, J.; Pasche, S.; De Paul, S.; Spikes, H. A.; Textor, M.; Spencer, N. D. *Tribol. Lett.* **2003**, *15*, 231.
50. Shimura, M.; Katsuma, M.; Chikuma, T.; Okumura, T. *J. Appl. Electrochem.* **1999**, *29*, 1177.
51. Schuurmans, F. J.; Megens, M.; Vanmaekelbergh, D.; Lagendijk, A. *Phys. Rev. Lett.* **1999**, *83*, 2183.
52. Schuurmans, F. J.; Vanmaekelbergh, D.; Van de Lagemaat, J.; Lagendijk, A. *Science* **1999**, *284*, 141.
53. Hagedorn, K.; Forgacs, C.; Collins, S.; Maldonado, S. *J. Phys. Chem.* C **2010**, 114, 12010.
54. Sze, S. M.; Ng, K. K. *Physics of Semiconductor Devices*; 3 ed.; John Wiley & Sons: Hoboken, 2007.

Chapter 5
Design Considerations for Nanowire Heterojunctions in Solar Energy Conversion/Storage Applications

I. Introduction.

A practical constraint in the design of scalable solar energy conversion/storage technologies is the use of low cost constituent materials. Efficient optical energy storage and conversion with traditional planar photoelectrode designs is only possible with semiconductors that support carrier collection lengths greater than the penetration depth of visible light, a property largely associated with high purity, expensive materials. Non-planar, high-aspect-ratio photoelectrode architectures eliminate the need for prohibitively expensive semiconductor materials.[1-2] High-aspect-ratio photoelectrode designs naturally decouple the directions of light absorption and photogenerated charge-carrier collection, circumventing severe minority carrier-based recombination losses even in materials with short carrier diffusion lengths.[3] However, meaningful energy conversion efficiencies with nanostructured photoelectrodes have thus far been difficult to consistently achieve in practice.[4] Factors such as heterogeneous charge-transfer kinetics, carrier recombination within the bulk material, and carrier recombination at surface trap sites are routinely identified as the main limiting factors that impact nanowire photoelectrode performance. Although the extent that these processes limit the operation of planar photoelectrodes has been extensively studied and documented,[5] the importance of these factors in nanostructured photoelectrodes, in relation to photoelectrode morphology and bulk electronic properties, has not yet been rigorously examined.

A common assumption in the design of nanowire photoelectrodes is that the value of the nanowire radius, *r*, only needs to not exceed the effective minority carrier diffusion

*This chapter was adapted from a published work
Hagedorn, K.; Forgacs, C.; Collins, S.; Maldonado, S. J. Phys. Chem. C 2010, 114, 12010.

length, L, of the bulk material to avoid bulk minority carrier recombination losses. For a material like iron oxide (α-Fe_2O_3), this notion defines the 'optimal' nanowire radius at ~10^{-8} m.[6] Nanowires with radii at this length scale have been exhaustively explored and the photoelectrode activity of these nanowires have been tested.[7-9] In all cases, the internal quantum efficiency of these nanostructured photoelectrodes has been much less than 1, raising doubt as to whether 'r equal to or less than L' is the most relevant design criterion.

The width of the internal depletion region, W, within the semiconductor should be an influential criterion for high-aspect-ratio heterojunctions. For an n-type semiconductor in depletion,[10] the width, W, of the space charge layer within the near-surface region of the semiconductor is a function of the dielectric constant and doping density of the semiconductor material,[11]

$$W = \sqrt{\frac{2\varepsilon\varepsilon_0\left(\Phi_b + \frac{k_B T}{q}\ln\left(\frac{N_D}{N_{CB}}\right)\right)}{qN_D}} \qquad (1)$$

where ε is the effective dielectric constant of the semiconductor, ε_0 is the permittivity of free space, Φ_b is the equilibrium junction barrier height, k_B is Boltzmann's constant, T is the system temperature, q is the unsigned charge of an electron, N_D is the dopant density, and N_{CB} is the effective density of states of the conduction band. Although recent reports on the activity of high-aspect-ratio photoelectrodes suggest a sensitivity to the doping level,[12-13] to date there have been no quantitative investigations that detail precisely how the ratio of r/W impacts the carrier collection efficiency of nanowire photoelectrodes when all other relevant photoelectrode parameters are defined.

Herein, we present a complementary set of experimental and digital simulation results for Si nanowire arrays as photoelectrodes in regenerative photoelectrochemical cells that directly probes how the ratio r/W influences photoelectrode efficiency in the presence of varied levels of bulk and surface recombination. We show the observable photocurrent-potential (J-E) responses for two extreme Si nanowire doping

concentrations for the cases of $r/W \sim 1$ and $r/W << 1$. The studied r/W ratios correspond to non-degenerate doping levels in the studied Si nanowires, affording analyses of their photoresponses without the confounding issues associated with degenerately doped photoelectrodes.[14-16] We discuss the implications of the presented data and suggest guidelines for where emphases should be placed for continued development of nanostructured photoelectrodes.

II. Experimental.

Materials - Single-crystalline n-type Si(111) wafers with resistivities of 0.02 Ω-cm (Czochralski growth, ITME), 1.1 Ω-cm (Czochralski growth, ITME), and >3000 Ω-cm (float zone growth, MEMS) were used. Wafer resistivities were determined from 4 point probe measurements using a Lucas lab probe head (S-302-6) and stand (SP4-40085TFY) connected to a Schlumberger 1286 potentiostat. Prior to use, wafers were degreased with sequential immersions in water (>18 MΩ-cm, Barnstead), methanol (Fisher), acetone (Fisher), methanol, and water. Wafer sections were then dried under N_2(g), and soaked in a 3:1 v/v mixture of H_2SO_4 (Aldrich) and 30% H_2O_2 (Fisher) at 90 °C for 45 min. Sections were then rinsed with water and either dried under N_2(g) and stored or used immediately.

Metal Assisted Etching of Nanowire Arrays - Si nanowires were prepared by metal assisted chemical etching.[17-18] Freshly cleaned Si was first etched in a solution of 5% HF(aq) for 3 min and then immersed in a solution of 4.8M HF(aq) containing 0.005 M $AgNO_3$(Aldrich) for 60 s. Si sections were visibly tinted metallic yellow, indicating uniform electroless deposition of silver (Ag). These surfaces were carefully rinsed with water to remove excess salt and then placed in a light-tight, black plastic vial containing an etching solution that was 4.8M HF(aq) and 0.10-0.35 M H_2O_2(aq) for 45 minutes. Following etching and a copious water rinse, sample surfaces were dull black. Samples were subsequently immersed in Ag-etchant solution (Transene) for 15 seconds to remove excess particulate Ag. The higher dopant density silicon substrate required a lower hydrogen peroxide concentration to obtain 15 micron nanowires. Hydrogen peroxide degrades slowly, even when stabilized. The age of the bottle needed to be accounted for when determining what concentration was appropriate for etching. The relation between

the hydrogen peroxide concentration and etching rate was determined empirically using SEM image analysis and would periodically need to be reevaluated as the hydrogen peroxide reagent aged. After several days, a hydrogen peroxide concentration which was 2-5% higher was required.

Physical Characterization - Scanning electron microscopic analysis of these materials was conducted with a Philips XL30-FEG instrument operated at 15 kV with a secondary electron detector. Nanowire diameters were assessed directly from high-magnification electron micrographs.

Photoelectrode Preparation - Ohmic contact was made by lightly scratching the backside of each Si section, etching with conc. HF(aq), and then applying In-Ga eutectic. The sections were then mounted onto a coiled tinned copper wire, fixed with conductive Ag epoxy (GC Electronics), and sealed with 1C Hysol epoxy (Loctite). Electrode areas were nominally 0.1 cm^2, as determined through optical image analysis.

Photoelectrochemical Measurements - A quartz cell with an optically flat bottom serving as the window was used for photoelectrochemical measurements and was assembled in an inert atmosphere glovebox. Dry methanolic solutions containing previously sublimed 1,1-dimethylferrocene (dmFc, Aldrich) were prepared with lithium perchlorate (battery grade, Aldrich). 1,1-dimethylferrocenium ($dmFc^+$) was generated in-situ via bulk electrolysis. In contact with n-Si, this redox couple renders a nominal value of $q\Phi_b$ equal to 1eV.[19] Platinum (Pt) gauze was used as the counter electrode and a luggin capillary reference electrode containing a platinum wire poised at the solution potential served as the reference. After assembly, the cell was removed from the glovebox, connected to a Schlenk line, and kept under a positive pressure of Ar(g) (Metro Welding). Concentration overpotentials and uncompensated solution resistances were estimated using a Pt working electrode. Voltammetric measurements were performed using a CH instruments 402A potentiostat. Illumination of the electrode was achieved with an Osram ELH 300 W lamp and a 1 cm water filter. Illumination intensities were calibrated using a Thorlabs S302A optical power meter. Immediately before use, all electrodes were first etched with HF(aq), washed with methanol, and dried in a stream of N_2(g). The presented photocurrent density (*J*)-potential (*E*) data are corrected for solution *IR* drop and concentration overpotential[20] and represent the average responses for three separate

photoelectrodes for each investigated type. The optical transparency of methanol containing 1 M $LiClO_4$, 195 mM dimethylferrocene, and 5 mM dimethylferrocenium was measured using a Varian Carey 5000 UV-Vis spectrometer. A UV-Vis spectrum was obtained using a 1-cm pathlength quartz cuvette filled with this electrolyte. For photoelectrode measurements, a 2 mm solution pathlength was used. The solution concentration was decreased by a factor of 5 to adjust the measured transmittance data to match the photoelectrochemical experimental conditions according to Eq 2,

$$-\log\left(\frac{P_{meas}}{P_0}\right) = abc \tag{2}$$

where *a* is the material absorptivity, *b* is the pathlength, and *c* is the solution concentration.

Time-Resolved Microwave Photoconductivity - Si wafer sections were sandwiched between two glass coverslips wetted by a methanolic 5 mM/195 mM $dmFc^{+/0}$ solution. The samples were then inserted into a custom-built microwave photoconductivity system. A Continuum Minilite Nd:YAG laser operating at λ = 1064 nm was used to produce excitation pulses with a full-width at half-maximum of < 10 ns. The microwave source was a HP 8350B Sweep Oscillator with a 83570A module operating at a frequency of 24 GHz and a nominal output power of 5 mW. The reflected signal was measured with an Advanced Control Devices diode (ACSP2644NZ, rise time < 1 ns) connected to a Tektronix TDS 1002B digital oscilloscope. The decays were fit with a single exponential function to determine the effective time constant.

Optical Measurements - Wavelength-dependent external quantum efficiency measurements were recorded using a spectral response system described previously.[2] The methanolic $dmFc^{+/0}$ solution was diluted to approximately 1% of its original concentration. These concentrations still supported as much as 300 uA cm^{-2} of photocurrent. Monochromatic illumination intensities were kept under 100 $\mu W\ cm^{-2}$. Specular reflectance measurements were obtained using the same system in conjunction with either a specular reflectance accessory (Varian accessory for Carey 5000) or an

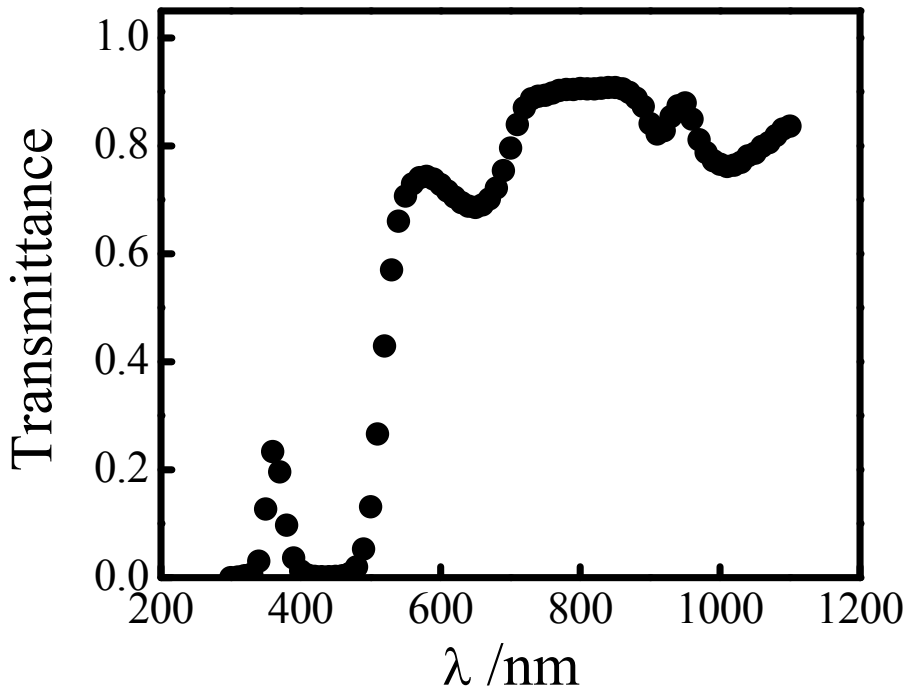

Figure 5.1. Approximate solution transmittance for a 2 mm beam pathlength through a methanolic electrolyte containing 195 mM dimethylferrocene and 5 mM dimethylferrocenium.

integrating sphere (819D-SF-4, Newport). Diffuse reflectance spectra were referenced against a thick Spectraflect® film.

Photoelectrode Response Simulations - A two dimensional, finite difference software package (TeSCA, Karl-Weierstrass-Institute) was used to simulate the steady-state photocurrent-potential responses of planar and cylindrical photoelectrodes. This software package solves Poisson's equation subject to Fick's law of diffusion to approximate diffusion, drift, recombination, and generation in semiconductor devices. A thorough description of the software applied to planar semiconductor interfaces has been reported previously.[21-22] For three-dimensional cylindrical photoelectrodes, a radial coordinate system was employed to effectively model a three-dimensional object using two spatial coordinates. The variables describing the bulk optoelectronic properties of the semiconductor, the electrolyte, and the associated charge-transfer kinetics are tabulated in Table 1. In all cases, the semiconductor/liquid contact was approximated as a conformal dielectric with a dielectric constant of 6. The back contact was modeled as a perfect ohmic contact with $S = \infty$. A Beer -Lambert optical excitation profile was used to simulate the steady-state photogeneration of carriers. Each simulation was run assuming monochromatic radiation with a characteristic value of α and an illumination angle of°0 with respect to the surface normal. The wavelengths corresponding to the values of α used for each simulation were determined from published optical data for Si.[23] The TeSCA simulations would occasionally produce *J-V* responses indicating internal quantum yields much above 1 or 0, inconsistent with slight changes in simulation parameters. These trials were identified as inaccurate. When the value of the dopant density was varied by as little as .1% TeSCA yielded new results in accord with prediction.

Modeling of Recombination Processes - A trap model[24-25] was used in TeSCA to define the non-radiative bulk and surface recombination rates for the modeled semiconductor photoelectrode. For this recombination model, each trap state has an independent capture rate for electrons and holes that is defined as the product of the thermal velocity (v_i, cm s^{-1}) and the capture cross (σ_i, cm^2) for each respective charge carrier,

$$k_n = \nu_n \sigma_n \tag{3a}$$

Table 5.1. TeSCA simulation parameters

Parameter	Description	Value	Units
$q\Phi_b$	barrier height	1.0	eV
$\mathbf{E}_g$	bandgap	1.12	eV
n_i	intrinsic carrier concentration	1.45×10^{10}	cm^{-3}
ε_{Si}	Si dielectric constant	11.9	
$\varepsilon_{electrolyte}$	electrolyte dielectric constant	6	
T	temperature	300	K
N_{CB}	effective density of states in conduction band	2.8×10^{19}	cm^{-3}
N_{VB}	effective density of states in valence band	1.04×10^{19}	cm^{-3}
N_D	dopant density	10^{13} - 10^{18}	cm^{-3}
k_n	bulk trap capture coefficient for electrons	1×10^{-8}	$cm^3\ s^{-1}$
k_p	bulk trap capture coefficient for holes	1×10^{-8}	$cm^3\ s^{-1}$
$k_{n,s}$	surface trap capture coefficient for electrons	1×10^{-8}	$cm^3\ s^{-1}$
$k_{p,s}$	surface trap capture coefficient for holes	1×10^{-8}	$cm^3\ s^{-1}$
$k_{Aug,n}$	Auger recombination coefficient for electrons	2×10^{-31}	$cm^6\ s^{-1}$
$k_{Aug,p}$	Auger recombination coefficient for holes	2×10^{-31}	$cm^6\ s^{-1}$
N_t	bulk trap density	1×10^{13}- 5×10^{13}	cm^{-3}
$N_{t,s}$	surface trap density	10^8-10^9	cm^{-2}
$\mathbf{E}_s$	energy of surface traps	$\mathbf{E}_g/2$	eV
h	nanowire height	15-100	um
r	nanowire radius	25-500	nm
μ_n	electron mobility	1300	$cm^2\ V^{-1}\ s^{-1}$
μ_p	hole mobility	450	$cm^2\ V^{-1}\ s^{-1}$
k_{et}	heterogeneous electron transfer rate constant	10^{-19}	$cm^4\ s^{-1}$
k_{ht}	heterogeneous hole transfer rate constant	10^{-19}	$cm^4\ s^{-1}$
I_0	flux of photogenerated carriers	0.02	$C\ cm^{-2}\ s^{-1}$
α	absorptivity	2.70 - 6390	cm^{-1}
[dmFc]	concentration of reduced redox couple	0.0001	$mol\ cm^{-3}$
[$dmFc^+$]	concentration of oxidized redox couple	0.0001	$mol\ cm^{-3}$
λ_{re}	reorganization energy	0.5	eV

$$k_p = \nu_p \sigma_p \tag{3b}$$

where k_n and k_p are the respective capture coefficients for electrons and holes at trap states in the bulk. Corresponding capture coefficients were calculated for electrons and holes at trap states at the electrode interface, respectively.

$$k_{n,s} = \nu_n \sigma_{n,s} \tag{4a}$$

$$k_{p,s} = \nu_p \sigma_{p,s} \tag{4b}$$

Although this model could accommodate differences in capture processes for electrons and holes at traps, the results presented here assumed $\nu = \nu_n = \nu_p = 10^7$ cm s^{-1} and $\sigma = \sigma_n = \sigma_p = 10^{-15}$ cm^2, in accord with experimentally observed values for crystalline Si.[10,26] The energy of the traps was set to be exactly in the middle of the bandgap. Explicit values for surface recombination rates, S, were then determined using Eq 11. Explicit values for the minority carrier diffusion length were bound according to Eq 5,

$$L_p = \sqrt{D_p \tau_p} = \sqrt{\frac{k_B T \mu_p}{q N_t k_p}} \tag{5}$$

where D_p is the diffusion coefficient of minority carriers (holes), τ_p is the lifetime of minority carriers, N_t is the bulk trap concentration, and the rest of the terms have their same meanings. To change the value of L_p for a given simulation, only the parameter N_t was adjusted. Auger recombination was also incorporated into the simulations,[27] using recombination coefficients of 2 x 10^{-31} cm^6 s^{-1} for both electrons and holes.[27]

Modeling of Heterogeneous Charge Transfer - A Marcus-Gerischer formalism is used by TeSCA to model heterogeneous charge transfer at semiconductor/electrolyte interfaces,[28]

$$j_n = j_{0,n}\left(\frac{n_s}{n_{0s}} - 1\right) = -q k_{et} N_{CB} [dmFc^+] e^{\frac{-(q\Phi_b - \lambda_{re})^2}{4 k_B T \lambda_{re}}} \left(\frac{n_s}{n_{0s}} - 1\right) \tag{6a}$$

$$j_p = j_{0,p}\left(\frac{p_s}{p_{0s}} - 1\right) = -qk_{ht}N_{VB}[dmFc]e^{\frac{-(E_g - q\Phi_b - \lambda_{re})^2}{4k_BT\lambda_{re}}}\left(\frac{p_s}{p_{0s}} - 1\right) \quad (6b)$$

where k_{et} is the heterogeneous rate of electron transfer from the conduction band edge at optimal exoergicity, k_{ht} is the heterogeneous rate of hole transfer from the valence band edge at optimal exoergicity, [$dmFc$] is the concentration of dimethylferrocene, [$dmFc^+$] is the concentration of dimethylferrocenium, λ_{re} is the reorganization energy for the dmFc/dmFc$^+$ redox couple, n_s is the surface concentration of electrons, n_{0s} is the surface concentration of electrons in the dark at equilibrium, p_s is the surface concentration of holes, and p_{0s} is the surface concentration of holes in the dark at equilibrium. A value of 0.5 eV was used for λ_{re} based on the reorganization energies for fast outer-sphere redox couples.[20] Precise measurements of k_{et} and k_{ht} for Si in this system are not feasible since n-type and p-type Si electrodes are in strong inversion and accumulation conditions, respectively, when in contact with this electrolyte. Estimates for the magnitude of these standard rate constants were instead based on the following relations,

$$k^o_{sc,et} = k_{et}N_{CB} \quad (7a)$$

$$k^o_{sc,ht} = k_{ht}N_{VB} \quad (7b)$$

$$k^o_{sc,et} \leq k^o_m \quad (8a)$$

$$k^o_{sc,ht} \leq k^o_m \quad (8b)$$

where k^o_{sc} is the heterogeneous charge-transfer standard rate constant at a semiconductor electrode[29] and k^o_m is the standard rate constant for heterogeneous charge-transfer of the same redox couple at a metal electrode. Recent experimental measurements of k^o_m for related ferrocene/ferrocenium redox couples in both aqueous and acetonitrile solutions using Au and Pt ultra-microelectrodes yielded values ranging between of 6.8 to 8.4 cm s^{-1}.[30-31] These measurements imply values no greater than 2.9 x 10^{-19} and 7.7 x 10^{-19} cm^4 s^{-1} for k_{et} and k_{ht} at Si electrodes, respectively. A conservative estimate of 1 x 10^{-19} cm^4 s^{-1} was used for both k_{et} and k_{ht} for the presented simulations. Although TeSCA also has the

capacity to include heterogeneous charge-transfer from surface states to acceptors/donors in solution, the rates for these processes were set to zero for the presented simulations.

Determination of the Minority Carrier Diffusion Length - Measurements of the external quantum yields for planar Si photoelectrodes in methanolic electrolyte containing dimethylferrocene/dimethylferrocenium were obtained at several wavelengths. Using the so-called Gärtner relation, these data were used to estimate L_p,[37]

$$\text{External Quantum Yield} = \text{Internal Quantum Yield} \times (1-R) = \left(1 - \frac{e^{-\alpha(\lambda)W}}{1+\alpha(\lambda)L_p}\right) \times (1-R) \quad (9)$$

where R is the reflectance of the Si/electrolyte interface, $\alpha(\lambda)$ is the wavelength-dependent absorptivity of Si, and the rest of the terms have their same meanings as described in the main text. For wavelengths where $\alpha(\lambda)$ is much smaller relative to W, Eq 9 can be re-written as

$$\frac{1}{\text{Internal Quantum Yield}} = 1 + \frac{1}{\alpha(\lambda)} \times \frac{1}{L_p} \quad (10)$$

Reflectivity of the Si Nanowire Film - The total (specular + diffuse) reflectance at a Si nanowire film in contact with methanol was determined using the system described in the optical measurements section. These data were used to adjust the internal quantum efficiency values determined from numerical simulation with TeSCA to compare directly with the measured external quantum efficiency values.

III. Results.

A. Si Nanowire Morphology - Metal-assisted chemical etching[17-18] of crystalline planar Si substrates resulted in matte dull, black films comprised of finely spaced, vertically oriented Si nanowires. Figures 4a and 4b highlight the relevant morphological features of the Si nanowire films used in this study. Nanowire films with total lengths of ca. 15 μm were consistently obtained with the etching conditions described above. Longer nanowire lengths were difficult to reproduce, particularly with the more lightly doped Si

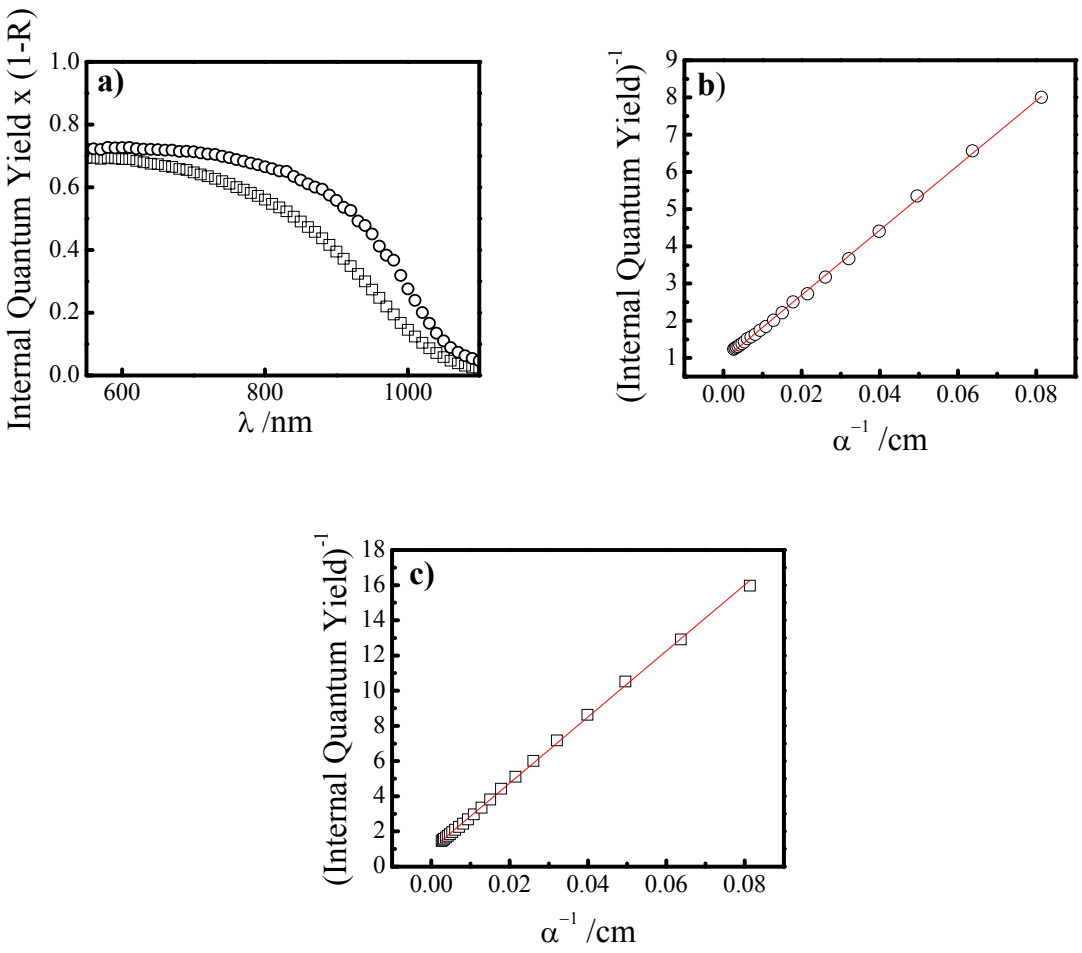

Figure 5.2. (a) Short-circuit external quantum yield (i.e. not corrected for reflectance losses) as a function of wavelength for the (open squares) heavily doped and (open circles) lightly doped planar Si photoelectrodes. These data are reproduced from Figure 7. (b) Reciprocal short-circuit internal quantum yield values as a function of the wavelength-dependent optical penetration depth for the more lightly doped n-Si planar photoelectrodes. (c) Same as in (b) except these data are for the more heavily doped n-Si planar photoelectrodes. The data in (b) and (c) were first corrected for '1-*R*' losses using the known reflectivity of polished Si and the index of refraction of methanol.[23]

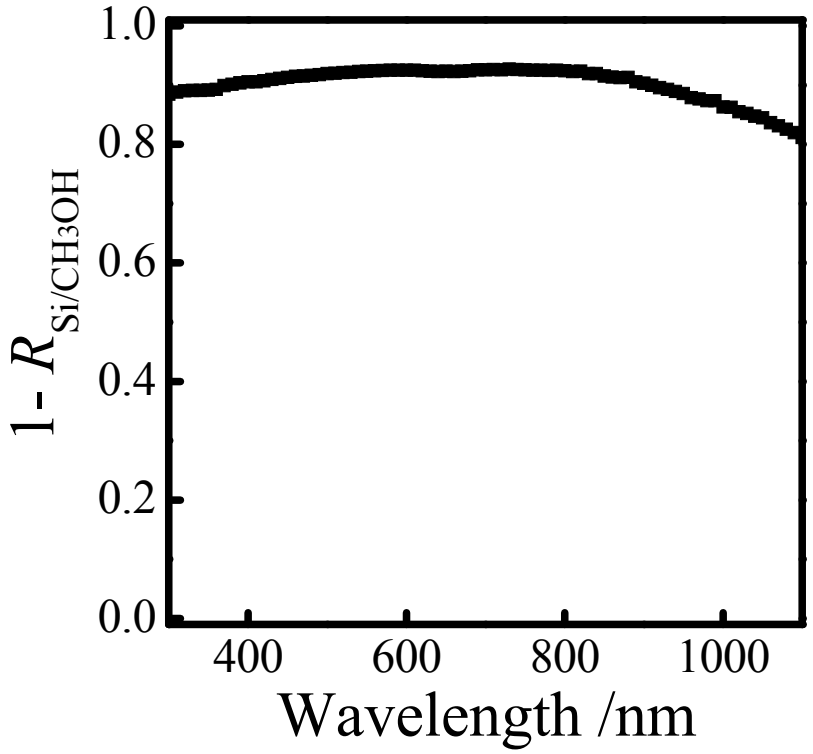

Figure 5.3. Total reflectance losses at the n-Si nanowire/CH_3OH interface. The data represent the maximum values for the external quantum yield values measured at each wavelength.

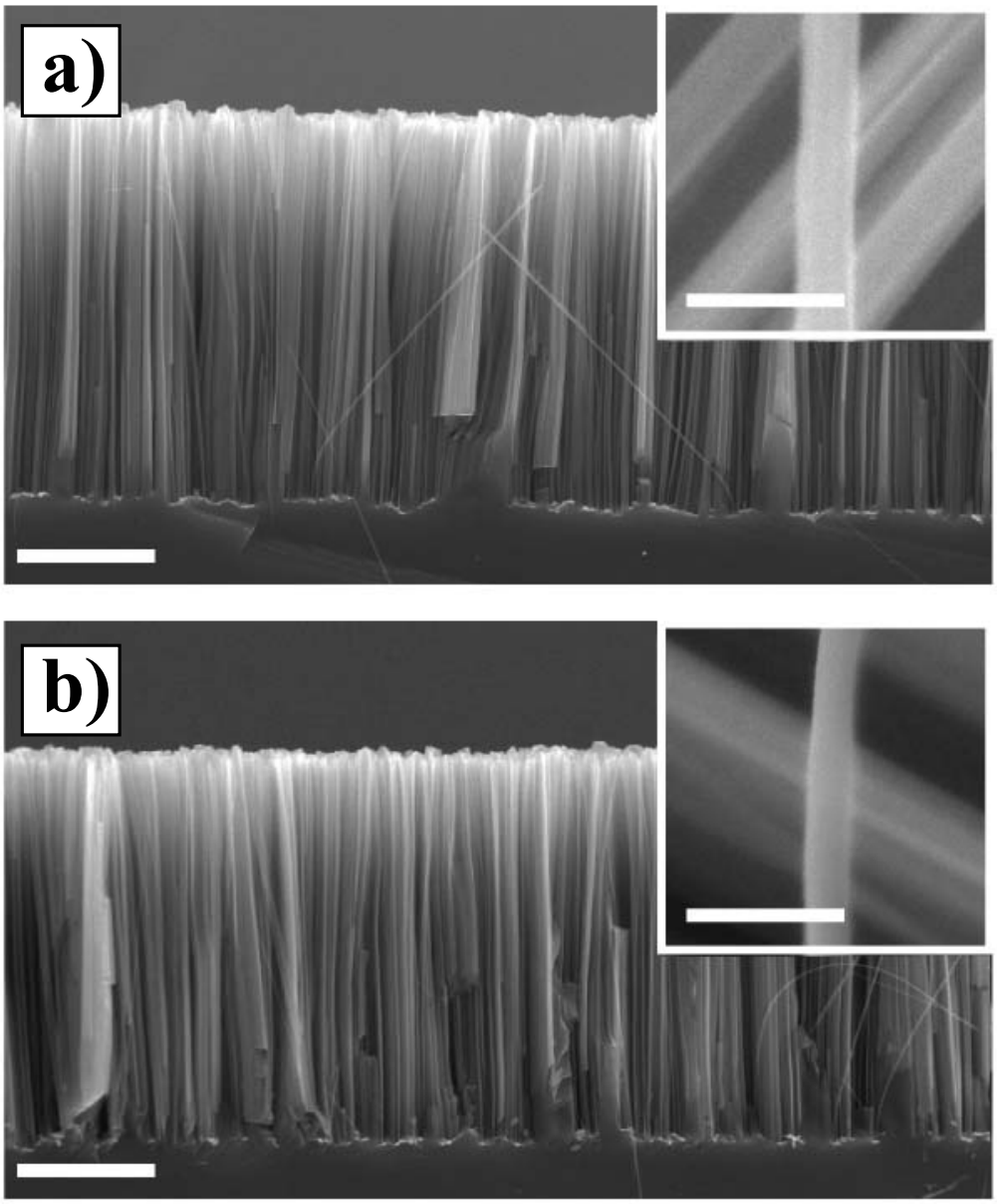

Figure 5.4. Scanning electron micrographs of cross-sections of Si nanowire films prepared by metal-assisted etching. (a) Si nanowires prepared using a Si(111) substrate with N_D = 7.8 x 10^{17} cm^{-3} (b) Si nanowires prepared using a Si(111) substrate with N_D = 4.8 x 10^{15} cm^{-3}. Scale bar: 5 μm. Inset scale bar: 200 nm

substrates. Under the employed conditions, Si nanowire radii generally ranged between 25 and 50 nm for all studied electrodes. Large area (> 1 cm^2) films were also challenging to prepare without large patches devoid of nanowires. Electrode dimensions were chosen in this study (~0.1 cm^2) to minimize biasing effects from such film imperfections. Assuming a uniform packing density of these Si nanowire arrays where the edge-to-edge distance between each nanowire is equal to the nanowire diameter, the ratio of the true surface area of these Si nanowire films to the projected (top-down view) area was approximately 190.

B. Surface Recombination at Si Nanowire/Electrolyte Interface - The rates of carrier recombination at planar and nanowire Si interfaces were measured using a k-band microwave cavity operating in reflection mode.[32-34] These data were necessary to identify the surface recombination velocity, *S*, for each type of photoelectrode interface and to determine whether the etching process for producing nanowires yielded nanowire surfaces with an inordinate and unusable density of deleterious surface trap states. Figure 5a shows the transient photoconductive decays after optical excitation with $\lambda = 1064$ nm of long bulk-lifetime (> 1 ms) crystalline Si samples in contact with methanol containing dimethylferrocene/dimethylferrocenium ($dmFc^{0/+}$). For materials with long bulk lifetimes of photogenerated minority carriers, τ_{bulk}, the observed photoconductivity decay time constant, τ, reports on the rate of surface recombination,[35]

$$\frac{1}{\tau} = \frac{1}{\tau_{bulk}} + \frac{S}{2d} \approx \frac{S}{2d} \tag{11}$$

where *d* is the thickness of the sample and the factor of 2 arises from recombination at both the front and back surface planes. The surface recombination velocities for these planar Si interfaces in this electrolyte have previously been reported to be 40 cm s^{-1}.[36] The photoconductivity decay response for planar Si corresponded to a nominally equivalent rate of 33 ± 5 cm s^{-1} for *S*. For Si substrates that had been subjected to metal assisted chemical etching that produced a Si nanowire film, a substantial decrease in the measured photoconductivity decay time constant (Figure 5c) was noted. Assuming

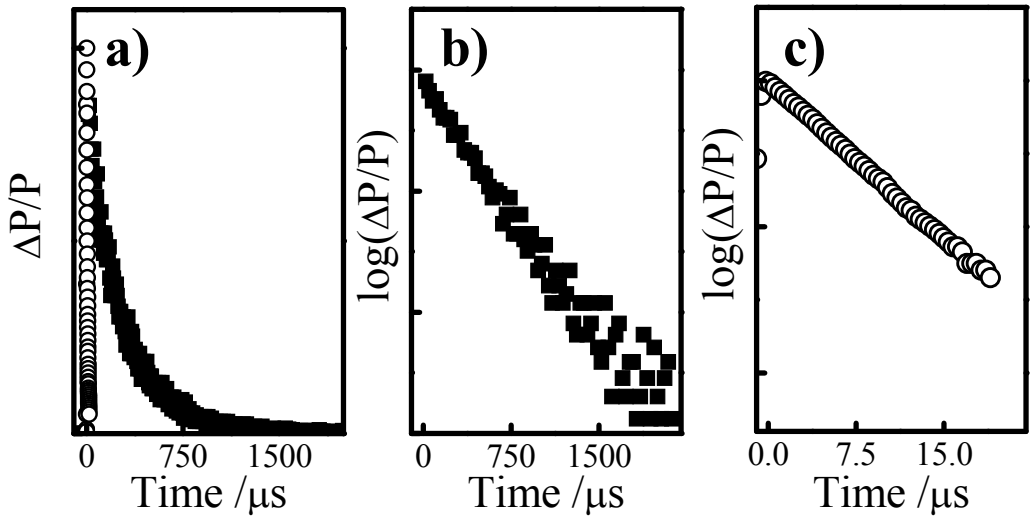

Figure 5.5. (a) Measured transient photoconductivity decay responses following pulsed excitation with λ = 1064 nm for (filled squares) planar Si and for (open circles) a planar Si substrate coated on both faces with a film of nanowires as shown in Figure 4. The y-axis represents the normalized reflected power measured at the detector. (b) The data for the planar Si substrate is shown in semi-log format. (c) The data for the Si substrate coated with nanowire films is shown in semi-log format.

Shockley-Read-Hall recombination processes, the rate of surface recombination relates to the density of surface traps according to Eq 12,[27]

$$S = \nu \sigma N_{t,s} \gamma \tag{12}$$

where σ is the trap cross section (cm^{-2}), ν is the collection velocity (cm s^{-1}), $N_{t,s}$ is the microscopic density of surface traps per unit projected area, and γ is the ratio of the true surface area to the projected surface area. For planar interfaces γ =1. The observed photoconductivity decays implied an increased *total* rate of surface recombination at the Si nanowire film interfaces relative to the planar substrates. However, these data do not indicate an increased value of $N_{t,s}$ for the Si nanowire films. The difference in the observed decay time constants corresponded to a factor of 120, comparable to the ratio of γ for the surface areas of the nanowire and planar interfaces estimated from scanning electron micrographs. These data are instead consistent with the premise that Si nanowires prepared by metal-assisted chemical etching (after removal of the residual metal) do not intrinsically have a significantly different microscopic density of surface traps than planar Si interfaces in this electrolyte.

C. Steady-State J-E Responses Under Illumination - The steady-state *J-E* responses for the planar and nanowire array Si photoanodes under 100 mW cm^{-2} illumination from an ELH source are shown in Figure 6. Figure 6a shows representative responses for planar n-Si and n-Si nanowire photoelectrodes with a dopant density of 4.8 x 10^{15} cm^{-3} and a hole diffusion length, L_p, of 114 μm. The n-Si nanowire film photoelectrodes yielded poorer photoresponses, with consistently *lower* light-saturated photocurrent densities (Table 2). The observed open-circuit photovoltage, V_{oc}, was nominally the same for the two photoelectrode architectures. Figure 6b highlights the photoresponses for planar n-Si and n-Si nanowire photoelectrodes with N_D = 7.8 x 10^{17} cm^{-3} and L_p = 53 μm. In this case, the light-saturated photocurrent densities were routinely *higher* for nanowire photoelectrodes. In addition, the observed values of V_{oc} were consistently smaller for these n-Si nanowire film photoelectrodes than for the planar photoelectrodes. The ideality factors, n, were significantly larger than 1 for both types of n-Si nanowire

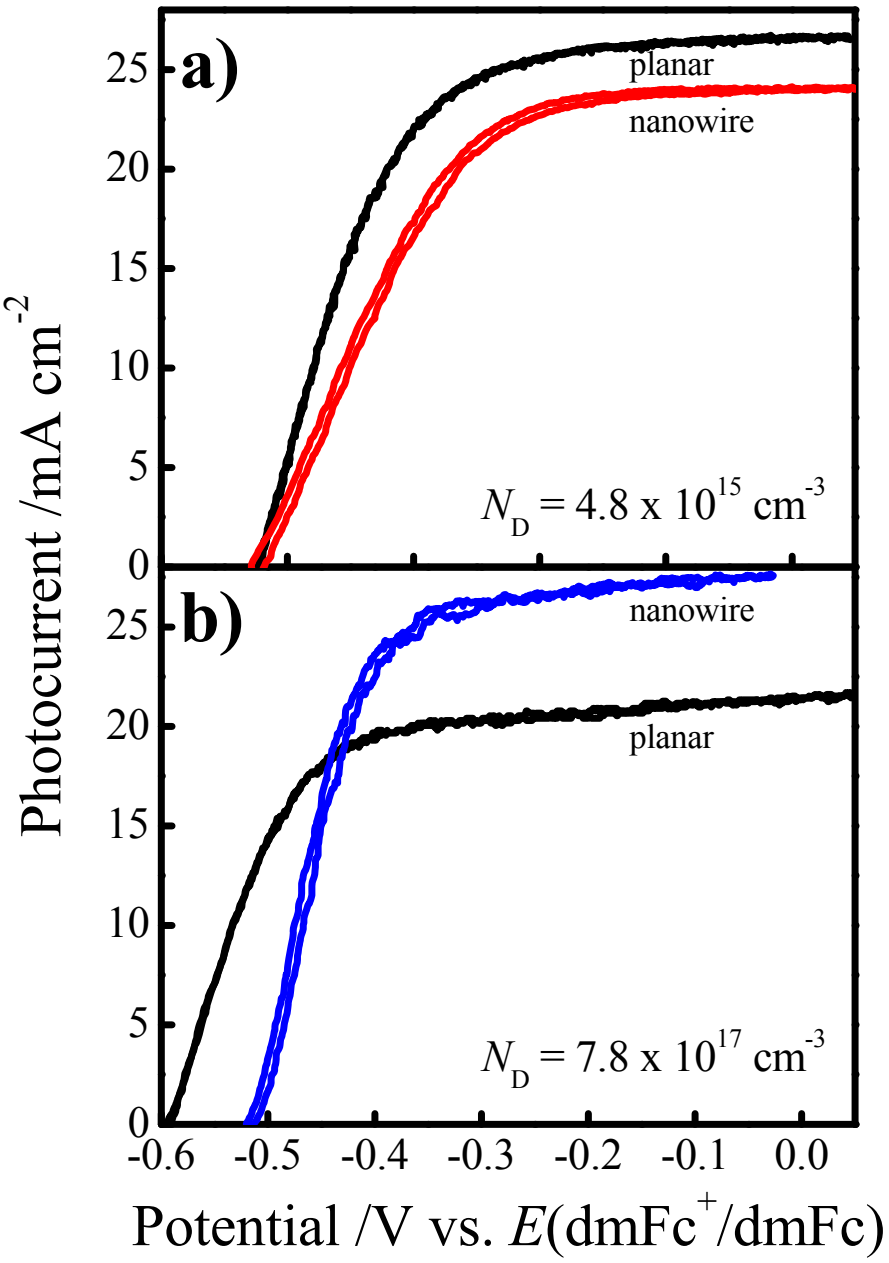

Figure 5.6. Steady-state photocurrent-potential responses for Si photoelectrodes immersed in deaerated methanol solutions containing 1 M $LiClO_4$, 195 mM dimethylferrocene, and 5 mM dimethylferrocenium. (a) Representative responses for (black) a planar and (red) a nanowire film photoelectrode with $N_D = 4.8 \times 10^{15}$ cm^{-3}. (b) Representative responses for (black) a planar and (blue) a nanowire film photoelectrode with $N_D = 7.8 \times 10^{17}$ cm^{-3}.

Table 5.2. Steady-state photoresponses of planar and nanowire photoelectrodes under illumination[a]

N_d /cm^{-3}	*Electrode Architecture*[a]	L_p[b] /μm	J_{sc} /mA cm^{-2}	V_{oc} /V	V_{oc} /V (calc)	n[c]	S /cm s^{-1}
7.8x10^{17}	Planar	53	21±1	0.597±0.02	0.658	1.02±0.02	33±7
7.8x10^{17}	Nanowire Array	53	26±1	0.537±0.03	0.663	1.5±0.3	2340±50
4.8x10^{15}	Planar	114	24±1	0.527±0.005	0.553	1.01±0.01	33±7
4.8x10^{15}	Nanowire Array	114	21±1	0.529±0.001	0.549	1.3±0.2	2340±50

[a] Individual nanowires in the synthesized arrays had a radius of ~30 nm and a length of 14 μm.

[b] L_p was measured from spectral response after (after correcting for reflectance) at long wavelengths.

[c] Values of n were obtained by plotting Ln (J_{sc}) vs V_{oc} at illumination intensities ranging from 100 to 2.6 mW cm^{-2}.

photoelectrodes, in contrast to the values for the respective planar n-Si photoelectrodes (Table 2).

Under white-light illumination, the total *J-E* responses of nanowire films on top of photoactive substrates were convoluted with the response characteristics of the top Si nanowire films and the underlying planar Si substrate. Charge carrier collection efficiencies (quantum yields) vs. wavelength responses were collected for the four types of n-Si photoanodes in this electrolyte. Representative data sets of the external quantum yields (i.e. without correction for interface reflection losses) are highlighted in Figure 7. The optical absorption (Figure 1) of the methanolic electrolyte containing $dmFc^{0/+}$ below 550 nm, in conjunction with the low irradiance of ELH lamps at short wavelengths,[2] effectively limited the white-light photoresponses to $\lambda \geq 550$ nm. Hence, the spectral region from 550 – 1100 nm is shown in Figure 7. In Figure 7a, the n-Si planar photoelectrode with the higher dopant density exhibited lower external quantum yields as compared to the n-Si planar photoelectrode with the lower dopant density, in accord with respective differences in L_p. The Si nanowire array film possessing a dopant density of N_d = 4.8 x 10^{15} cm^{-3} and L_p= 114 μm exhibited only slightly altered quantum yields relative to the to the corresponding planar electrode for $\lambda \geq 890$ nm. This spectral region corresponds to light with optical penetration depths (α^{-1}) much greater than the thickness of the nanowire film height.[23] Hence, for near-bandgap illumination, the light absorption and resultant photoresponses were largely dominated by the underlying bulk substrate. For $\lambda \leq 890$ nm, the optical penetration depths were equal to or less than the height of the Si nanowire film (Figure 7b). At progressively shorter wavelengths, the external quantum yields for the lightly doped n-Si nanowire films decreased as compared to the corresponding planar photoelectrodes. For n-Si nanowire photoelectrodes with N_d = 7.8 x 10^{17} cm^{-3} and L_p = 53 μm, the external quantum yields were greater at every wavelength as compared to the corresponding planar Si photoelectrodes. At wavelengths shorter than 890 nm, the n-Si nanowires with N_d = 7.8 x 10^{17} cm^{-3} yielded significantly higher external quantum yields than both the corresponding planar Si photoelectrode and the n-Si nanowires with N_d = 4.8 x 10^{15} cm^{-3}.

D. Digital Simulations of Nanowire Photoelectrodes - To interpret further the significant differences in the wavelength dependences of the external quantum yields for the two

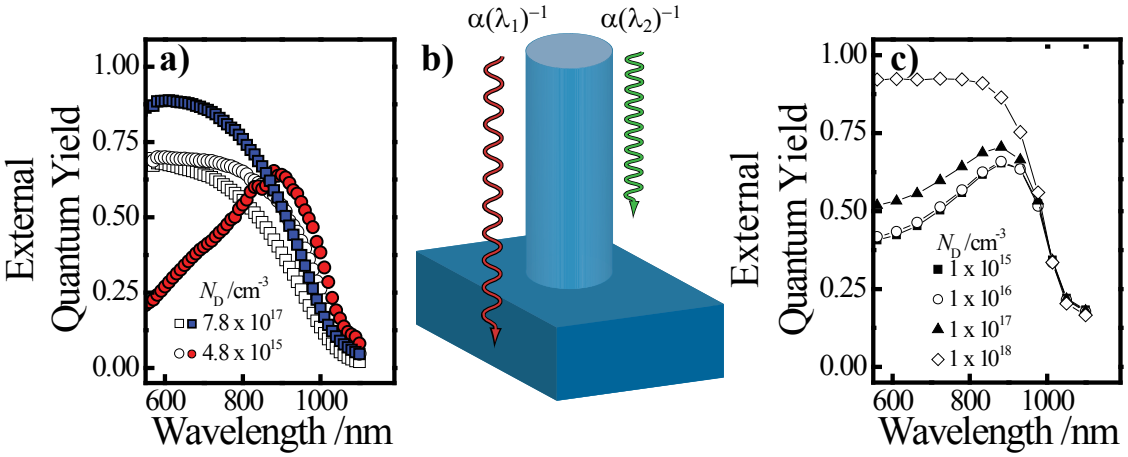

Figure 5.7. (a) Experimentally obtained measurements of the external quantum yield at E_{app}= 0 V of Si photoelectrodes immersed in a methanol solution containing 1 M $LiClO_4$, 4.95 mM dimethylferrocene, and 0.05 mM dimethylferrocenium. Round symbols correspond to data for Si with 4.8 x 10^{15} cm^{-3} and square symbols correspond to data for Si with 7.8 x 10^{17} cm^{-3}. Data for planar substrates and nanowire film photoelectrodes correspond to open and filled symbols, respectively. (b) Representation of the modeled system using TeSCA. The optical penetration depth in each monochromatic simulation was determined by adjusting the value of α^{-1}. Recombination and carrier fluxes at the side planes of the underlying substrate were set to 0 to simulate a slab of infinite length and width. The nanowire radius and height were chosen to match those shown in Figure 4. (c) Simulation results for the quantum yield at E_{app}= 0 V for the modeled Si nanowire system as a function of N_D.

types of n-Si nanowire photoelectrodes, a semiconductor device analysis software package (TeSCA)[21-22,24] based on drift-diffusion models of carrier transport was used to model a cylindrical nanowire on top of a photoactive planar substrate (Figure 7b) in contact with a liquid electrolyte containing a fast outer-sphere redox couple. The modeling software did not account for optical light scattering/trapping effects,[38] imperfections in the nanowire film packing, heterogeneity of the Si nanowire dimensions across macroscale dimensions, or mass transport of dissolved redox species through the film. The influences of these respective effects were assumed to be equal for both types of Si nanowires given their nominally equivalent morphologies. The simulations did account for the interplay between charge-transfer kinetics, surface/bulk recombination centers, and the spatial generation of carriers in a three dimensional heterojunction under constant illumination. The simulations calculated the internal quantum yields for the modeled photoelectrodes. Multiplication of these data with experimentally measured reflectance data for the Si nanowire films allowed direct comparison with the experimentally obtained quantum yield-wavelength data and the simulated quantum yield-wavelength profiles. Figure 12c shows the results of nanowire device simulations based on experimental conditions identical to the experimental data in Figures 1-6. In these simulations, all parameters were held constant except for the dopant density. A value of L_p = 114 μm was chosen to match that of the less doped Si photoelectrodes. At high dopant densities, the internal quantum yield vs wavelength profiles mirrored the data in Figure 6 for the high dopant density Si nanowire photoelectrodes. As the dopant density was lowered, the quantum yield-wavelength profile changed significantly with markedly decreased quantum yields at wavelengths shorter than 890 nm. At dopant densities comparable to the experimental data for the lightly doped Si nanowires in Figure 6, the general profile and local maximum of the quantum yield-wavelength response was captured. These simulations suggest that dopant density was the dominant factor that influenced the charge carrier collection properties of the studied n-Si nanowires, much more so than the values of L_p.

Additional numerical simulations were performed to further elucidate the interplay of dopant density with other system variables such as r, S, and L_p on the charge-carrier collection properties of an individual nanowire photoelectrode. For these

simulations, the modeled photoelectrode consisted of a single nanowire with a height of 100 μm and no underlying photoactive substrate immersed in an electrolyte where $q\Phi_b$ = 1eV, contacted at the bottom with an ideal ohmic contact ($S = \infty$), and illuminated with monochromatic light with λ = 105.2 cm^{-1} (α^{-1} = 95 μm) at a photon flux of 1.25 x 10^{17} photons cm^{-2} s^{-1}. The range of simulated S values corresponded to the range of surface recombination velocities typically encountered experimentally for Si interfaces.[35] The full *J-E* responses are reproduced in the Figure 8-11. Figures 12a-d summarize the internal collection efficiency at E_{app} = 0 V (short-circuit conditions) for these simulations. The data are plotted against the dopant density used for each particular simulation. In each data set, the dopant density that gave the condition $r/W = 1$ is indicated by a dashed line. Figures 12a and 12c show that for a comparatively thin nanowire (r = 50 nm), the internal quantum yield for carrier collection was 1 for all values of S when the dopant density is large enough that $r/W >> 1$, irrespective of the value of L_p. For dopant densities where $r/W \leq 1$, the predicted internal quantum yields decreased with smaller values of N_D. For simulations with a large value of L_p (Figure 12a), the lowest predicted internal quantum yield and the steepness in decline of internal quantum yield was strongly sensitive to the value of S. For simulations with small values of L_p (Figure 12c), the predicted internal quantum yields were essentially insensitive to the value of S, and internal quantum efficiencies equal to 1 only occurred for values of N_D that were large enough so that $r/W >> 1$. Figures 12b and 12d show the corresponding results for a larger nanowire photoelectrode with r = 500 nm. Due to the increased radius, the condition r/W =1 occurs at a much lower dopant density than shown in Figures 12a and 12c. The same qualitative trends regarding S and L_p were observed for the simulations in Figures 12b and 12d, although the total decrease in the internal quantum yield was not as severe in each corresponding simulation set.

IV. Discussion.

The steady-state *J-E* data presented here illustrate that a high-aspect-ratio photoelectrode form factor, even with materials with excellent bulk electrical properties (i.e. large values of L_p), does not necessarily guarantee improved or 'good' photoresponse characteristics. The data in Figure 6 show that photoelectrodes comprised

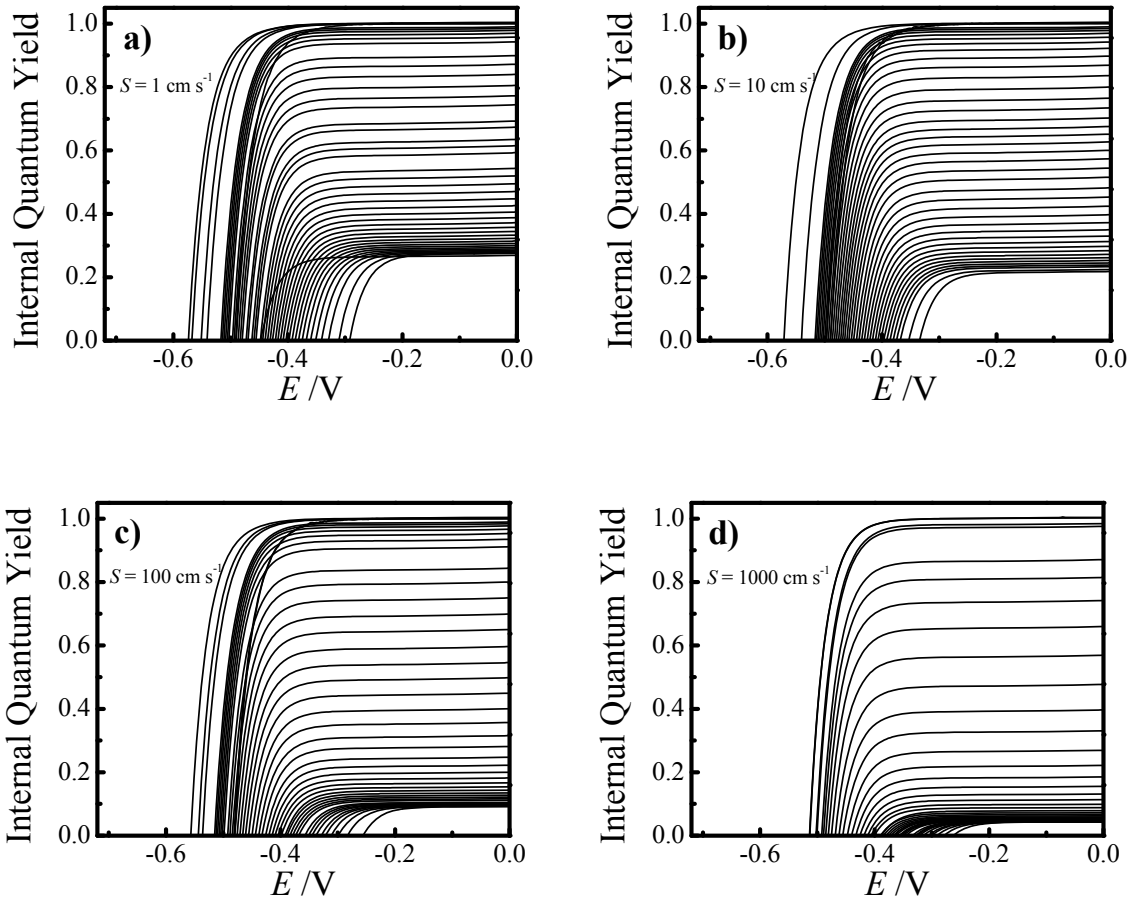

Figure 5.8. Simulated steady-state photocurrent-potential responses for a nanowire heterojunction with r = 50 nm, $q\Phi_b$ = 1 eV, and L_p = 50 μm. The four sets of plots correspond to the data in Figure 12a, with the value of S indicated on each plot.

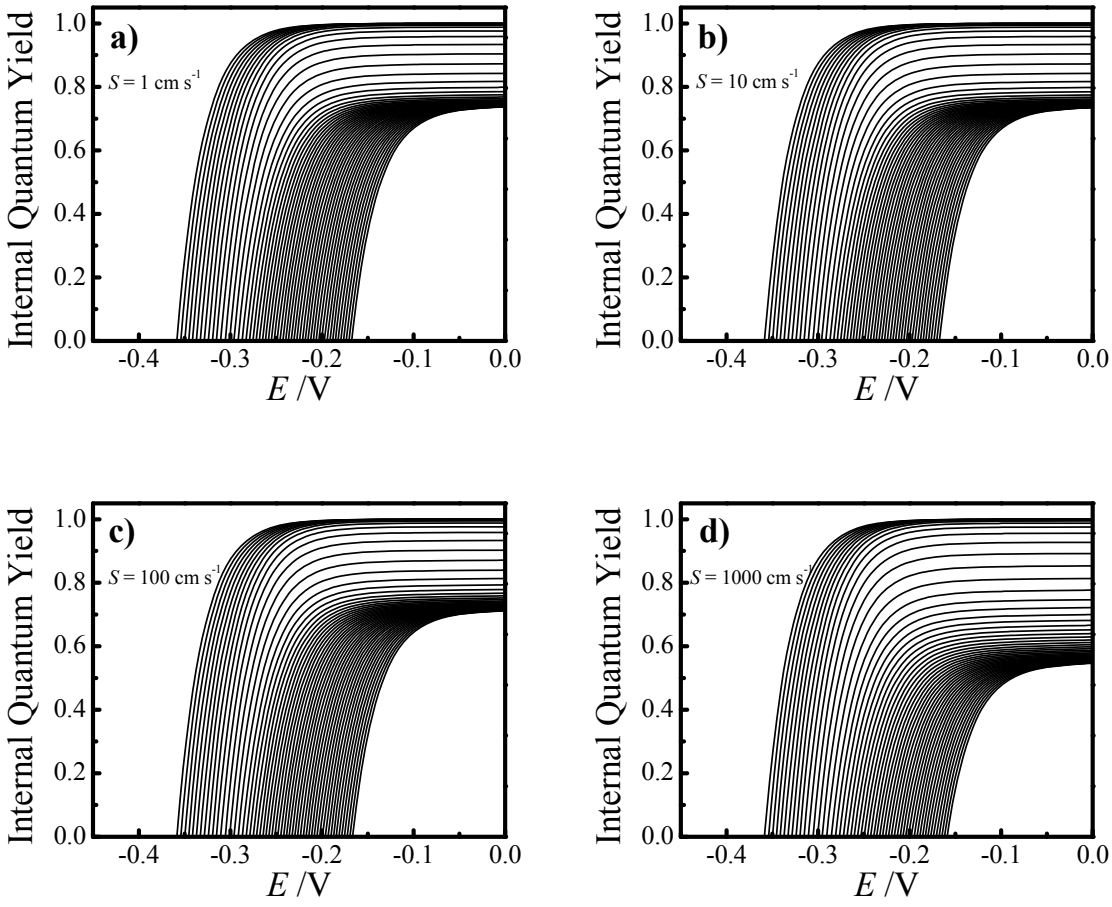

Figure 5.9. Simulated steady-state photocurrent-potential responses for a nanowire heterojunction with r = 500 nm, $q\Phi_b$ = 1 eV, and L_p = 50 μm. The four sets of plots correspond to the data in Figure 12b, with the value of S indicated on each plot.

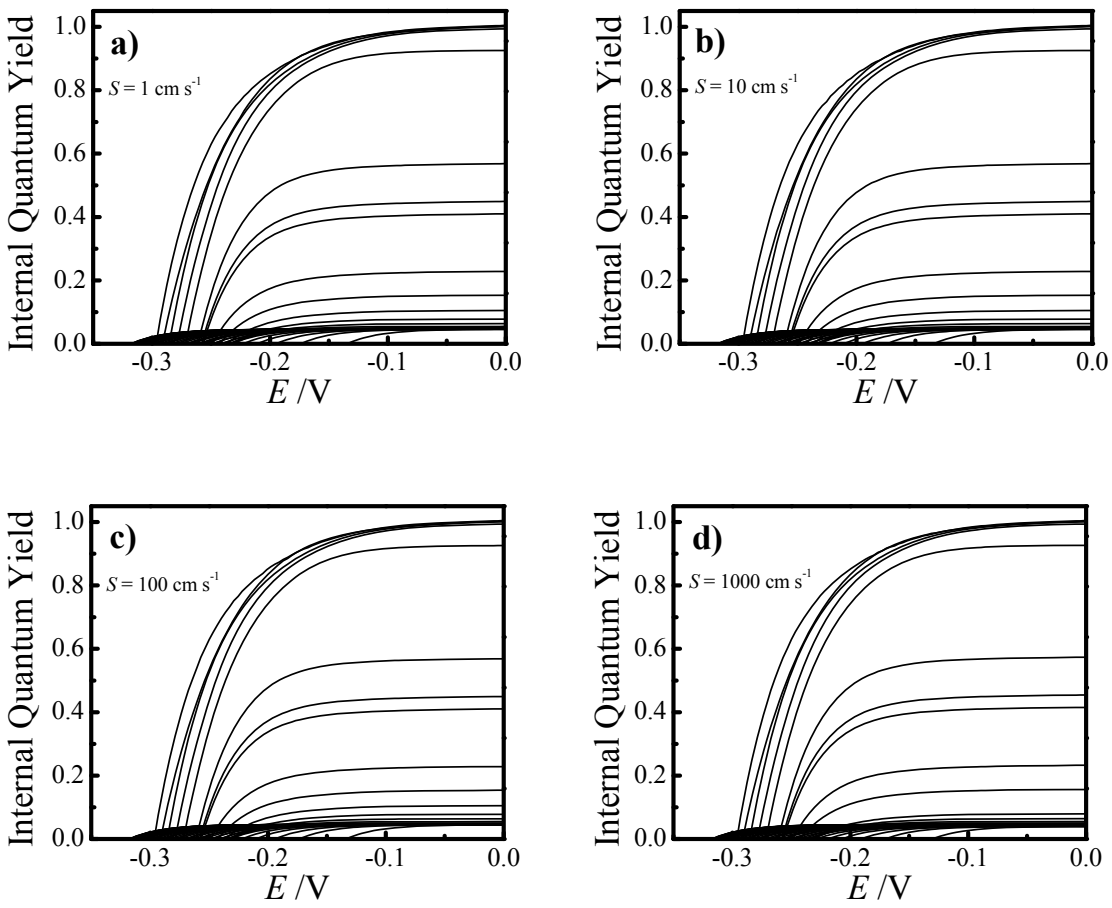

Figure 5.10. Simulated steady-state photocurrent-potential responses for a nanowire heterojunction with r = 50 nm, $q\Phi_b$ = 1 eV, and L_p = 5 μm. The four sets of plots correspond to the data in Figure 12c, with S values indicated on each plot.

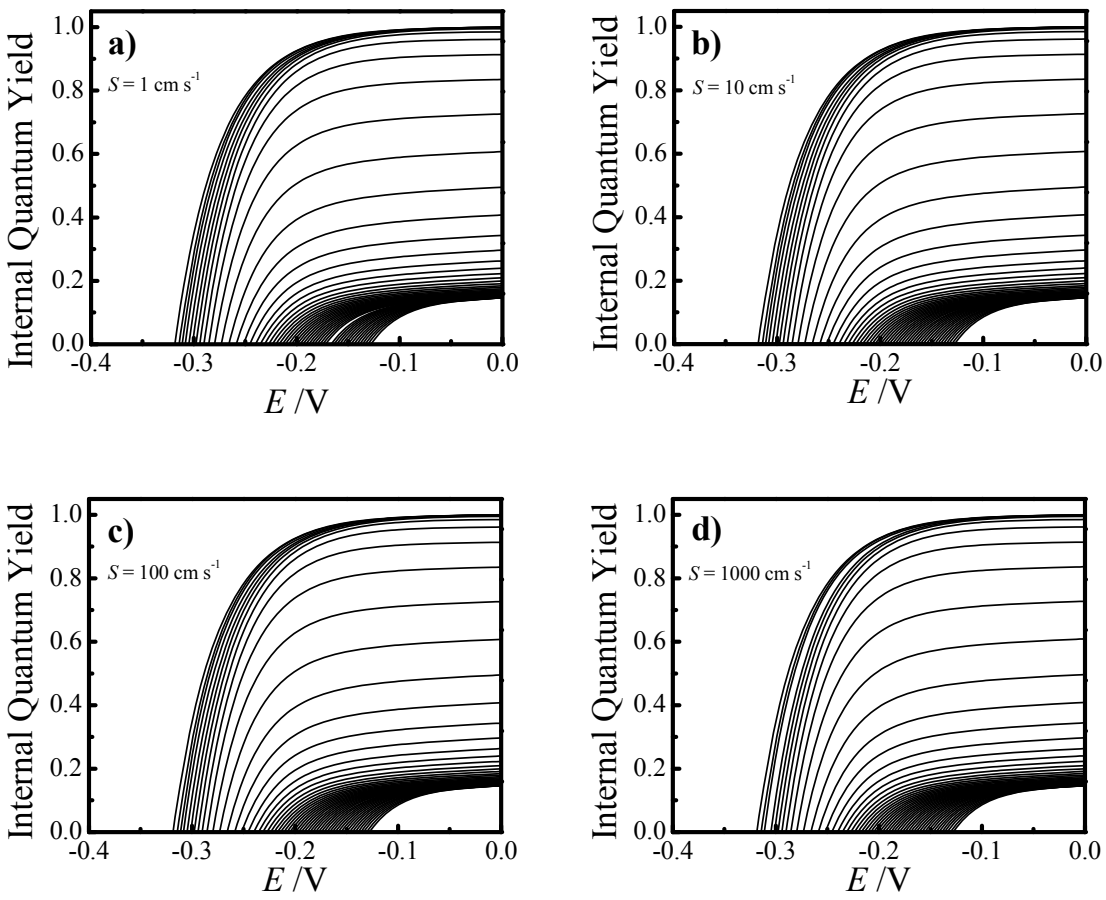

Figure 5.11. Simulated steady-state photocurrent-potential responses for a nanowire heterojunction with r = 500 nm, $q\Phi_b$ = 1 eV, and L_p = 5 μm. The four sets of plots correspond to the data in Figure 12d, with the value of S indicated on each plot.

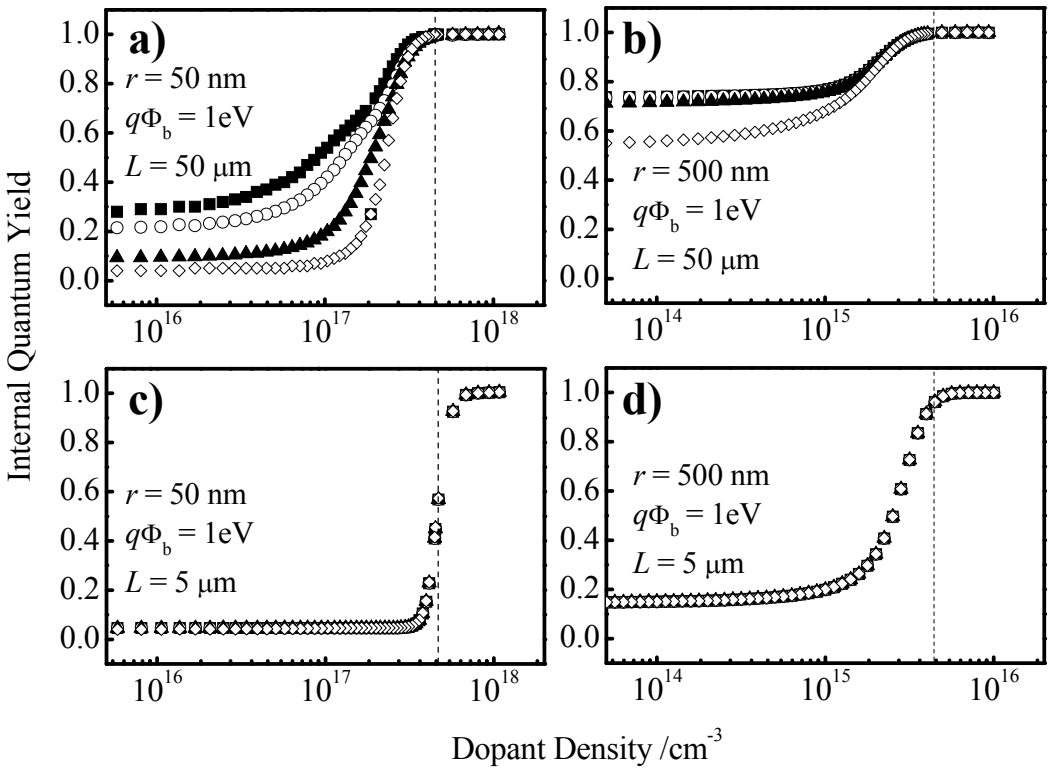

Figure 5.12. Simulation results for the internal quantum efficiency at E_{app} = 0 V of a single Si nanowire heterojunction (without an underlying photoactive support substrate) under monochromatic illumination (α^{-1} = 95 μm) with the simulation parameters as described in the text. For each data set, the calculated internal quantum yield for each level of doping was determined for a specific value of *S*. Filled squares, open circles, filled triangles, and open diamonds correspond to *S* values of 1, 10, 100, and 1000 cm s^{-1}. For each plot, the dashed line highlights the dopant density where *r/W* = 1. (a) Simulation results for a Si nanowire with a 50 nm radius in contact with an electrolyte yielding $q\Phi_b$ = 1 eV and possessing a value of L_p = 50 μm. (b) Simulation results for a Si nanowire with a 500 nm radius in contact with an electrolyte yielding $q\Phi_b$ = 1 eV and possessing a value of L_p = 50 μm. (c) Simulation results for a Si nanowire with a 50 nm radius in contact with an electrolyte yielding $q\Phi_b$ = 1 eV and possessing a value of L_p = 5 μm. (d) Simulation results for a Si nanowire with a 500 nm radius in contact with an electrolyte yielding $q\Phi_b$ = 1 eV and possessing a value of L_p = 5 μm.

of a substrate coated with Si nanowires with radii too small to support a full depletion width exhibit a lowered capacity for optical to electrical energy conversion. For these electrodes, the total attainable photocurrents were measurably lower than the photocurrents of the analogous planar Si photoelectrode. In addition, the value of V_{oc} was the same for the nanowire-containing photoelectrodes and the planar photoelectrodes. These observations are consistent with the notion that the majority of the *net* photocurrent is passed across the exposed planar/solution interface rather than the nanowire/solution interface. The presented photoelectrochemical data also highlight that nanowires with the exact same morphological features and even poorer bulk optoelectronic properties but doped enough to support an internal electric field can give good photoresponses. For the more heavily doped Si nanowire photoelectrodes, a marked enhancement in the light-saturated photocurrent was observed that resulted in better visible light conversion efficiency. The values of V_{oc} for the more heavily doped Si nanowire photoelectrodes were lower than the corresponding planar Si photoelectrodes, consistent with the premise that most of the *net* photocurrent was passed across the nanowire/solution interface. For a given illumination level at high-aspect-ratio photoelectrodes, a decrease in V_{oc}, relative to comparable planar photoelectrodes, is expected due to a reduced quasi-Fermi level splitting caused by a dilution of the photocurrent across a larger total interfacial area.[39]

The wavelength dependence of the quantum yield at short-circuit for photogenerated charge-carrier collection could be correlated to either the nanowire top film or the underlying substrate. For light with long optical penetration depths relative to the thickness of the nanowire film, the measured quantum yield reports strongly on the properties of the underlying photoactive support. For light with short optical penetration depths relative to the thickness of the nanowire film, the measured quantum yield reports strongly on the operation of the nanowire photoelectrode. In nanowire systems such as those reported here where the optoelectronic, chemical, and kinetic terms are known, the results of the numerical simulations show that the quantum yield responses of nanowire photoelectrodes under low-injection level conditions, i.e. the illumination levels where photogenerated carriers only significantly change the population of minority carriers in the semiconductor,[40] are readily predictable and interpretable using established

semiconductor heterojunction device physics.[10] The experimental data confirm that the quantum yield characteristics of nanowire photoelectrodes with radii too large for quantum confinement-effects are largely governed by the ability of the nanowire to support an internal electric field. The maximum electric field, $\in_{max}$, at the interface is a strong function of the semiconductor dopant density.[11]

$$\in_{max} = \sqrt{\frac{2qN_D\left(\Phi_b + \frac{k_BT}{q}\ln\left(\frac{N_D}{N_{CB}}\right)\right)}{\varepsilon\varepsilon_0}} \tag{13}$$

For low-injection level conditions, the internal field is necessary to simultaneously direct minority carriers towards the surface (front contact) and majority carriers towards the bulk (back contact). The net velocity for directing charge-carriers either towards (minority carriers) or away (majority carriers) from the interface is given by the drift velocity, v_d (Figure 13)

$$v_{d,n} = \mu_n \in_{max} \tag{14a}$$

$$v_{d,p} = \mu_p \in_{max} \tag{14b}$$

where μ_n and μ_n are the carrier mobilities for electrons and holes, respectively. When the value of r for a nanowire is less than W, the semiconductor nanowire cannot support the full electric field between the surface and bulk regions. Without the full electric field strength pushing majority carriers away from the interface, recombination losses at low dopant concentrations are incurred because of high densities of both majority and minority carriers at the interface (Figure 13).[5] Hence, when $r/W < 1$, the attainable quantum yield of charge carriers decreases because of higher *majority* carrier-induced recombination losses at the surface and not because of a decrease in the electrical conductivity of the bulk. In the absence of any significant field, the densities of acceptor/donor states of the contacting material and the heterogeneous charge-transfer rate constants (k_{et} and k_{ht} for electrons and holes, respectively) control the extent of

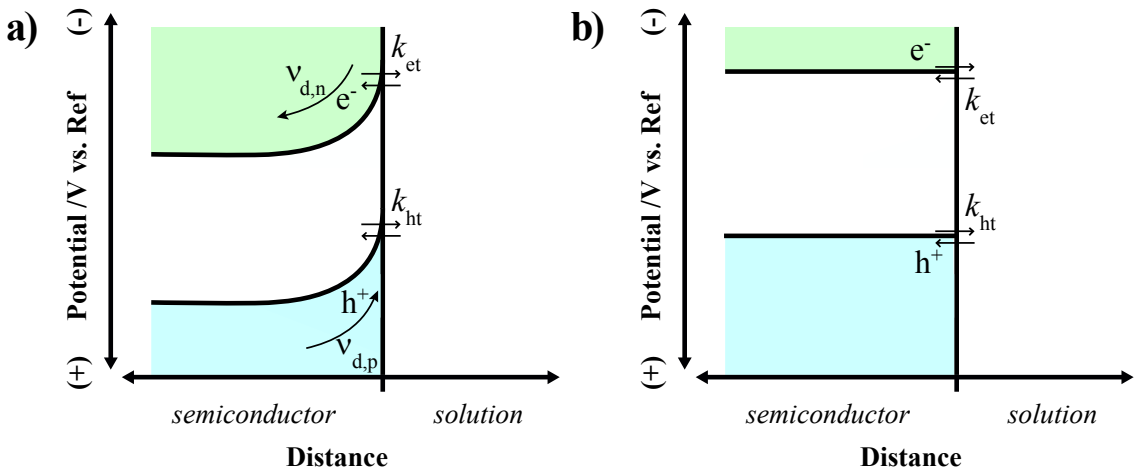

Figure 5.13. Schematic diagram illustrating the processes governing the direction and collection of photogenerated majority and minority carriers at an ideal n-type semiconductor/liquid heterojunction devoid of surface traps. The drift velocity set by the internal electric field sweeps majority and minority carriers away from/towards the front interface, respectively. The rate of carrier charge transfer across the front interface is influenced by the rate constants k_{et} and k_{ht} for electrons and holes, respectively. (a) A heterojunction with a semiconductor sufficiently capable of supporting an internal field. (b) A heterojunction with a semiconductor incapable of supporting an internal electric field.

majority carrier-induced recombination loss. For intimate semiconductor/metal contacts where the rate of majority carrier charge-transfer is intrinsically high,[41] majority carrier-induced recombination losses can be severe.[41-42] For this reason, the comparatively lower density of acceptor states in liquid electrolytes[43] and conducting polymers[44] naturally represent more tenable contacting materials than metals for nanowire photoelectrodes. The simulations presented here assumed heterogeneous rate constants commensurate with fast outer-sphere redox couples (Table 1). Simulations where the value of k_{et} were further decreased by several orders of magnitude did not yield appreciably different photoresponses. Irrespective, the net result in the presented dataset is that the dominant and overwhelming factor in determining the charge-carrier collection efficiency of nanowire photoelectrodes is N_D rather than L_p or S. Even for materials where the bulk and surface electrical properties are excellent, i.e. $L_p >> r$ and $S = 1$ cm s^{-1}, poor photoresponse characteristics will be observed if the value of N_D is too low.

The simulation results presented here also suggest that certain nanowire photoelectrodes may still be able to function effectively even without a significant internal electric field. For the larger nanowires possessing low dopant densities, the simulated incident photon flux of 1.25×10^{17} photons cm^{-2} s^{-1} corresponds to high level injection conditions, i.e. the photogenerated carriers significantly change the populations of both carrier types. For high level injection conditions, photoelectrodes can operate with efficient optical energy conversion efficiencies without a large internal electric field.[40,45-46] For example, point-contact solar cells (e.g. 'Swanson' cells as manufactured by SunPower®) utilize lightly doped Si that cannot support large internal electric fields but have long carrier diffusion lengths and small values of interfacial recombination.[47-48] In this design, spatially distributed ohmic selective contacts produce diffusional gradients that allow large quasi-Fermi level splitting and excellent carrier collection efficiencies. The simulation results in Figure 12 for the larger nanowires indicate that if the conditions of a reasonably large value of L_p and a small value of S are satisfied, significant internal quantum yields can still be obtained even in the absence of a significant internal field, i.e. values of N_D where $r/W < 1$. As in the case of 'planar' point-contact solar cells, the type and position of contacts should become important in determining the upper limit of the internal quantum yield of nanowire cells operating under high level injection. Such

factors were not explored here; and, to our knowledge, no experimental or modeling data on nanowire solar cells intentionally operating without an internal electric field while under high level injection conditions have been reported. The data presented here suggests lightly doped nanowires operating under high-level injection may be worth exploring. For further clarification, lightly doped nanostructured semiconductors are regularly used in dye-sensitized photoelectrochemical cells. In those systems, the nanostructured semiconductor is not the main light absorber and the collection of photogenerated carriers depends entirely on the kinetic terms of the system (e.g. k_{et}). The principles and issues of dye-sensitized systems have been extensively documented and discussed,[49] and are fundamentally different than the lightly doped nanowire photoelectrode operating under high level injection conditions discussed here.

Although the presented experimental and simulation results describe a specific Si nanowire heterojunction system, the general implications of these data extend to other materials where high aspect ratio form factors are useful for overcoming carrier collection limitations. According to Eq 1, a hypothetical 10 nm radius nanowire photoelectrode contacted with an electrolyte that yields $q\Phi_b$ = 2 eV requires a dopant density in excess of 10^{19} cm^{-3} to satisfy the condition of $r/W \geq 1$ and to avoid the majority carrier-based recombination losses described above, irrespective of the values of L_p and S. Such high dopant densities correspond to degenerately doped conditions. For degenerately doped semiconductors, additional deleterious processes such as the tunneling[10] of majority carriers from the bulk through the depletion region and Auger recombination[16] further hinder photoelectrode optical energy conversion efficiency. Hence, for low-level injection, the upper limit for the usable dopant concentration in nanowire photoelectrodes is bound to levels below degenerate doping conditions. Coupled with the lower doping level set by the nanowire radius, the working 'window' for optimal dopant density for nanowire photoelectrodes operating at low-injection levels is readily definable. In general, controlling the precise level of doping in semiconductors that are less developed than Si can be difficult. For novel materials such as TaON[50] or Ta_3N_5[51] where the identity of dopants is unclear, the simultaneous control over size and doping presents a formidable materials challenge. Hence, in order to utilize low-cost but underdeveloped semiconductors with intrinsically short values of L_p as useful

photoelectrode materials, a primary emphasis for development should be placed on controlling the dopant density and morphology in concert. Without first satisfying these criteria, attempts to minimize surface recombination[52] or to increase the electrocatalytic activities[53] of nanowire photoelectrodes will ultimately not result in substantially improved photoelectrode responses.

A final note should be made regarding more complex nanostructured photoelectrode geometries. Macro/mesoporous semiconductor films[1-2] and semiconductor nanotubes[50-51,54-58] offer similar conceptual advantages for separating light absorption and carrier collection. Although a detailed investigation of each specific photoelectrode morphology is needed to understand fully the factors for operation, the wall thicknesses in these materials will have a role comparable to the radii in nanowires. Hence, details regarding doping conditions should still be a dominant influence on the performance of these nanostructured photoelectrodes. In addition, recent reports of highly branched, crystalline nanowire materials have extended the possibility of nanowire photoelectrode design.[59-60] The ability to uniformly and precisely dope branched semiconductor nanowires has not been rigorously demonstrated or explored. The influence of non-uniform dopant density profiles, particularly in the presence of sharp junctions that may separately distort the internal electric field, needs to be more fully understood in order to better develop these materials for solar energy conversion applications. The data presented here are specifically focused on systems where the dopant density was uniform throughout the semiconductor volume. Work is ongoing to model more structurally and compositionally complex photoelectrode architectures.

V. Summary.

The steady-state photoelectrochemical responses of semiconductor nanowire arrays in nonaqueous regenerative photoelectrochemical cells were analyzed. Under white light illumination, the photocurrent-potential responses of the Si nanowire arrays were strongly influenced by their respective levels of doping. Lightly doped Si nanowire arrays consistently showed lower light-saturated photocurrents than heavily doped Si nanowire arrays, despite having minority carrier diffusion lengths that were larger by a factor of 2. Analyses of the spectral response characteristics of the Si nanowire arrays

separated out the effects from the underlying Si substrate and highlighted that carrier-collection was either significantly enhanced or suppressed by the Si nanowires depending on the value of r/W established by the equilibrium barrier height and dopant density. Simulation results confirmed the sensitivity of the collection efficiency of monochromatic light to dopant density for nanowire photoelectrodes with small radii. In particular, although high aspect ratio photoelectrode form factors circumvent minority carrier-based recombination losses, sub-optimal doping conditions invariably lead to severe majority carrier-based recombination losses. The data thus suggest that continued development of semiconductor materials as nanowire photoelectrodes requires precise control over both the morphology and doping levels.

VI. References.

1. Maiolo, J. R.; Atwater, H. A.; Lewis, N. S. *J. Phys. Chem. C* **2008**, *112*, 6194.
2. Price, M. J.; Maldonado, S. *J. Phys. Chem. C* **2009**, *113*, 11988.
3. Kayes, B. M.; Atwater, H. A.; Lewis, N. S. *J. Appl. Phys.* **2005**, *97*, 114302.
4. Garnett, E. C.; Yang, P. *J. Am. Chem. Soc.* **2008**, *130*, 9224.
5. Fonash, S. *Solar Cell Device Physics*; Academic Press: New York, 1982.
6. Kennedy, J. H.; Frese, K. W. *J. Electrochem. Soc.* **1978**, *125*, 709.
7. Lindgren, T.; Wang, H.; Beermann, N.; Vayssieres, L.; Hagfeldt, A.; Lindquist, S. E. *Sol. Energ. Mat. Sol. C.* **2002**, *71*, 231.
8. Mohapatra, S. K.; John, S. E.; Banerjee, S.; Misra, M. *Chem. Mater.* **2009**, *21*, 3048.
9. Beermann, N.; Vayssieres, L.; Lindquist, S. E.; Hagfeldt, A. *J. Electrochem. Soc.* **2000**, *147*, 2456.
10. Sze, S. M.; Ng, K. K. *Physics of Semiconductor Devices*; 3 ed.; John Wiley & Sons, Inc.: Hoboken, 2007.
11. Tan, M. X.; Laibinis, P. E.; Nguyen, S. T.; Kesselman, J. M.; Stanton, C. E.; Lewis, N. S. *Principles and Applications of Semiconductor Photoelectrochemistry*; John Wiley & Sons: Hoboken, 1994.
12. Kelzenberg, M. D.; Turner-Evans, D. B.; Kayes, B. M.; Filler, M. A.; Putnam, M. C.; Lewis, N. S.; Atwater, H. A. In *IEEE Photovoltaic Specialists Conference* 2009; Vol. 1, p 1449.
13. Yuan, G.; Zhao, H.; Liu, X.; Hasanali, Z. S.; Zou, Y.; Levine, A.; Wang, D. *Angew. Chem. Int. Ed.* **2009**, *48*, 9680.
14. Rosenbluth, M. L.; Lewis, N. S. *J. Am. Chem. Soc.* **1986**, *108*, 4689.
15. Geiger, T.; Nottenberg, R.; Pelaprat, M. L.; Gratzel, M. *Helv. Chim. Acta* **1982**, *65*, 2507.
16. Kerr, M. J.; Cuevas, A. *J. Appl. Phys.* **2002**, *91*, 2473.
17. Zhang, M. L.; Peng, K. Q.; Fan, X.; Jie, J. S.; Zhang, R. Q.; Lee, S. T.; Wong, N. B. *J. Phys. Chem. C* **2007**, *112*, 4444.
18. Peng, K.; Xu, Y.; Wu, Y.; Yan, Y.; Lee, S. T.; Zhu, J. *Small* **2005**, *1*, 1062.
19. Bansal, A.; Lewis, N. S. *J. Phys. Chem. B* **1998**, *102*, 1067.
20. Bard, A. J.; Faulkner, L. R. *Electrochemical Methods: Fundamentals and Applications*; John Wiley & Sons: Hoboken, 2001.
21. Krueger, O.; Jung, C.; Gajewski, H. *J. Phys. Chem.* **1994**, *98*, 12653.
22. Krueger, O.; Jung, C.; Gajewski, H. *J. Phys. Chem.* **1994**, *98*, 12663.
23. Green, M. A.; Keevers, M. *Prog. Photovoltaics* **1995**, *3*, 189.
24. Anz, S. J.; Kruger, O.; Lewis, N. S. *J. Phys. Chem. B* **1998**, *102*, 5625.
25. Anz, S. J.; Lewis, N. S. *J. Phys. Chem. B* **1999**, *103*, 3908.
26. Wang, Y.; Cheung, K. P. *Appl. Phys. Lett.* **2007**, *91*, 113509.
27. Yablonovitch, E.; Allara, D. L.; Chang, C. C.; Gmitter, T.; Bright, T. B. *Phys. Rev. Lett.* **1986**, *57*, 249.
28. Gerischer, H. *Adv. Electroch. El. Eng.* **1961**, *1*, 139.
29. Lewis, N. S. *Ann. Rev. Phys. Chem.* **1991**, *42*, 543.
30. Velmurugan, J.; Sun, P.; Mirkin, M. V. *J. Phys. Chem. C* **2009**, *113*, 459.
31. Sun, P.; Mirkin, M. V. *Anal. Chem.* **2006**, *78*, 6526.
32. Kunst, M.; Beck, G. *J. Appl. Phys.* **1986**, *60*, 3558.
33. Schmidt, J.; Aberle, A. G. *J. Appl. Phys.* **1997**, *81*, 6186.

34. Schofthaler, M.; Brendel, R. *J. Appl. Phys.* **1994**, *77*, 3162.
35. Yablonovitch, E.; Gmitter, T. J. *Sol. St. Electron.* **1992**, *35*, 261.
36. Forbes, M. D. E.; Lewis, N. S. *J. Am. Chem. Soc.* **1990**, *112*, 3682.
37. Gartner, W. W. *Phys. Rev.* **1959**, *116*, 84.
38. Li, J.; Yu, H.; Wong, S. M.; Li, X.; Zhang, G.; Lo, P. G.; Kwong, D. L. *Appl. Phys. Lett.* **2009**, *95*, 243113.
39. Spurgeon, J. M.; Atwater, H. A.; Lewis, N. S. *J. Phys. Chem. C* **2008**, *112*, 6186.
40. Tan, M. X.; Kenyon, C. N.; Kruger, O.; Lewis, N. S. *J. Phys. Chem. B* **1997**, *101*, 2830.
41. Green, M. A. *J. Appl. Phys.* **1976**, *47*, 547.
42. Price, M. J.; Foley, J.; Maldonado, S. *manuscript in preparation* **2010**.
43. Kumar, A.; Lewis, N. S. *J. Phys. Chem.* **1990**, *94*, 6002.
44. Lonergan, M. *Ann. Rev. Phys. Chem.* **2004**, *55*, 257.
45. Kenyon, C. N.; Tan, M. X.; Kruger, O.; Lewis, N. S. *J. Phys. Chem. B* **1997**, *101*, 2850.
46. Kruger, O.; Kenyon, C. N.; Tan, M. X.; Lewis, N. S. *J. Phys. Chem. B* **1997**, *101*, 2840.
47. King, R. R.; Sinton, R. A.; Swanson, R. M. *Appl. Phys. Lett.* **1989**, *54*, 1460.
48. Sinton, R. A.; Swanson, R. M. *IEEE Trans. Elect. Dev.* **1987**, *34*, 2116.
49. Peter, L. *Acc. Chem. Res.* **2009**, *42*, 1839.
50. Abe, R.; Tsuyoshi, R.; Hideki, S.; Domen, K. *Chem. Lett.* **2005**, *34*, 1162.
51. Feng, X.; LaTempa, T. J.; Basham, J. I.; Mor, G. K.; Varghese, O. K.; Grimes, C. A. *Nano Lett.* **2010**, *10*, 948.
52. Dare-Edwards, M. P.; Goodenough, J. B.; Hamnett, A.; Trevellick, P. R. *J. Chem. Soc. Faraday T.* **1983**, *79*, 2027.
53. Zhong, D. K.; Sun, J.; Inumaru, H.; Gamelin, D. R. *J. Am. Chem. Soc.* **2009**, *131*, 6086.
54. Wei, J.; Jia, Y.; Shu, Q.; Gu, Z.; Wang, K.; Zhuang, D.; Zhang, G.; Wang, Z.; Luo, J.; Cao, A.; Wu, D. *Nano Lett.* **2007**, *7*, 2317.
55. Banerjee, S.; Mohapatra, S. K.; Misra, M. *Chem. Comm.* **2009**, *44*, 7137.
56. LaTempa, T. J.; Feng, X.; Paulose, M.; Grimes, C. A. *J. Phys. Chem. C* **2009**, *113*, 16293.
57. Mor, G. K.; Varghese, O. K.; Wilke, R. H. T.; Sharma, S.; Shankar, K.; Latempa, T. J.; Choi, K.-S.; Grimes, C. A. *Nano Lett.* **2008**, *8*, 1906.
58. Mor, G. K.; Prakasam, H. E.; Varghese, O. K.; Shankar, K.; Grimes, C. A. *Nano Lett.* **2007**, *7*, 2356.
59. Gur, I.; Fromer, N. A.; Chen, C. P.; Kanaras, A. G.; Alivisatos, A. P. *Nano Lett.* **2007**, *7*, 409.
60. Bierman, M. J.; Jin, S. *Energy Environ. Sci.* **2009**, *2*, 1050.

Chapter 6
Conclusions and Future Directions

I. General Findings.

Novel materials and material architectures for light-harvesting devices were investigated in this thesis. Two sets of organic chromophore systems are characterized for applications as light absorbers and exciton transport materials in solar energy conversion systems, and two nanostructured inorganic semiconductor systems are the subject of study for applications in light-harvesting devices.

Controlling exciton trapping through the inclusion of tailored defect sites was demonstrated in Chapter 2. Energy transfer rates were studied in a series of multi-chromophore systems composed entirely of triarylamine, which differed only in the connectivity of dye molecules. When the arrangements included a biphenyl unit, excitons were directed to and trapped on the biphenyl site with 98% efficiency. Trapping occurred as the result of the planarization of the biphenyl unit during excited state relaxation. The presented results demonstrated that subtle variations in the arrangement of chromophores strongly influenced energy migration and the location of trap sites within a multi-chromophore system.

The effect of a cyclical arrangement of dye molecules on the photophysical properties of the multi-chromophore system was investigated in Chapter 3. Two-photon excitation fluorescence measurements and fluorescence upconversion anisotropy measurements were performed on a series of cyclical thiophenes. The chromophore coupling constants were determined from fluorescence anisotropy measurements and were substantially higher than in linear chains. The two-photon cross section was measured through two-photon fluorescence excitation microscopy and was found to be unusually high. This was attributed to the strong coupling between chromophores.

Chapter 4 described the first successful preparation of macroporous p-GaP(100) by anodic etching. Macroporous p-GaP(100) was predicted to be a more stable electrode material for photosynthetic water-splitting, and also to have interesting optical properties. Preliminary measurements of this material as a photocathode for the reduction of hydrogen showed a small enhancement of the energy conversion efficiency with visible light over planar p-GaP(100), but further optimization of nanostructure is expected to lead to significant gains.

Chapter 5 constituted the first complete quantitative analysis of the relationship between the capacity to support an internal electric field and photogenerated carrier collection efficiency in semiconductor nanowire photoelectrodes. A series of nanowire photoelectrodes, with nominally similar morphologies but varying levels of doping, were prepared. The solar energy conversion efficiencies of these platforms were compared. Lightly doped nanowires, which had a corresponding depletion width larger than the radius of the nanowire, were largely inactive for energy conversion. Heavily doped nanowires were active for solar energy conversion and demonstrated improved conversion efficiencies relative to the planar photoelectrodes. Numerical simulations verified the experimental results and further elucidated the interplay between minority carrier diffusion lengths, surface recombination, and nanowire radius in Si nanowire photoelectrodes.

II. Future Directions.

A. Triarylamine Dendrimers – The triarylamine dendrimers investigated in Chapter 2 are potentially useful as improved light absorbers and exciton transporters in light-harvesting systems. One specific application for these materials is in organic solar cells. In these cells, conducting polymers, such as P3HT, absorb light, and excitons diffuse through the material until they reach a exciton-splitting interface.[1] However, the efficiency of such cells is generally low because the exciton is not preferentially directed towards the interface. Random diffusion results in a significant fraction of excitons that do not reach the desired interface. The efficiency of organic solar cells could be improved if the exciton preferentially diffused to an exciton-splitting interface, or if the lifetime of the excitons in the material was longer. It would be useful to investigate these triarylamine

systems for applications in organic solar cells, as they potentially have the ability to direct excitons and improve exciton diffusion lengths.

One possible extension of this work could be measuring the efficiency of energy transfer to biphenyl sites incorporated into triarylamine polymers. The triarylamine systems investigated in Chapter 2 demonstrated efficient energy trapping over a distance of about 5 nm. One interesting experiment could be to measure the efficiency over a larger range, possibly microns. This would be accomplished by making triarylamine polymer chains several hundred units long and measuring the fluorescence rise time at the biphenyl site, as exemplified by Figure 1. If the exciton trapping were still efficient, a noticeable rise in fluorescence from the biphenyl site should be observed, even in long chains where the exciton was generated far away. This experiment would determine if these sites could potentially act as antennae, drawing excitons to favorable locations, such as interfaces.

Another experiment would entail measuring the exciton diffusion lengths of the triarylamine dendrimers to see if there is an enhanced hopping rate. It is known that N,N′-diphenyl-N,N′-(3-methylphenyl)-[1,1′-biphenyl]-4,4′-diamine (TPD), which incorporates a biphenyl unit, making a highly conductive amorphous material.[2] The inclusion of the biphenyl unit into the triarylamine system may have improved the exciton diffusion length in these systems as well. To measure this, the photoluminescence of the system can be measured as a function of film thickness on a metal substrate. When excitons diffuse to a metal interface, fluorescence is immediately quenched. Therefore, the exciton diffusion length can be estimated by depositing thin films on a metal substrate and measuring the photoluminescence as a function of film thickness. When the film is thinner than the exciton diffusion length, nearly all the fluorescence will be quenched, while films thicker than the exciton diffusion length will show substantial fluorescence. Film thickness can be approximately controlled by spin coating or drop casting,[3] and the film thickness can be measured with a surface profilometer.

B. Thiophene Macrocycles – The thiophene macrocycles investigated in Chapter 3 show some interesting photonic properties, including a high chromophore coupling constant and two-photon absorption cross section. The ability to enhance the two-photon cross

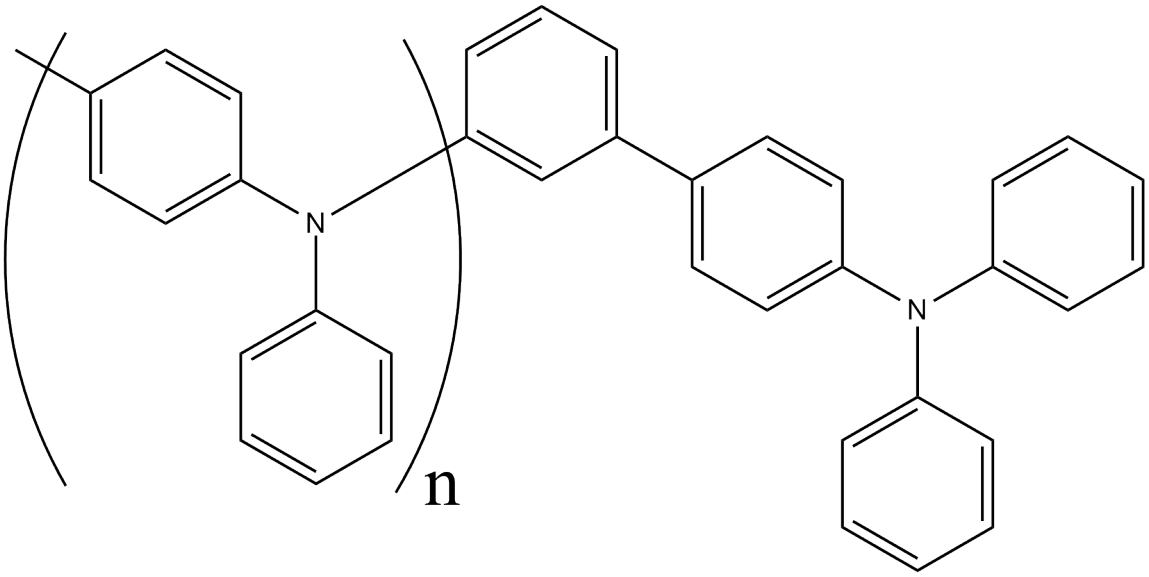

Figure 6.1. A possible Triarylamine polymer. The length of the arylamine chain can be varied to determine the effective range of the biphenyl trapping unit.

section of a material by cyclizing it would be enormously useful to applications in imaging[4-5] and lithography.[6-7] Advances in these techniques require smaller light-absorption cross sections. Light absorption in two-photon material is proportional to the amplitude squared. Therefore, if the amplitude distribution of a light pulse is given by a Gaussian distribution with a value of σ, then the two-photon absorption is given by σ^2.

To verify that this result is due to the cycilization and not to some separate property of thiophene chromophores, the experiments could be repeated using a macrocyclic thiophene with degeneracy broken by deviations from planar. Inclusion of tert-butyl groups on adjacent thiophene molecules should hinder planarization and substantially reduce the chromophore coupling. The two-photon cross section should be similarly reduced if these properties are linked. The coupling constant would again be calculated from fluorescence anisotropy measurements to ensure that the degeneracy is broken, and the two-photon cross section would be measured by two-photon excitation fluorescence.

C. Macroporous p-GaP(100) - The novel macroporous p-GaP(100) system reported in Chapter 4 has applications as a photonic material and as a light harvesting material. As prepared, the system was not optimized for light harvesting. A small enhancement in the energy conversion efficiency at red wavelengths was observed, but the overall energy conversion efficiency was reduced. With better control of the etching process, morphologies that are favorable for solar energy conversion can be utilized.

The processes that lead to the formation of the nanostructured p-GaP need to be explored in greater detail to determine how to best make nanostructures that demonstrate greater energy conversion efficiencies. A number of experimental variables can be tried to this end. Alternative solvents, such as ethanol and alternative electrolytes, could influence the etching rate and the nanostructure width. It was shown that the addition of ethylene glycol had a substantial effect on the size of the macropores. This was attributed to competitive binding of the ethylene glycol over the Br^- anions, which resulted in a higher pore density. Therefore, using a less polar solvent could help concentrate anions on the surface by reducing the solubility of the anions in the solvent, giving smaller pore densities. Since the mechanism of binding of the bromide to the GaP is not known, information could be gained about the binding mechanism by using alternative

electrolytes. An alternative electrolyte could be bromate anions (BrO_3^-), as this anion is more sterically crowded. However, if bromide is required to bind multiple sites on the crystal during the etching process, this anion would not work for making porous materials. On the other hand, if a strong electron donating group is needed, this anion is a stronger Lewis base than bromide, and would therefore be an effective electrolyte for etching. If bromate is an effective ion for etching, then other strong Lewis bases should be investigated.

Another possibility for improved control over the etching process is using an AC etching waveform. Using an AC etching waveform may allow for more precise control of the Br^- concentration at the surface. The material would etch briefly while the potential swings to more positive voltages and recovers lost bromine surface concentration while the potential swings to more negative voltages. This could allow for more precise control of etching. An example waveform is shown in Figure 2.

The etching procedure detailed in Chapter 4 may also have separate applications with other p-type III-V materials. For example, InGaN is a modern blue and green light-emitting diode (LED) material. Making InGaN porous has been shown to substantially improve photoluminescence and is an area of active research.[8-10] However, making p-InGaN porous is done by patterning with a mask and either chemically or physically etching the surface. If this method also works for p-InGaN, it would be a much cheaper method of making the porous material. In addition, the porous p-GaP(100) prepared in this study had a much higher surface area than these other etching procedures, which is predicted to produce a device with higher luminosity.

D. Design Rules for Nanostructured Light Harvesting Devices - In Chapter 5, the effect of dopant density on carrier collection efficiency in nanostructured materials was quantified. This work identifies optimal electronic properties for nanostructured materials. In particular, it defines the necessary dopant density for efficient carrier collection. This is particularly useful for getting enhanced carrier collection efficiency out of materials such as nanostructured GaP. However, more can be done to understand what parameters are most relevant to nanostructured photoelectrode operation.

Our previous study of macroporous p-GaP(100) showed poor energy conversion properties. The size of the wall in the macroporous GaP was on the order of 300 nm, and

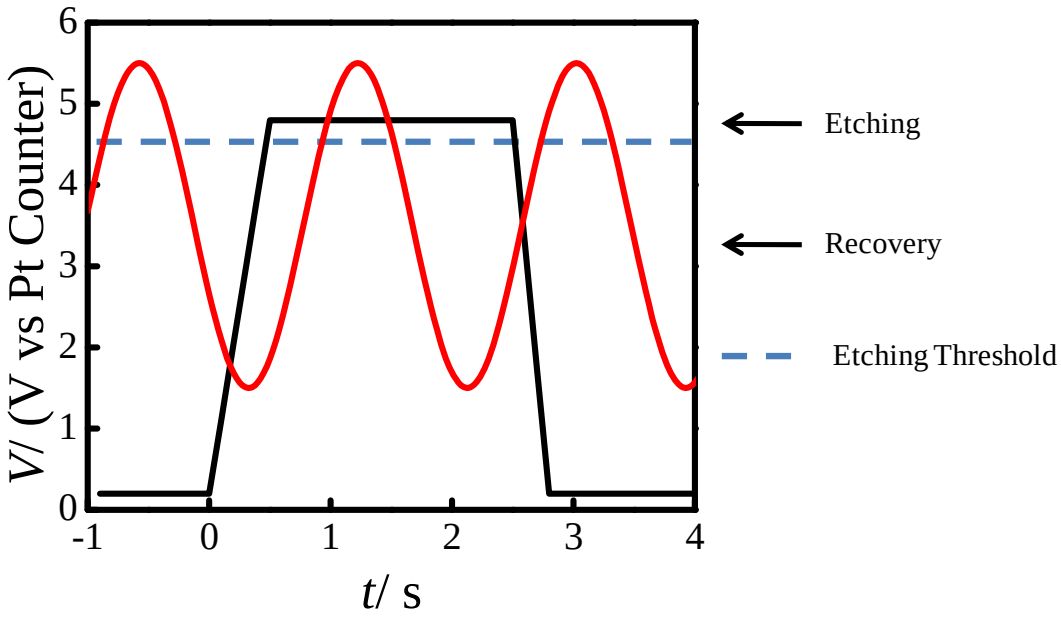

Figure 6.2. (black) Potential waveform used in the etching of p-GaP. (red) A possible AC macroporous etching voltage for p-GaP. This AC voltage waveform maintains the p-GaP electrode at a voltage above the threshold for a fine time duration that should favor macroporous etching.

the size of the depletion region was calculated to be on the order of 500 nm. This suggests that our initial attempts at using macroporous p-GaP failed due to a mismatch in the size of the material and the internal electric field. Using this information, we can attempt to revisit macroporous p-GaP to optimize the size of the macroporous material in order to better match the internal electric field. A more heavily doped material should yield improved results.

Finally, while these studies compared the relative effects of dopant density, minority carrier diffusion length and surface recombination velocity, a number of other properties could be explored, including slower charge transfer rates. Only systems with outer-sphere redox couples were investigated. The effect of a slower rate consistent with hydrogen reduction at a semiconductor interface could be studied to determine the relative effect for fuel forming photoelectrodes. In the case of slow heterogeneous charge transfer, an overpotential needs to develop in order to drive the reaction. This would predict that surface recombination would have a greater effect on the energy conversion efficiency of photoelectrodes if charge transfer is slow.

E. Conclusion - The work on organic chromophores and inorganic semiconductor materials detailed in this thesis was performed separately and without deliberate overlap. However, solar energy conversion systems can be envisioned that utilize both types of materials working in concert.[11-14] Hybrid solar cells, such as bulk heterojunction solar cells and dye-sensitized solar cells, utilize strongly-absorbing organic chromophores with long exciton diffusion lengths. In these systems, light is absorbed by an organic chromophore, generating an exciton that is transferred and separated at an interface with an inorganic semiconductor. The inorganic semiconductors are typically nanostructured, as a large surface area allows for more light absorbing chromophores to be within a diffusion length of the interface. Understanding the optoelectronic properties of nanostructured semiconductors is also of critical importance in hybrid systems. In hybrid systems, the aforementioned parameters for organic and inorganic light harvesting materials outlined in this thesis must be considered. If the pertinent issues relating to their interface are also properly addressed, organic/inorganic hybrid light harvesting systems can be envisioned that augment the best features of each component and enable widespread use of solar energy.

References.

1. Sariciftci, N. S.; Smilowitz, L.; Heeger, A. J.; Wudl, F. *Science* **1992**, *258*.
2. Shimakawa, K.; Murata, K.; Matsumoto, S.; Naito, H. *J. Non-Cryst. Solids* **2006**, *352*, 1671.
3. Schubert, D. W.; Dunkel, T. *Mater. Res. Innov.* **2003**, *7*, 314.
4. Denk, W.; Strickler, J.; Webb, W. W. *Science* **1990**, *248*, 73.
5. Helmchen, F.; Denk, W. *Nat. Methods* **2005**, *2*, 932.
6. Park, S.-H.; Yang, D.-Y.; Lee, K.-S. *Laser Photonics Rev.* **2009**, *3*, 1.
7. Dong, X.-Z.; Zhao, Z.-S.; Duan, X.-M. *Appl. Phys. Lett.* **2007**, *91*, 124103.
8. Kim, K.; Choi, J.; Bae, T. S.; Jung, M.; Woo, D. H. *Jpn. J. Appl. Phys.* **2007**, *46*, 6682.
9. Yang, C. C.; Lin, C. F.; Lin, C. M.; Chang, C. C.; Chen, K. T.; Chien, J. F.; Chang, C. Y. *Appl. Phys. Lett.* **2008**, *93*, 203103.
10. Kim, H.; Cho, J.; Lee, J. W.; Yoon, S.; Kim, H.; Sone, C.; Park, Y.; Seong, T.-Y. *Appl. Phys. Lett.* **2007**, *90*, 161110.
11. Grätzel, M. *Photochem. Photobiol. C* **2003**, *4*, 145.
12. Ginger, D. S.; Greenham, N. C. *Phys. Rev. B* **1999**, *59*, 10622.
13. Scheblykin, I. G.; Yartsev, A.; Pullerits, T.; Gulbinas, V.; Sundström, V. *J. Phys. Chem. B* **2007**, *111*, 6303.
14. Lancelle-Beltran, E.; Prené, P.; Boscher, C.; Belleville, P.; Buvat, P.; Sanchez, C. *Adv. Mater.* **2006**, *18*, 2579.